FACHBEREICH
MATHEMATIK UND
NATURWISSENSCHAFTEN
BERGISCHE UNIVERSITÄT
WUPPERTAL

Study of the Potential of the ATLAS Detector to Observe a Higgs Decay into $t\bar{t}$ in the Fully Hadronic Decay Mode

Dissertation zur Erlangung des Doktorgrades
des Fachbereiches Mathematik und Naturwissenschaften
der
Bergischen Universität Wuppertal
vorgelegt von

Anca-Mirela Siebel

WUB-DIS 2006-07
December 2006

Contents

Chapter 1

Introduction

In 2007 the Large Hadron Collider (LHC) will be inaugurated at the European Nuclear Research Centre CERN. It will be the largest particle accelerator ever built, colliding beams of protons at unprecedented beam energies. The main purpose of the LHC will be to search for new physical phenomena, either to complete the experimental verification of the predictions of the Standard Model of particle physics, as in the case of the Higgs boson, or to discover indications for phenomena beyond the Standard Model.

To this end, two general purpose detectors are being built to be operated at the LHC, the CMS[1] and the ATLAS[2] experiment. The faculty for science of the University of Wuppertal contributes to the ATLAS experiment with the development of central parts of the ATLAS experiment as well as with studies for physics analysis to be carried out on the data recorded by ATLAS. Additionally, a research team of the University is contributing to the development of the GRID, which allows for distributed computing in High Energy Physics data analysis.

Several theoretical concepts of extensions to the Standard Model have already been developed, one of the most promising among them is the theory of Super-Symmetry. This theory does not only predict a multitude of until now undiscovered particles, but it also requires the existence of at least five so-called Higgs bosons. Higgs bosons are a necessary ingredient of any gauge theory for an interaction with massive gauge bosons. In this way a Higgs boson is a necessary part of the Standard Model in order to describe the electro-weak interaction. The additional constraints in a super-symmetric expansion to the Standard Model make the introduction of more Higgs bosons necessary. In the case of the minimal

[1] **C**ompact **M**uon **S**olenoid
[2] **A** **T**oroidal **L**HC **A**paratu**S**

super-symmetric extension, the so called MSSM, five Higgs bosons are predicted. Two of these bosons, the heavy scalar Higgs boson H and the pseudo-scalar Higgs boson A are subject to this study.

At LHC H and A bosons could be produced via the process of gluon-gluon fusion. In a parameter configuration of the MSSM theory which is generally considered likely, the H and the A boson are degenerate in mass and are massive enough to decay into a top quark-anti-quark pair. The top quark-anti-quark pair decays predominantly into six jets of hadrons. This decay mode has not only the largest branching ratio, but is also the kinematically most constraint mode due to the lack of escaping high-energetic neutrinos, which appear in the competing decay modes. However, proton-proton collisions at the LHC lead to an abundance of hard processes of the strong interaction with numerous high-energy jets in the final state, which form a huge background to the full hadronic decay mode to a top quark-anti-quark pair.

The aim of this study is, to investigate the prospects for the reconstruction of $H/A \to t\bar{t}$ decays in the fully hadronic mode with the ATLAS experiment. To this end hadronically decaying $t\bar{t}$-pairs are separated from the background of QCD produced light jet events using a neural network. The mass spectrum of the $t\bar{t}$-pairs is reconstructed using a kinematic fitting procedure. The spectrum is then compared to theoretical predictions. An important part of these predictions is the interference between the production of $t\bar{t}$-pairs via Higgs decays and the production via direct gluon-gluon fusion. The interference alters the shape of the mass spectrum substantially and provides an even stronger signature of the presence of a Higgs production than the Higgs mass peak itself. Special consideration is paid to the optimisation of the ATLAS trigger conditions with respect to the discovery potential of Higgs bosons by introducing a b-tagging procedure into the trigger algorithms.

This thesis is structured as follows: In Chap. 2 the Standard Model of particle physics and some theoretical extensions thereof are presented, before in Chap. 3 the LHC accelerator and the ATLAS experiment are introduced. Chap. 4 gives a short overview of the Monte-Carlo simulations of particle interactions used in this analysis. In Chap. 5 phenomenological aspects of $t\bar{t}$-pair and Higgs production are discussed. In Chap. 6 the selection of simulated data and the analysis of the $t\bar{t}$-mass spectrum are described, before in Chap. 7 the impact of the trigger conditions on this analysis and the optimisation of the trigger conditions are addressed.

Chapter 2

Standard Model and Beyond

Particle physics deals with the basic constituents of matter and the interactions taking place between them. In the current understanding of particle physics, matter is built of fermions, while the interactions are mediated by bosons.

Four types of fundamental forces can be observed in nature: electromagnetic, weak, strong and gravitational force. Modern theory attempts to describe the phenomena related to the electromagnetic, weak and strong interaction by means of relativistic quantum field theories in which invariance under appropriate local gauge transformations is imposed. This gauge symmetry leads to formulations of the theory whose perturbative expansions can by renormalised, leading eventually to finite results. The strong interaction is described by Quantum Chromo-Dynamics (QCD), based on an invariance under SU(3) colour-space transformations. A coherent description of the weak interaction can only be obtained after unifying weak and electromagnetic interactions to the electroweak interaction which is described by the Glashow-Salam-Weinberg model based on a SU(2)⊗U(1) gauge symmetry group. QCD and the Glashow-Salam-Weinberg model together form the Standard Model (SM) of particle physics, a gauge theory based on the mathematical framework of local $SU(3) \otimes SU(2) \otimes U(1)$ gauge invariance.

The gravitational force is described by the general theory of relativity which is based on symmetries of space-time itself. By now it cannot be included in the Standard Model . However, gravitational interaction is several orders of magnitude weaker than the other three interactions and can therefore be neglected within particle physics.

According to the Standard Model all matter is built up of spin-$\frac{1}{2}$ fermions: quarks

		Quarks				**Leptons**	
Helicity	Isospin	Charge				Charge	
left-handed	$+\frac{1}{2}$ $-\frac{1}{2}$	$+\frac{2}{3}$ $-\frac{1}{3}$	$\begin{pmatrix} u \\ d \end{pmatrix}_{\text{red}}$	$\begin{pmatrix} u \\ d \end{pmatrix}_{\text{green}}$	$\begin{pmatrix} u \\ d \end{pmatrix}_{\text{blue}}$	0 -1	$\begin{pmatrix} \nu_e \\ e \end{pmatrix}$
	$+\frac{1}{2}$ $-\frac{1}{2}$	$+\frac{2}{3}$ $-\frac{1}{3}$	$\begin{pmatrix} c \\ s \end{pmatrix}_{\text{red}}$	$\begin{pmatrix} c \\ s \end{pmatrix}_{\text{green}}$	$\begin{pmatrix} c \\ s \end{pmatrix}_{\text{blue}}$	0 -1	$\begin{pmatrix} \nu_\mu \\ \mu \end{pmatrix}$
	$+\frac{1}{2}$ $-\frac{1}{2}$	$+\frac{2}{3}$ $-\frac{1}{3}$	$\begin{pmatrix} t \\ b \end{pmatrix}_{\text{red}}$	$\begin{pmatrix} t \\ b \end{pmatrix}_{\text{green}}$	$\begin{pmatrix} t \\ b \end{pmatrix}_{\text{blue}}$	0 -1	$\begin{pmatrix} \nu_\tau \\ \tau \end{pmatrix}$
right-handed	0	$+\frac{2}{3}$ $-\frac{1}{3}$	$(u)_{\text{red}}$ $(d)_{\text{red}}$	$(u)_{\text{green}}$ $(d)_{\text{green}}$	$(u)_{\text{blue}}$ $(d)_{\text{blue}}$	-1	(e)
	0	$+\frac{2}{3}$ $-\frac{1}{3}$	$(c)_{\text{red}}$ $(s)_{\text{red}}$	$(c)_{\text{green}}$ $(s)_{\text{green}}$	$(c)_{\text{blue}}$ $(s)_{\text{blue}}$	-1	(μ)
	0	$+\frac{2}{3}$ $-\frac{1}{3}$	$(t)_{\text{red}}$ $(b)_{\text{red}}$	$(t)_{\text{green}}$ $(b)_{\text{green}}$	$(t)_{\text{blue}}$ $(b)_{\text{blue}}$	-1	(τ)

Table 2.1: Elementary fermions in the SM. Electric charges are given in units of the elementary charge.

and leptons. An overview over these fermions is given in TAB. 2.1. The fermions taking part in strong interactions are referred to as quarks the others are called leptons. While only electrically charged particles take part in electromagnetic interactions, all left handed fermions, which appear as iso-spin dubletts in TAB. 2.1, take part in weak interactions. Assuming massless neutrinos there are no right handed neutrinos. However, experimental evidence of neutrino mass not equal zero has meanwhile been found [1].

As can be seen in TAB. 2.1, three generations of two quarks and two leptons exist. It has been experimentally shown that the number of light neutrino flavours is three [2] supporting the assumption that only three generations of fermions exist. The Standard Model does not give a reason for the existence of exactly three generations [3].

2.1 The Quantum Chromo-Dynamics

The theory of the strong interaction is based on a symmetry with respect to redefinitions of the strong (colour-) charge.

The observation of the spin-$\frac{3}{2}$ baryons like the Δ^{++}, the Δ^{-} and the Ω^{-} consisting

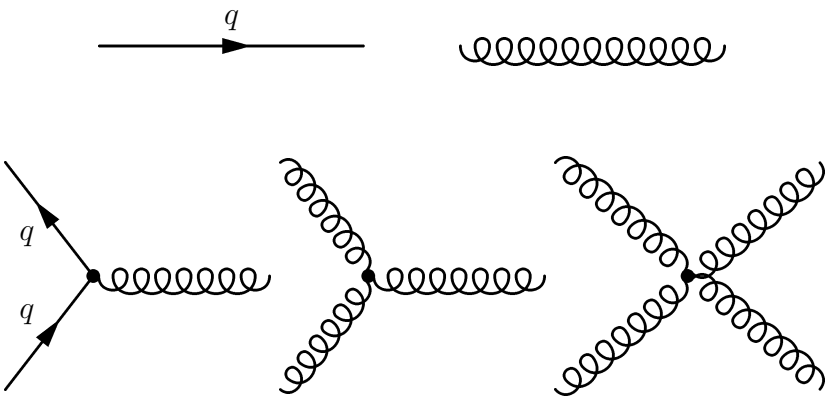

Figure 2.1: The fundamental Feynman graphs of QCD.From left to right they are the propagators for the fermionic quarks and gluons, the gluon radiation or quark-pair production, and the self-coupling of three and four gluons.

of three up- respectively strange-quarks with completely symmetric quark wave functions required the introduction of a new degree of freedom for quarks, the colour, in order to prevent a violation of the Pauli principle. The colour part of the above wave functions has to be completely antisymmetric with respect to quark exchange. The experimental proof of the existence of exactly three quark colours has been found in the decay width of the pion and the ratio of the cross-sections of hadron and lepton production in e^+e^- annihilation:

$$R = \frac{\sigma(e^+e^- \to q\bar{q})}{\sigma(e^+e^- \to \mu^+\mu^-)} \quad . \tag{2.1}$$

The colour degree of freedom is identified with the charge of the strong interaction. The relevant gauge symmetry has been found to be $SU(3)$ transformation within colour space. Local $SU(3)$ symmetry requires the introduction of eight bosonic fields which couple to the quarks. The bosonic fields are identified with the gluons which act as force carrier particles of the strong interaction.

The $SU(3)$ group is an exact gauge symmetry, so that the gluons are massless. Its non-Abelian structure directly leads to self-coupling of the gluons, the gluons therefore carry colour charge themselves. The three fundamental vertices of QCD are shown in Fig. 2.1. Series expansions in terms of the strong coupling α_s lead to predictions of QCD processes. However, loops in the diagrams of these expansions give divergent contributions. The process of cancelling out these divergencies is called renormalisation. The renormalisation introduces an energy

scale dependence of the coupling α_s. The energy dependence of α_s is given by the renormalisation group equation.

$$\mu\frac{\partial\alpha}{\partial\mu} = \beta(\alpha) = -\frac{\beta_0}{2\pi}\alpha^2 - \frac{\beta_1}{4\pi^2}\alpha^3 - \dots \tag{2.2}$$

with the coefficients:

$$\beta_0 = 11 - \frac{2}{3}N_F \tag{2.3}$$

$$\beta_1 = 51 - \frac{19}{3}N_F \quad . \tag{2.4}$$

taking into account the first two terms on the right side of Eq. 2.2, the solution

$$\alpha_s(\mu^2) = \frac{4\pi}{\beta_0 \ln\left(\frac{\mu^2}{\Lambda^2}\right)}\left(1 - \frac{\beta_1 \ln\ln\left(\frac{\mu^2}{\Lambda^2}\right)}{\beta_0^2 \ln\left(\frac{\mu^2}{\Lambda^2}\right)}\right) \tag{2.5}$$

is obtained where the factor in brackets is a correction to the first order solution (only β_0 in Eq. 2.2) due to the β_1-term in Eq. 2.2 . As can be seen in Eq. 2.3 β_0 is positive for $N_F < 33/2$ which leads to a decrease of the coupling α_s with energy. This is in contrast with the behaviour of the electromagnetic interaction where α is increasing with energy. The reason for this different energy dependence is the non-Abelian structure of the $SU(3)$ group in QCD which leads to self-coupling between differently colour-charged gluons, which allow for bosonic loops with a relative sign opposite to fermionic loops in the renormalisation calculations. The running of α_s leads to two consequences:

- α_s formally diverges at $Q = \Lambda$. Therefore, perturbative calculations cannot be applied at energies of the order of Λ or smaller. Moreover, colour charged objects are always bound in colour-neutral states, the hadrons, due to the increasing interaction. This phenomenon is called *confinement* of QCD. There are two types of hadrons: baryons and mesons. Baryons are fermions consisting of three quarks. Most prominent examples of baryons are the proton and the neutron of which atomic nuclei are built. Mesons are bosons that consist of one quark and one anti-quark. Besides these well confirmed states there are also further states possible: the possibly recently discovered penta-quark [4] consists of four quarks and an anti-quark, while the theoretically discussed glue-ball has gluons as valence constituents.

- α_s decreases with energy so that perturbation theories can be applied. Furthermore, high energies correspond to small distances, which means that inside the proton, the quark constituents behave approximately as free particles. This phenomenon is known as *asymptotic freedom*.

Due to the large number of contributing Feynman-graphs and the relatively large coupling constant, the perturbative approach is limited in QCD. Predictions are usually calculated only to order of α_s^2 or expanded in logarithmic approximations. To describe the final hadronic state phenomenological models of hadronisation have to be applied [5, 6].

2.2 Electro-weak interaction

Gauge bosons introduced by imposing a local gauge symmetry on the Lagrangian are required to be massless, because mass terms for the gauge-bosons would violate the gauge symmetry. However, the bosons of the weak interaction, Z and $W^{\pm}$ are massive. Peter Higgs showed that massive bosons can be achieved via spontaneous symmetry breaking. [7] This implies that the Lagrangian of the system retains its invariance under the symmetry group, while the vacuum state no longer satisfies the invariance. A corresponding formulation of the theroy of weak interaction can be achieved by unifying the weak and the electromagnetic interaction into one theory. The required symmetry corresponds to the group $SU(2) \otimes U(1)$. It has been extended to the hadronic sector via a mechanism suggested by Glashow-Iliapoulous-Maiani [8] , which finally led to the concept of Cabbibo-Kobayashi-Maskawa for quark flavour mixing [9]. Imposing these symmetries onto the Lagrangian requires the introduction of three bosonic gauge fields $W_\mu^{(1)}$, $W_\mu^{(2)}$, $W_\mu^{(3)}$ for the $SU(2)$ symmetry and a single gauge field B_μ for the $U(1)$ symmetry [10]. The coupling constants of the W's and B are g_1 and g_2 respectively. The W-bosons only couple to the left-handed particles and right-handed anti-particles, where left-handed and right-handed fields are defined as:

$$\psi_L = \frac{1}{2}(1 - \gamma_5)\psi \qquad \text{and} \qquad \psi_R = \frac{1}{2}(1 + \gamma_5)\psi \tag{2.6}$$

The introduction of $U(1)$ symmetry is essential in order to incorporate the electric charge Q and unify the weak and electromagnetic interactions in a common gauge structure. Right-handed fermions are assigned to transform under $U(1)$ only, no right-handed neutrino is introduced. Further, a weakly interacting scalar field is required: The Higgs field, which is a complex doublet written as

$$\phi = \frac{1}{\sqrt{2}} \begin{pmatrix} \phi_1 + i\phi_2 \\ \phi_3 + i\phi_4 \end{pmatrix} \tag{2.7}$$

For the scalar field the potential

$$V = \mu^2 \phi\phi^* + \lambda(\phi\phi^*)^2 \tag{2.8}$$

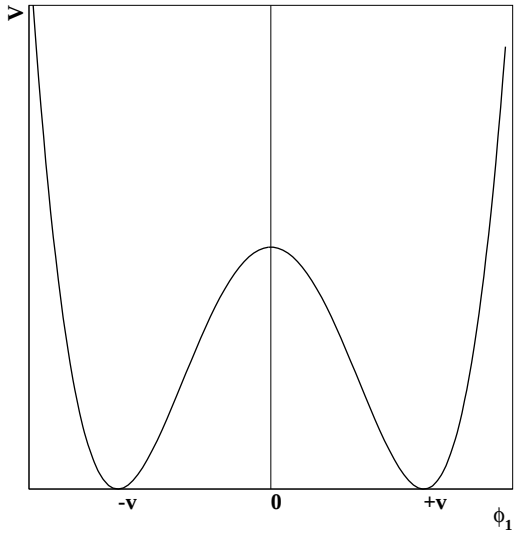

Figure 2.2: The potential of the scalar doublet ϕ

with $\mu^2 < 0$ is assumed. Therefore the potential function resembles a "Mexican-hat" shape as shown in FIG. 2.2. The minima of the potential are located on a hyper-sphere with a radius $v^2 = -\frac{1}{2}\frac{\mu^2}{\lambda} > 0$. This leads to a non-vanishing value of $|\phi|^2$ in the physical ground state. The ground state can be chosen arbitrarily. A usual choice for the ground state is

$$\phi_0 = \frac{1}{\sqrt{2}} \begin{pmatrix} 0 \\ v \end{pmatrix} \quad . \tag{2.9}$$

The choice of a designated ground state breaks the $SU(2) \otimes U(1)$ symmetry spontaneously. Due to the coupling to the non-vanishing ground state of the Higgs boson, the gauge bosons acquire masses where W^1 and W^2 mix to the mass eigen-states W^+ and W^- while W^3 and B mix to Z and A. The masses of the new gauge bosons are given by:

$$m_A = 0 \tag{2.10}$$

$$m_W = \frac{g_2 v}{2} \tag{2.11}$$

$$m_Z = \frac{m_w}{\cos\theta_W} \tag{2.12}$$

where the mixing angle θ_W is given by:

$$\cos\theta_W = \frac{g_1}{\sqrt{g_1^2 + g_2^2}} \tag{2.13}$$

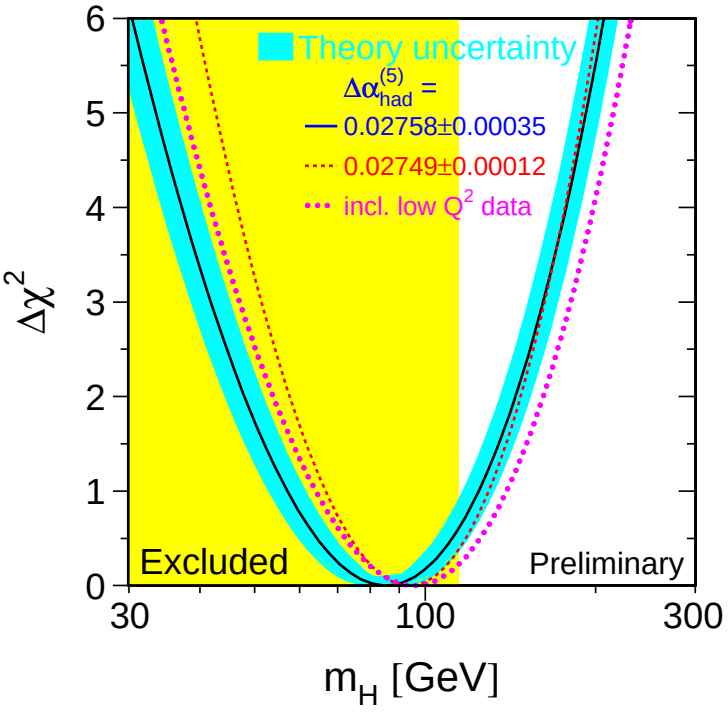

Figure 2.3: The exclusion region for the higgs mass in comparison with the result of indirect fits

From the measurements of the vector-boson masses and the mixing angle the vacuum expectation value of the Higgs field has been determined to be $v = (\sqrt{2}G_F)^{-\frac{1}{2}} \simeq 246\text{GeV}$. The mass of the Higgs boson in the Standard Model is given by

$$m_H = (2\lambda)^{\frac{1}{2}} v \tag{2.14}$$

where λ is a dimensionless coupling constant of the scalar potential. However, as λ is not yet determined, the Standard Model does not give a prediction for the Higgs mass. Direct searches by the LEP experiments lead to a lower limit in the mass of the Higgs boson of 114.4GeV [11] while high precision measurements of the Standard Model parameters by the LEP experiments result in an upper limit on the Standard Model Higgs mass of 199 GeV at the 99% confidence level [11]. The LEP data are also used to set an upper bound on the HZZ coupling for various assumptions concerning the decay of the Higgs boson [11]. Considering

these results, any assertion that LEP has excluded the majority of the range allowed by the precision electroweak fit is premature. On the other hand, any resemblance between the most likely mass value $m_H \sim 115$ GeV hinted at by direct searches during the last months of LEP is surely coincidental. Reprocessings of the analysed data reduced the significance of the observed signal further.

2.3 Free parameters of the Standard Model

The Standard Model of electroweak and strong interaction has 19 parameters (or more, considering massive neutrinos) which are not predicted by theory but have to be determined by experiments and used as an input to the model. They are:

- The coupling constant α_s at a given energy or alternatively the integration constant Λ
- A parity-violating phase is allowed for in QCD. As no CP-violation has been observed in strong interactions, this phase is zero.
- The four parameters of the Cabbibo-Kobayashi-Maskawa matrix, which relate the eigenstates of the interaction with the propagation eigenstates. More parameters are required, if a corresponding matrix for massive neutrinos has to be taken into account. The exact number of parameters depends on the type of neutrinos (Majorana/Dirac).
- The nine fermionic masses (twelve, considering massive neutrinos)
- The couplings g_1 and g_2
- The parameters λ and μ

The parameters in the last two points are usually expressed by experimentally more accessible parameters:

- The Sommerfeld fine structure constant α_{QED}
- The Fermi constant G_F obtained from the muon lifetime
- The Z-boson mass m_Z
- The Higgs boson mass m_H

Despite of the enormous success of the Standard Model in predicting new particles (c, b, t, $W^{\pm}$ and Z) and the ability to describe the bulk of present data, there are still open questions as the existence of the Higgs boson and the parameters in the neutrino sector which have to be answered. However, even with all parameters determined, several problems, a few of them only aesthetic in nature, remain. Among them are the following:

- The large number of 19 parameters described above which are not predicted by theory is aesthetically unsatisfying. Furthermore, there is no explanation for the existence of three fermion generations.
- Gravitation cannot be implemented in the Standard Model. The complete lack of a quantum theory of gravity imposes large problems when dealing with strong gravitational fields at small distances.
- The Standard Model is not able to describe the surplus of baryonic matter over anti-matter in the universe. The CP-violation allows in principle for such a mechanism, so that the failure of the Standard Model in this aspect maybe related to our insufficient knowledge of the exact processes in the early universe.
- A very fine tuning of parameters is needed to cancel out quadratic divergencies in the loop corrections of the Higgs propagator. A miraculous cancellation of terms of the order of the Planck scale of 10^{19}GeV is required for the Higgs to have a mass of the order of $100GeV$. This so-called *Hierarchy problem* is one of the main points in searching for extensions to the Standard Model.

2.4 Supersymmetry

It is convenient to organise the questions raised by the Standard Model into three categories:

- **Problem of Mass**: Do particle masses really originate from a Higgs boson and if so, why are these masses not closer to the Planck mass $m_P \simeq 10^{19}$ GeV?
- **Problem of Unification**: Is there a simple gauge group framework for unifying all the particle interactions, a so-called Grand Unified Theory (GUT) and if it exists, does it predict observable new phenomena such as baryon

decay and/or neutrino masses, and does it predict relations between parameters of the Standard Model such as gauge couplings or fermion masses?

- **Problem of Flavour**: Why are there so many different types of quarks and leptons and what explains their weak charged-current mixing and CP violation?

The main theoretical reason to expect super-symmetry at an accessible energy scale is provided by the already mentioned hierarchy problem: Why is $m_W \ll m_P$ or, equivalent, why is $G_F \sim 1/m_W^2 \gg G_N = 1/m_P^2$? Another question is why the Coulomb potential in an atom is so much greater than the Newton potential: $e^2 \gg G_N m^2 = m^2/m_P^2$, where m is a typical particle mass?

A simple solution would be to set $m_P \gg m_W$ by hand and consider the problem solved. But as the quantum corrections to m_H and hence m_W are quadratically divergent in the Standard Model :

$$\delta m_{H,W} \simeq \mathcal{O}(\frac{\alpha}{\pi})\Lambda^2 \tag{2.15}$$

which is $\gg m_W^2$ if the cutoff Λ, which represents the scale where new physics beyond the Standard Model appears, is comparable to the scale of Grand Unified Theories (GUT scale) or the Planck scale. If for example, the Standard Model were to hold unscathed all the way up to Planck mass $m_P \sim 10^{19}$ GeV, the radiative correction Eq. 2.15 would be 36 orders of magnitude greater than the physical values of $m_{H,W}^2$. This is not a problem from the mathematical point of view of renormalisation theory, a tree-level value of m_H^2 that is equal and opposite to the correction Eq. 2.15 should be postulated in order to obtain the correct physical value. As the correction Eq. 2.15 should be kept comparable to most of the physical values the idea described above is rather unnatural [12].

The natural cancellation of these divergencies is possible in a super-symmetric theory, in which the number of fermions and bosons is equal and they have identical couplings. As bosonic and fermionic loops have opposite signs, the residual one-loop correction is of the form

$$\delta m_{H,W} \simeq \mathcal{O}(\frac{\alpha}{\pi})(m_B^2 - m_F^2) \tag{2.16}$$

which is $\lesssim m_{H,W}^2$ and hence naturally small if the super-symmetric partner bosons B and fermions F have similar masses:

$$|m_B^2 - m_F^2| \lesssim 1 \text{ TeV}^2 \tag{2.17}$$

The naturalness of the mass hierarchy is the best motivation for finding super-symmetry at relatively low energies [13]. In addition to the super-symmetric idea of removing the quadratic divergencies shown in Eq. 2.15 by introducing cancellation terms like Eq. 2.16, there are many logarithmic divergences absent in a super-symmetric theory which is the underlying reason why super-symmetry solves the fine tuning problem of the effective Higgs potential when m_H is in the proximity of 115 GeV.

The basic idea of super-symmetry is the existence of fermionic charges Q_α that relate bosons to fermions. All previous symmetries, such as flavour $SU(3)$ or electromagnetic $U(1)$ have involved scalar charges Q that link particles with the same spin into multiplets. In the relativistic limit super-multiplets consist of massless particles with spins differing by half a unit. In the case of simple $N = 1$ super-symmetry, the basic building blocks are *chiral super-multiplets*:

$$\begin{pmatrix} \frac{1}{2} \\ 0 \end{pmatrix} \quad \text{e.g.} \begin{pmatrix} l(\text{lepton}) \\ \tilde{l}(\text{slepton}) \end{pmatrix} \quad \text{or} \begin{pmatrix} q(\text{quarks}) \\ \tilde{q}(\text{squark}) \end{pmatrix} \tag{2.18}$$

gauge super-multiplets:

$$\begin{pmatrix} 1 \\ \frac{1}{2} \end{pmatrix} \quad \text{e.g.} \begin{pmatrix} \gamma(\text{photon}) \\ \tilde{\gamma}(\text{photino}) \end{pmatrix} \quad \text{or} \begin{pmatrix} g(\text{gluon}) \\ \tilde{g}(\text{gluino}) \end{pmatrix} \tag{2.19}$$

and the *graviton super-multiplet* consisting of the spin-2 graviton and the spin$-3/2$ gravitino.

In the Standard Model none of the known fermions q, l can be paired with any of the known bosons $\gamma, W^\pm, Z^0, g, H$, due to the fact that their internal quantum number do not match:

- Quarks q sit in triplet representations of colour, whereas the known bosons are either singlets or octets of colour.
- Leptons l have non-zero lepton number $L = 1$, whereas the bosons have $L = 0$

The only possibility is to introduce new super-symmetric partners, so called *spartners*, for all known particles: quark $\rightarrow$ squark, lepton $\rightarrow$ slepton, photon $\rightarrow$ photino, Z $\rightarrow$ Zino, W $\rightarrow$ Wino, gluon $\rightarrow$ gluino, Higgs $\rightarrow$ Higgsino as suggested in Eq. 2.18 and Eq. 2.19.

2.4.1 The Minimal Super-symmetric Standard Model

Any super-symmetric model is based on a Lagrangian which contains a super-symmetric part and a super-symmetry-breaking part. The Minimal Super-symmetric extension of the Standard Model (MSSM) has the same gauge interactions as the Standard Model, and Yukawa interactions that are closely related. They are based on a super-potential W that is a cubic function of complex super-fields corresponding to left-handed fermion fields. Conventional left-handed quark and lepton doublets are denoted L, Q, and right-handed fermions are introduced via their conjugate fields, which themselves are left-handed, $e_R \to E^c$, $u_R \to U^c$, $d_R \to D^c$.

$$W = \sum_{L,E^c} \lambda_L L E^c H_1 + \sum_{Q,U^c} \lambda_U Q U^c H_2 + \sum_{Q,D^c} \lambda_D Q D^c H_1 + \mu H_1 H_2 \qquad (2.20)$$

The first three terms in Eq. 2.20 yield masses for the charged leptons, charge-$(+2/3)$ quarks and charge-$(-1/3)$ quarks respectively. All the Yukawa couplings $\lambda_{L,U,D}$ are 3×3 matrices in flavour space, whose diagonalisation yield the mass eigenstates and Cabbibo-Kobayashi-Maskawa mixing angles. Two distinct Higgs doublets $H_{1,2}$ are introduced for two important reasons. One reason is that the super-potential must be an analytic polynomial: As seen in Eq. 2.20 it cannot contain both H and H^*, whereas the Standard Model uses both of these to give masses to all the quarks and leptons with just a single Higgs doublet. The other reason is to cancel the so-called triangle anomalies that destroy the renormalisation of a gauge theory. Ordinary Higgs boson doublets do not contribute to these anomalies, but the fermions in Higgs super-multiplets do, and two doublets are required to cancel each others' contributions. Once two Higgs super-multiplets are introduced there is the necessity of a bilinear term $\mu H_1 H_2$ coupling them together.

There are important possible variations on the MSSM super-potential Eq. 2.20, which are impossible in the Standard Model, but are allowed by the gauge symmetries of the MSSM super-multiplets. These are additional super-potential terms that violate the quantity known as R parity:

$$R \equiv (-1)^{3B+L+2S}, \qquad (2.21)$$

where B is the baryon number, L is lepton number and S is spin. For all the particles in the Standard Model $R = +1$ while all their spartners have $R = -1$, identical values of B and L, but differ in spin by half a unit. If both B and L would be conserved, R would be conserved.

There are three important consequences of R conservation:

- sparticles are always produced in pairs, e.g. $p\bar{p} \to \tilde{q}\tilde{g}X$, $e^+e^- \to \tilde{\mu}^+\tilde{\mu}^-$
- heavier particles decay to lighter ones, e.g. $\tilde{q} \to q\tilde{g}$, $\tilde{\mu} \to \mu\tilde{\gamma}$
- the lightest particles is stable, because has no legal decay mode.

This feature constrains strongly the possible nature of the lightest super-symmetric light sparticles.

2.4.2 Super-symmetric Higgs Bosons

As discussed above, two complex Higgs doublets are expected in MSSM $H_2 \equiv (H_2^+, H_2^0)$, $H_1 \equiv (H_1^+, H_1^0)$ with a total of eight real degrees of freedom and opposite hyper-charges in order to give masses to all the matter fermions. Of these, three are forced via the Higgs mechanism to become the longitudinal polarisation states of $W^\pm$ and Z^0, leaving five physical Higgs bosons to be discovered by experiment. Three of these are neutral: the lighter CP-even neutral h, the heavier CP-even neutral H, the CP-odd neutral A, and charged bosons $H^\pm$. All Higgs masses and couplings in the MSSM at the tree level are characterised by the Higgs vacuum expectation $v = \sqrt{v_1^2 + v_2^2} = 246\ GeV$ and by the plane $(m_A, \tan\beta)$ where $\tan\beta = \frac{v_1}{v_2}$ is the ratio of vacuum expectation values. $\tan\beta$ is an undetermined parameter and should be treated as free. The production and decays of the MSSM Higgs bosons will be discussed in detail in Sect. 5.2.

Chapter 3

The Experiment

3.1 The Large Hadron Collider LHC

The Large Hadron Collider (LHC) is a particle accelerator which is being built at CERN, the European Organisation for Nuclear Research, the world's largest particle physics laboratory. When it will be switched on in 2007, it will be the most powerful instrument ever built to investigate the properties of particles.

The LHC will replace CERN's Large Electron Positron (LEP) collider and is built in LEP's 27 km long tunnel, about 100 m underground. It will provide proton-proton collisions at $\sqrt{s} = 14$ TeV with a design luminosity of $L = 10^{34} cm^{-2} s^{-1}$. With a bunch crossing taking place every 25ns and with approximately 22 proton-proton collisions per bunch crossings at full luminosity, LHC is opening a new frontier in particle physics. LHC will not be limited to only the study of proton-proton collisions but also be able to provide heavy-ion collisions with a collision energy of 1148 TeV.

Before being injected into the LHC, the proton beams will be prepared by CERN's existing "accelerator complex", a succession of machines with increasingly higher energies, one injecting the beam into the next one, which takes over to bring the beam to an even higher energy.

In order to bend the 7 TeV proton beams around the ring, the LHC dipole magnets must be able to produce a magnetic field of 8.36 Tesla, a value which is made possible using superconductive coils. The LHC operates at ~ 4 Kelvin and uses the most advanced superconductive magnet and accelerator technologies. 1,296 superconductive dipoles and more than 2,500 other magnets will guide and collide the LHC beams.

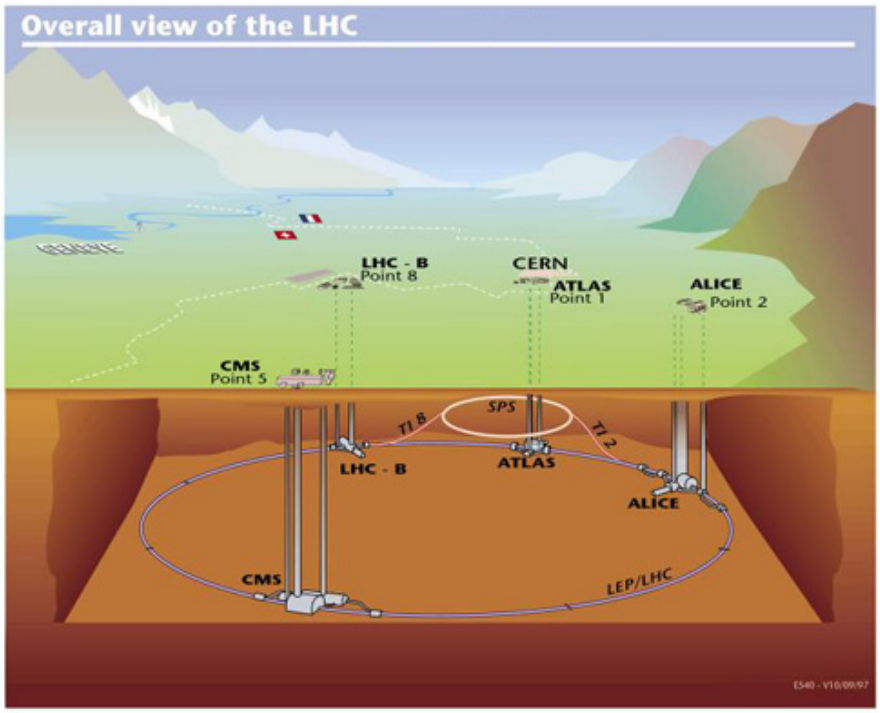

Figure 3.1: Schematic view of the LHC accelerator

Five experiments will study what will happen when LHC beams collide:

- ALICE- **A** large **I**on **C**ollider **E**xperiment. The ALICE detector is built as a heavy-ion detector, to exploit the unique physics potential of nucleus-nucleus interactions at LHC energies. The ALICE collaboration's aim is to study the physics of strongly interacting matter at extreme energy densities, where the formation of a new state of matter, the quark-gluon plasma is expected.

- ATLAS - **A** **T**oroidal **L**HC **A**paratu**s**. The ATLAS detector is one of the two general-purpose detectors which will search for new phenomena, explore the fundamental nature of matter and the basic forces that govern our universe. ATLAS is the largest collaborative effort (above 1800 physicist) ever attempted in physics.

- CMS - The **C**ompact **M**uon **S**olenoid detector is the second general-purpose detector which will detect and record the results of interesting collisions. Its central feature is a huge, high field (4 Tesla) solenoid, 13 m in length and 6

m in diameter. Its compact design will be big enough to contain the electromagnetic and hadron calorimetry and also make possible a performant muon detection system.

- LHCb - The LHCb apparatus will be the most sensitive instrument ever created to detect tiny differences between matter and antimatter. Being designed for a specific purpose, the structure of the detector is less complex than the big general purpose detectors ATLAS and CMS, and allows the collaboration to concentrate on one of the best possible detectors for B-meson physics.

- TOTEM - **Tot**al Cross-Section, **E**lastic Scattering and Diffraction Dissociation at the LHC (**m**). TOTEM is an experiment dedicated to the measurement of the total cross-section, elastic scattering and diffractive processes at LHC. The total cross-section will be measured using a luminosity independent method which is based on the simultaneous detection of inelastic interactions and of elastic scattering at low momentum transfer.

3.2 The ATLAS Detector

ATLAS is one of the two General Purpose Detectors being designed to operate at LHC. The ATLAS detector is situated at Access Point 1, directly opposite to the CERN main entrance. The basic design criteria for building the ATLAS detector are [15, 16]:

- Very good electromagnetic calorimetry for electron and photon identification and measurements, complemented by the full-coverage hadronic calorimetry for accurate jet and missing transverse energy (E_T^{miss}) measurements

- High-precision muon momentum measurements, with the capability to guarantee accurate measurements at the highest luminosity using the external muon spectrometer alone

- Efficient tracking at high luminosity for high p_T-lepton momentum measurement, electron and photon identification, τ-lepton and heavy-flavour identification, and full event reconstruction capability at lower luminosity

- Large acceptance in pseudo-rapidity (η) with almost full azimuthal angle (ϕ) coverage everywhere.

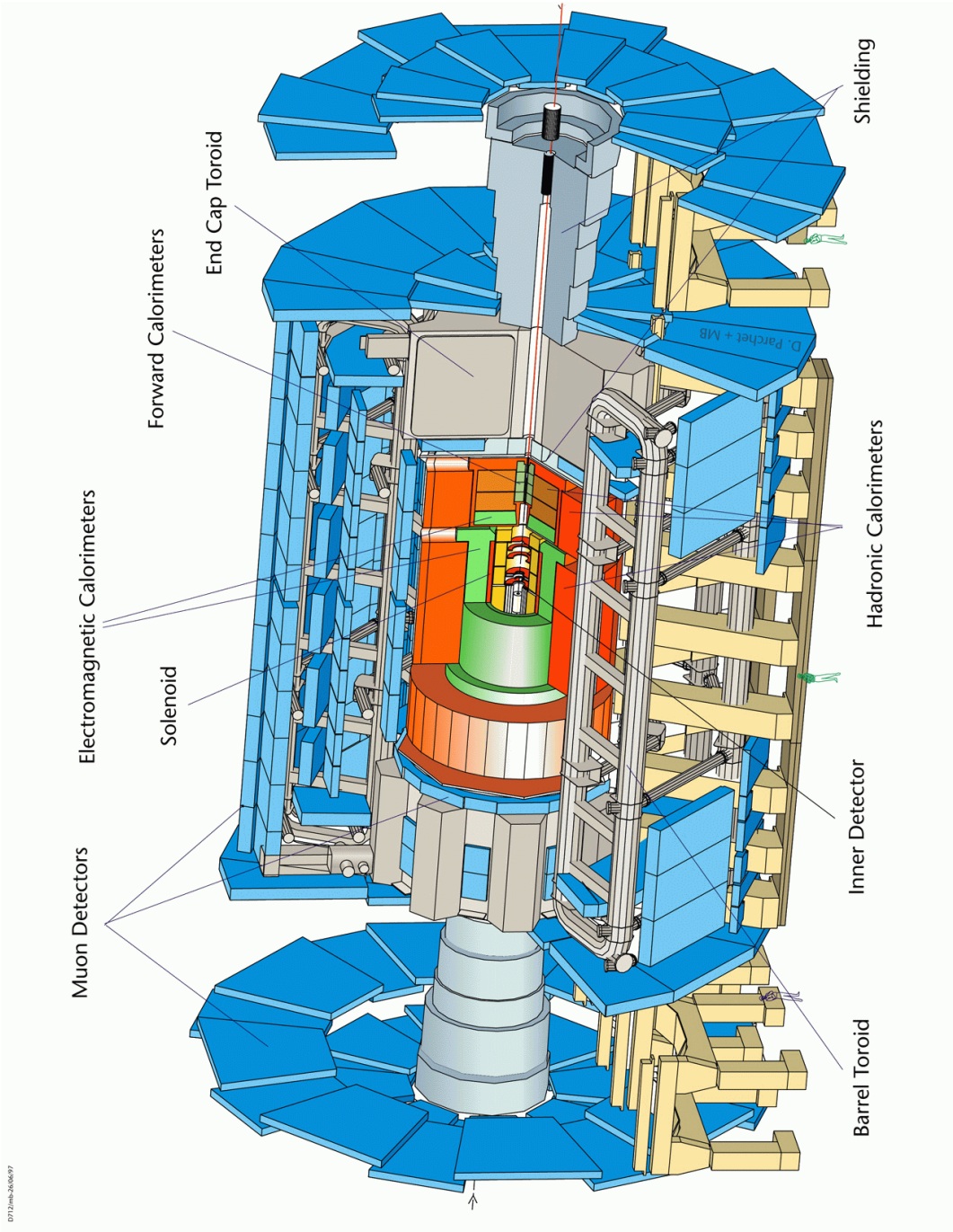

Figure 3.2: Schematic view of the ATLAS experiment

- Triggering and measurements of particles at low-p_T thresholds, providing high efficiencies for most physics processes of interest at LHC

To fulfill these requirements, the detector was built with four major components:

- The Magnet System that bends charged particles for momentum measurements;
- The Inner Tracker which measures the momentum of each charged particle;
- The Calorimeter which measures the energy carried by photons, leptons or jets of particles;
- The Muon Spectrometer which identifies and measures muons.

The size and weight of the detector is unprecedented: total length of 42 m and a radius of 11 m with a weight of approximately 7000 tons.

3.2.1 The Inner Detector

The layout of the Inner Detector combines high-resolution detectors at the inner radii with continuous tracking elements at the outer radii, all contained in the Central Solenoid (CS) which provides a nominal magnetic field of 2 Tesla. The momentum and vertex resolution required by the physics processes demand high-precision measurements to be made with high-granularity detectors, given the very large track density expected at LHC. Semiconductor tracking detectors, using silicon micro-strip (SCT) and pixel technologies fulfill these features. The highest granularity is achieved around the vertex region using semiconductor pixel detectors. The total number of precision layers is limited due to the large amount of material they introduce and by the high-cost. The Inner Detector (ID) consists of three parts:

- The Pixel Detector
- The Semiconductor Tracker (SCT)
- The Transition Radiation Tracker (TRT)

The Pixel Detector

The Pixel Detector is designed to provide a very high granularity, high precision set of measurements as close as possible to the interaction point. A Pixel sensor is a 16.4×60.8 mm^2 wafer of silicon with 46,080 pixels, 50×400 square-microns each. The Pixel Detector determines the impact parameter resolution which allows b-tagging performance at the level of 50-60% efficiency (depending of the luminosity) and short living particles such as B-hadrons and τ-lepton identification. To achieve this goal, three cylindrical layers in the barrel region and three forward disks of pixel detectors for the end-caps are forseen. The cylindrical layers have a radial position of 50.5 mm, 88.5 mm and 122.5 mm respectively and are made of identical staves inclined with azimuthal angle of 20° and in each layer are 22, 38 and 52 staves. Each stave is composed of 13 pixel modules. The innermost pixel layer is called B-layer. It is very important for the secondary vertex measurement performance and has been designed to be removable, as its lifetime is limited due to the radiation damage. Intense development has been performed in ATLAS to improve radiation tolerance of the devices, since the level of radiation in ATLAS is expected to be very high. The exact lifetime depends on the luminosity profile. One disk is made of 8 sectors with 6 modules in each sector. Disk modules are identical to the barrel modules, except the connecting cables.

The Silicon Semiconductor Tracker (SCT)

The Silicon Semiconductor Tracker is based upon silicon micro-strip detector technology. The SCT system is designed to provide eight precision measurements per track in the intermediate radial range, contributing to the measurement of momentum, impact parameter and vertex position. In the barrel SCT eight layers of silicon micro-strip detectors are used to provide precision points in the $R\phi$ and z coordinates, using small stereo angles to obtain the z measurement. Each silicon detector is 6.35×6.40cm^2 and 780 readout strips of 80 μm pitch. The barrel modules are mounted on carbon-fibre cylinders which carry the cooling system, at radii of 30.0, 37.3, 44.7 and 52.0 cm. The end-cap modules are mounted in up to three rings onto nine wheels, which are interconnected by a space-frame. The radial range of each disk is adapted to limit the coverage to a pseudo-rapidity range of $|\eta| \simeq 2.5$.

Transition Radiation Tracker (TRT)

The TRT is based on straw tubes (cylindrical proportional counters), which can operate at the very high rates expected at LHC, due to their small diameter and the isolation of the sense wires within individual gas volumes. The TRT detector occupies the space between last silicon layer and the cryostat wall. The detector construction is modularised in order to simplify assembly procedures and minimise at every stage the number of straw tubes affected by any failure. The barrel part contains 52544 axial straw tubes of about 150 cm length at radii between 56 cm and 107 cm. The end-caps contain a total of 319,488 radial straws at radii between 64 cm and 103 cm (inner end-caps), respectively 48 cm and 103 cm (outer end-caps). The TRT provides on average 36 two-dimensional measurement points with 170 μm resolution for charged particle tracks with $|\eta| < 2.5$ and $p_T > 0.5$ GeV.

3.2.2 The Calorimetry

The calorimetry consists of an electromagnetic (EM) calorimeter covering the pseudo-rapidity region $|\eta| < 3.2$, a hadronic barrel calorimeter covering $|\eta| < 1.7$, hadronic end-cap calorimeters covering $1.5 < |\eta| < 3.2$ and forward calorimeters covering $3.1 < |\eta| < 4.9$.

The Electromagnetic Calorimeter

The EM calorimeter is a lead/liquid argon (LAr) detector with accordion geometry which provides complete ϕ symmetry without azimuthal cracks. Over the pseudo-rapidity range $|\eta| < 1.8$, it is preceded by a pre-sampler detector, installed immediately behind the cryostat cold wall, which is used to correct for the energy lost in the material upstream of the calorimeter. The basic requirements fulfilled by the EM calorimeter are:

- the largest possible rapidity coverage to observe rare physics processes ($H \to \gamma\gamma$)
- electron reconstruction capability from 1-2 GeV up to 5 TeV
- excellent energy resolution in range 10-300 GeV; the constant term of the resolution formula should be at the level of 1%

- dynamic range from 50 MeV to 5 TeV
- energy scale precision 0.1%
- linearity of response better than 0.5% in the energy range up to 300 GeV
- coherent noise below 3 MeV per channel
- bunch-crossing identification

The Hadronic Barrel Calorimeter

The Tile Calorimeter is a large hadronic sampling calorimeter which makes use of steel as the absorber material and scintillating plates read out by wavelength shifting (WLS) fibres as the active medium. It covers the central range $|\eta| < 1.7$. The new feature of its design is the orientation of the scintillating tiles which are placed in planes perpendicular to the colliding beams and are staggered in depth. A good sampling homogeneity is obtained when the calorimeter is placed behind an electromagnetic compartment and a coil equivalent to a total of about two interaction lengths of material. The Tile Calorimeter consists of a cylindrical structure with an inner radius of 2280 mm and an outer radius of 4230 mm. It is subdivided into a 5640 mm long central barrel and two 2910 mm extended barrels as shown in FIG. 3.2. The thickness of the calorimeter in the gap is improved, which has the same segmentation as the rest of the calorimeter. The total number of channels is about 10000.

Hadronic End-Cap Calorimeter (HEC)

The HEC uses liquid argon technique and copper plates as the absorber spaced by 8.5 mm gaps equipped with three parallel electrodes. Only the middle one is a readout electrode, the other two are placed to form an electrostatic capacitor.

Forward calorimeter (FCAL)

The FCAL is integrated in the end-cap cryostat with a front face at about 4.7m from the interaction point. The FCAL uses liquid argon as the sensitive medium. It is a particularly challenging detector due to the very high level of radiation present in the forward area. To face the radiation, a structure based on metal matrix with regularly spaced longitudinal channels filled with concentric roads

and tubes is used. The basic performance characteristics for hadronic and forward calorimetry are the following:

- reconstruct jets up to $|\eta| = 5.0$
- reconstruct p_T^{miss}

The following requirements arise from the first two:

- granularity of $\Delta\eta \times \Delta\phi = 0.1 \times 0.1$ for $|\eta| < 3.0$ and $\Delta\eta \times \Delta\phi = 0.2 \times 0.2$ in forward region
- energy resolution of $\Delta E/E = 50\%/\sqrt{(E)} + 3\%$ for $|\eta| < 3.0$ and $\Delta E/E = 100\%/\sqrt{(E)} + 10\%$ in $3.0 < |\eta| < 5.0$
- energy linearity within 2% up to the $E_T = 4$ TeV
- total thickness of about 10λ (interaction length)

3.2.3 The Muon Spectrometer

The muon spectrometer is based on the magnetic deflection of muon tracks in the large superconducting air-core toroid magnets, instrumented with separate trigger and high precision tracking chambers. The precision measurement of the muon tracks is made in the $R-z$ projection, in a direction parallel to the bending direction of the magnetic field; the axial coordinate z is measured in the barrel and the radial coordinate R is measured in the transition and end-cap regions. The trigger system covers the pseudo-rapidity range $|\eta| < 2.4$. In the barrel region ($\eta < 1.0$), which is covered by the large barrel toroid system, muons are measured in three layers of chambers around the beam axis using precision Monitored Drift Tubes (MDTs) and fast Resistive Plate Chambers (RPCs). In regions of larger pseudo-rapidity, also three layers of chambers are installed, but vertically. Here Thin Gap Chambers (TGCs) are used for triggering. The precision measurement of muons is again done with MDTs, except for the innermost ring of the inner station of the end caps and for $\eta > 2$. In the barrel of the ATLAS muon system, the muon chambers are installed in three cylinders concentric with the beam axis at radii of about 5, 7.5 and 10 m. They are arranged to form projective towers pointing to the nominal interaction vertex. In the end caps, the distance in z from the vertex is about 7, 10 and 14m for the three layers.

3.2.4 The Magnet System

The Magnet System is an arrangement of a Central Solenoid (CS) providing the Inner Detector with a magnetic field, surrounded by a system of three large air-core toroids generating the magnetic field for the muon spectrometer. The overall dimensions of the magnet system are 26 m in length and 20 m in diameter.

The Central Solenoid

The central ATLAS solenoid has a length of 5.3 m with a bore of 2.4 m. The conductor is a composite that consists of a flat superconducting cable located in the centre of an aluminium stabiliser with rectangular cross-section. It is designed to provide a field of 2 Tesla in the central tracking volume with a peak magnetic field of 2.6 Tesla. To reduce the material build-up, the solenoid shares the cryostat with the liquid argon calorimeter.

The Toroid Magnet

The ATLAS Toroid Magnet system consists of eight Barrel coils housed in separate cryostats and two end-cap cryostats housing eight coils each. The end-cap coils systems are rotated by 22.5° with respect to the Barrel Toroids in order to provide radial overlap and to optimise the bending power in the interface regions of both coil systems.

3.3 The ATLAS Trigger System

The frequency of bunch-crossings at LHC is 40 MHz, leading to an interaction rate $\sim 10^9 s^{-1}$ at a luminosity of 10^{34} $cm^{-2}s^{-1}$. The readout system of the ATLAS experiment is not fast enough to cope with this data rate. However, the vast majority of these events are so called minimum bias events, which are of little interest for physics analyses. The task of the ATLAS trigger system is to reduce the rate of recorded events enough to enable the readout system to persistify the collected data by suppressing the readout of minimum bias events and osimilar event types in favour of event types which are more interesting to physics analyses. The rate of selected events must be reduced to ∼100 Hz for permanent storage. As an rejection factor of 10^7 against "minimum-bias" processes is required, an

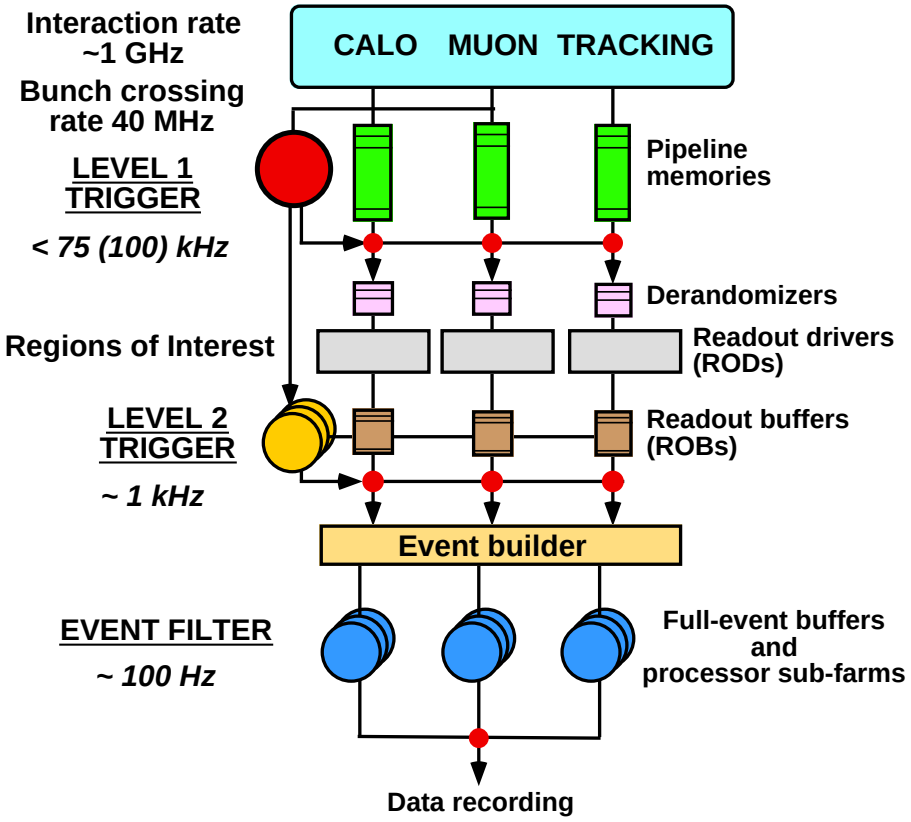

Figure 3.3: The Atlas trigger system

efficient and selective trigger system is needed in order to reduce the amount of data but to select the relevant physics events as Higgs boson decays [15–17].

The Atlas trigger is designed as a multilevel system where at each level the decision made by a previous level is refined and additionally selection criteria are applied. Fig. 3.3 gives a simplified view of the trigger system which is divided in three levels:

- The Level-1 (LVL1) trigger is a hardware-based system. It receives signals from the calorimeter and muon detectors of Atlas and its task is to reduce the event rate from 1 GHz to 75 kHz with a latency of 2.5 μs. In this time the data from all detectors are stored in the pipeline memories. The events accepted at LVL1 are transferred to the Read-Out Buffers (ROBs).
- The Level-2 (LVL2) trigger is based on software selection algorithms running in the processor farms. LVL2 can access data from all sub-detectors

of ATLAS in so called "Regions-of-Interest" (ROI) which were identified by the LVL1 system. The average time to decide if an event passes this level is about 10 ms, hence a fast rejection strategy is needed using specialised trigger algorithms.

- The Event Filter (EF) is also based on software selection algorithms. In comparison with LVL2 it runs after the event building, such as the complete event information is available to the EF algorithms. The EF performs in few seconds a thorough event selection and classification process. The EF algorithms are foreseen to be based on offline reconstruction code using the full calibration and alignment information. The events accepted by EF are written to the mass storage.

The last two steps form together the High Level Trigger (HLT).

3.4 Trigger Menu

In order to get an optimal acceptance, an approach based on the use of inclusive criteria for the online event selection has been taken. The signatures are mostly based on single- and di-object high-p_T triggers, where high-p_T refers to objects as charged leptons or jets with $p_T > 10$ GeV [18]. A collection of signatures the trigger is supposed to select an event on is called a trigger menu. A physics signature, or so called "trigger item", is a combination of requirements formulated as trigger conditions. The trigger menu is selected for running at an initial peak luminosity of $2 \cdot 10^{33}\text{cm}^{-2}\text{s}^{-1}$. The trigger menu is divided into four parts:

- Inclusive physics trigger – important to guarantee the coverage of a very large fraction of the ATLAS physics program.

- Pre-scaled physics triggers – used for the extension of the physics coverage, by having inclusive selections with lower thresholds in order to enlarge the kinematic reach and provide samples for understanding background processes and detector performance.

- Exclusive physics triggers – also used for extended physics coverage.

- Dedicated monitoring and calibration triggers – used for understanding of the detector performance.

Furthermore, specific selections might be used to monitor the machine luminosity. The trigger menu and the threshold values are derived from the physics-analysis requirements but take into account the estimates of the total HLT output bandwidth. The trigger menu will evolve continuously, benefitting from a better understanding of the detector and the experience gained when commissioning the experiment. Also a better understanding of the Standard Model gained before the start of LHC might influence the trigger menu.

TAB. 3.1 gives an overview of the major selection signatures needed to guarantee the physics coverage [19]. The trigger items are labelled as "$NoXXi$". Here

- "N" is the minimum number of objects required,
- "o" indicates the type of object which is triggered upon, for example
  - "e" for electron, "γ" for photon, "μ" for muon, "τ" for a τ-hadron, "J" for a jet, "b' for a b-tagged jet,
  - in "xE" the missing transverse energy required is given by x,
  - "E" for the total transverse energy
  - "jE" for total transverse energy obtained using only jets
- "XX" gives the threshold in transverse energy (in GeV)
- "i" indicates an isolation requirement

The threshold indicates the transverse energy value above which the selection has good efficiency for a true object of the specified type. The trigger menu contains only unprescaled (inclusive) triggers to be used for physics purposes. The trigger menu shown above aims for a total rate of 25 kHz at LVL1 and 200 Hz at HLT. Assuming a design capability of 75 kHz at LVL1, there will be room left for additional triggers, especially towards the end of LHC. The rate estimates are based on Monte Carlo predictions which might be a factor of two or more off which requires some safety margin to be planned.

The main contribution to the menu are single- and di-lepton triggers. These signatures are most sensitive to Standard Model and new physics processes involving known or new W and Z bosons. For QCD studies within the Standard Model and for hadronic final states of new physics processes, a number of jet signatures with multiplicities between one and four required jets is presented. Precise determination of the trigger thresholds is the aim of trigger studies in progress.

LVL1 signature	LVL1 rate (kHz)	HLT signature	HLT rate (Hz)	example of physics coverage
MU20	0.8	μ20i	40	$t\bar{t}H$, $H \to W^+W^-$, ZZ, $q\bar{q}\tau^+\tau^-$, W', Z', top, $Z \to l\bar{l}$
2MU"5"	0.2	2μ10	10	$H \to W^+W^-$, ZZ, $Z \to l\bar{l}$
		2μ"5"+mass etc.	10	B physics
EM25i	12	e25i	40	$t\bar{t}H$, $H \to W^+W^-$, W', Z', top,$W \to l\nu$,$Z \to l\bar{l}$,
		γ60i	25	$H \to \gamma\gamma$
2EM15i	4	2e15i	< 1	$H \to WW$, ZZ $Z \to ll$,
		γ20i	2	$H \to \gamma\gamma$
τ60	?	τ60	?	$H^{\pm} \to \tau\nu_{\tau}$
J200	0.2	j400	10	QCD, new physics
2J170	?	2j350	?	QCD, new physics
3J90	0.2	3J165	10	QCD, new physics
4J65	0.2	4J110	10	QCD, new physics
FWDJ	?	FWDJ	?	?
xE150	?	xE200	?	?
E1000	?	E1000	?	?
JE1000	?	JE1000	?	?
Mu10+EM15i	0.1	Mu10+EM15i	1	$H \to WW$, ZZ, $t\bar{t}$ fully leptonic
EM??+NJ	?	EM??+NJ	?	low rate; threshold + jet multiplicity
EM20i+xE20-30	?	EM20i+xE20-30	9	$W \to e\nu$
TAU25+xE30	2	TAU35+xE45	5	$W \to \tau\nu$, $Z \to \tau\tau$ new physics
J50+xE60	0.4	J70+xE70	20	SUSY
Pre-scaled, Technical, Monitoring	5		20	
Total	25		200	

Table 3.1: General Physics Trigger Menu for $2 \cdot 10^{33}\text{cm}^{-2}\text{s}^{-1}$. The "?" in some of the trigger thresholds indicates that the precise value is not yet defined

Chapter 4

Event Simulation

4.1 Pythia

Due to the confinement in strong interactions and the rapidly with higher orders increasing complexity of contributing Feynman-diagrams of QCD, the properties of high energy particle collisions involving strong interactions cannot be calculated exactly. Instead, Monte-Carlo simulation programs are used, which combine an approximate calculation of the hard interaction, mostly involving leading logarithmic approximations, with phenomenological models of the soft processes involved. The output of these simulation programs does not only give theoretical predictions for expected event properties, but it can also be used as input to a simulation of the event evolving in a detector in order to study the response capabilities of the measurement process.

One of these Monte-Carlo simulations is the Pythia program [20], developed by the Lund HEP theory working group. The emphasis in Pythia is put on multi-particle production in collisions between elementary particles. This in particular means hard interaction in e^+e^-, pp and ep colliders. The objective is to provide as accurate as possible a representation of event properties in a wide range of reactions, within and beyond the Standard Model, with emphasis on those where strong interactions play a role, directly or indirectly, and therefore multi-hadronic final states are produced.

For the description of a typical high-energy event, an event generator should contain a simulation of several physics aspects [20]:

1. Initially, two beam particles are coming in towards each other. In case of

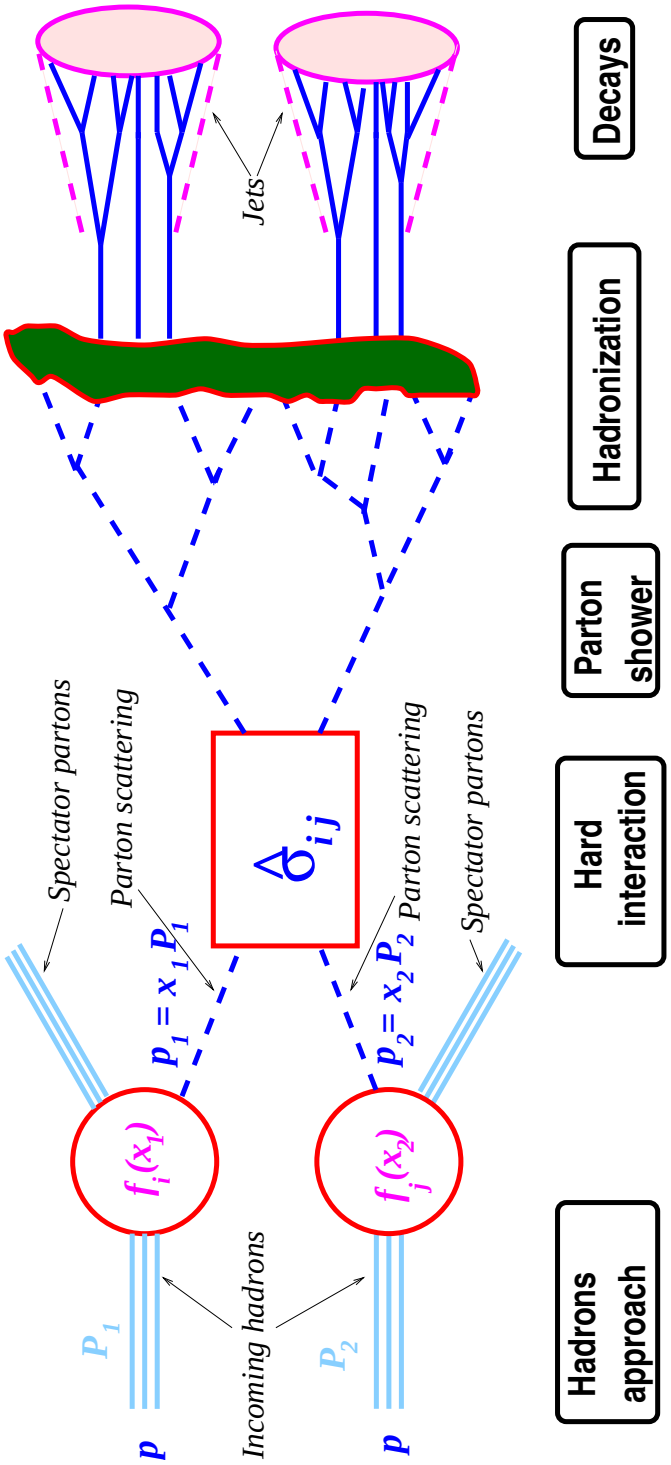

Figure 4.1: The evolution of a collision event drawn schematically [21]

composite incoming particles like protons, each particle is characterised by a set of parton distributions, which defines the partonic structure in terms of flavour composition and energy sharing.

2. One shower initiator parton from each beam starts off a sequence of branchings, such as $q \to qg$ which builds up an initial state shower.

3. One incoming parton from each of the two showers enters the hard process, where then a number of outgoing partons are produced, usually two. It is the nature of this process that determines the main characteristics of the event.

4. The hard process may produce a set of short-lived resonances, like the $Z^0/W^\pm$ gauge bosons, whose decay to partons or leptons has to be considered in close association with the hard process itself.

5. The outgoing partons may branch, just like the incoming did, to build up final state showers.

6. In addition to the hard process considered above, further semi-hard interactions may occur between the remaining partons of the two incoming hadrons.

7. When a shower initiator is taken out of a beam particle, a beam remnant is left behind. This remnant may have an internal structure, and a net colour charge that relates it to the rest of the final state.

8. The QCD confinement mechanism ensures that the outgoing quarks an gluons are not observable directly, but instead fragment to colour neutral hadrons.

9. Normally, the fragmentation mechanism can be seen as occurring in a set of separate colour singlet subsystems, but interconnection effects such as colour rearrangement or Bose-Einstein correlations may complicate the picture.

10. Many of the produced hadrons are unstable and decay further.

A schematic depiction of the phases of a proton-proton collision can be seen in FIG. 4.1. Here, two partons of the protons, carrying a momentum fraction x_1 and x_2 of the protons collide. In the final state jets produced by the hard interactions as well as remnants of the incoming protons can be observed.

4.2 Detector modelling: ATLFAST

For the simulation of the ATLAS detector environment a package called ATLFAST is used. As the name suggest, ATLFAST can be used for a fast-event simulation including the crucial detector aspects: jet reconstruction in the calorimeters, momentum/energy smearing for leptons and photons, magnetic field and missing transverse energy [22].

The package is not meant to replace the full simulation of the detector response. The particle-level simulation is only an intermediate step between the simple analysis of Monte-Carlo events without detector simulation ("Monte-Carlo truth") and the very complicated and time consuming full detector simulation. This simulation is needed for quick and approximate estimations of the signal and background rates and also for the high-statistics studies of the complex background processes at LHC as the use of "Monte-Carlo truth" only often gives too optimistic and therefore misleading results. Considering the large number of events needed to make this study, the full detector simulation cannot be used due to the huge amount of required computing time. Therefore ATLFAST is used here to simulate the influence of the ATLAS detector on the analysis.

The package attempts to reproduce the expected ATLAS detector mass resolution. However, for any specific channel, the ATLAS predictions in terms of resolution and reconstruction efficiency should always be confirmed with full-simulation results. Not all detector aspects can be parametrised in fast simulation and only the basic information on the detector geometry is given: the η-coverage, the size of the barrel/end-cap transition region for the electromagnetic calorimeter and the granularity of the calorimeters. No effects on the detailed shape of particle showers in the calorimeters, charged track multiplicity in jets are considered.

The main goal of the ATLFAST package is to simulate and analyse fully generated events and to select the isolated leptons and photons, to reconstruct jets, label the b-jets, c-jets and τ-jets and to estimate the missing transverse energy. Another part of the package is ATLFAST-B which simulates randomly b-, c- and τ-tagging and provides jet-energy re-calibration. For the following analysis, ATLFAST-B is not used as the calibration of jets and b-tagging simulation do not represent the the expected b-tagging properties to the required degree. [23]

The ATLFAST package can analyse fully or partially generated events: events generated with or without QCD/QED initial and final state radiation, fragmentation, hadronisation and decays of unstable particles. Information about hadronic jets, reconstructed isolated leptons and photons and reconstructed tracks are stored.

4.2.1 Calorimetric Clusters

The transverse energies of the particles not yet decayed are summed up in calorimeter cells of a certain granularity in $\eta \times \phi$ space coordinates over the full calorimeter coverage $|\eta| < 5$. All calorimeter cells with transverse energy larger than 1.5 GeV are considered possible initiators for the clusters. The cells are scanned in decreasing order in E_T in order to verify that the total E_T summed over all cells in a cone $\Delta_R = \sqrt{(}\Delta\eta^2 + \Delta\phi^2)$ exceeds the minimum required threshold for a reconstructed cluster $E_T > 10$ GeV. For this reconstruction a cone radius $\Delta R = 0.4$ is used.

4.2.2 Jet Reconstruction

Clustered calorimeter cells are used for the jet reconstruction. The energies of the clusters which were not selected as associated to the isolated electrons or photons, are smeared according to a Gaussian energy resolution. The jets are reconstructed using a cone algorithm with a radius of 0.4 which is considered the standard value for ATLAS. Jet reconstruction can be done at low and high luminosity. For high luminosity the effect of pile-up is included in the resolution parametrisation. Jets which have E_T >10 GeV are labelled as reconstructed jets.

A special attention is paid to the jets coming from the b-quarks which can be identified using b-tagging techniques as described in Sect. 4.3. In ATLFAST, a jet is labelled as a b-jet if a b-quark with $p_T > 5$ GeV is found in a cone of ΔR =0.2 around the axis of a reconstructed jet for jets with $|\eta| < 2.5$. The same criteria as for b-jets are applied in identification of the c-jets. ATLFAST does not take into account limited efficiencies for b-jets tagging, nor the mis-tagging efficiency for c-jets or light jets.

4.3 b-tagging Procedure

A signature of events in which t-quarks are produced are jets initiated by b-quarks which come from the decay of the t-quark. Unlike t-quarks, b-quarks have a lifetime which is long enough for the b-quark containing hadrons, usually B-mesons, to traverse measurably large distances before they decay. The masses of these hadrons are large enough to give to the decay products a substantial transverse momentum with respect to the direction of the B's momentum. If the trajectories of the decay particles are measured with a high enough precision, the

	u-jet rejection		c-jet rejection	
$\lvert\eta\rvert$	$\epsilon_b = 50\%$	$\epsilon_b = 60\%$	$\epsilon_b = 50\%$	$\epsilon_b = 60\%$
$0 < \lvert\eta\rvert < 0.5$	2.23	2.29	1.11	1.10
$0.5 < \lvert\eta\rvert < 1.0$	1.59	1.76	1.12	1.11
$1.0 < \lvert\eta\rvert < 1.5$	1.22	1.27	1.07	1.06
$1.5 < \lvert\eta\rvert < 2.0$	0.52	0.51	0.86	0.87
$2.0 < \lvert\eta\rvert < 2.5$	0.30	0.38	0.73	0.76

Table 4.1: The parametrisation of $F_1(|\eta|)$ taken from [23]

secondary vertex at which the B-meson decayed can be distinguished from the primary vertex of the event. A jet containing such a secondary vertex is then found to originate from a b-quark.

There are several approaches to b-tagging at collider experiments:

- The secondary vertex is explicitely reconstructed. Studies with this approach have been done by ATLAS e.g. in [24].
- The probability that all particles of a jet originate from the primary vertex is calculated by analysing the particles' impact parameters. Jets in which a probability lower than a cut-value is found, are tagged as b-jets. [25]
- A third method is not relying on the decay length of the B-mesons, but on the possibility that a lepton can be produced in the decay of these Mesons. The so called soft-lepton-tag identifies a jet in which a low energy lepton from a semi-leptonic decay of a b is found as a b-jet, where the branching ratio for b decaying into an electron or muon is around 20%.

As these experimental ways of identifying b-jets are not yet completely implemented in the ATLFAST simulation, an stochastic simulation of the b-tagging procedure is used here. A study of the b-tagging properties [23] using the impact parameter technique determined the efficiency to tag a b-jet correctly to be 50% (60% alternatively). The rejection of c-jets is assumed to be 10.8 (6.2) and the rejection for light jet is assumed to be 150 (54). Here, the rejection is the inverse of the efficiency to mis-tag a c- or light-jet as a b-jet. The rejections depend on the transverse momentum and the pseudo-rapidity of the jet. This dependence is parametrised by

$$R(\eta, p_T) = R_0 \cdot F_1(|\eta|) \cdot F_2(p_T) \tag{4.1}$$

	u-jet rejection		c-jet rejection	
$p_T(GeV)$	$\epsilon_b = 50\%$	$\epsilon_b = 60\%$	$\epsilon_b = 50\%$	$\epsilon_b = 60\%$
$15 < p_T < 30$	0.36	0.42	0.60	0.71
$30 < p_T < 50$	1.01	0.92	0.84	0.87
$50 < p_T < 70$	1.81	1.81	1.11	1.20
$70 < p_T < 100$	2.59	2.47	1.24	1.28
$100 < p_T < 150$	1.76	1.68	1.31	1.25
$150 < p_T < 200$	1.61	1.52	1.39	1.33
$200 < p_T < 250$	0.96	0.88	1.03	1.05
$250 < p_T < 300$	0.46	0.55	0.87	0.90
$300 < p_T < 400$	0.21	0.28	0.66	0.66

Table 4.2: The parametrisation of $F_2(p_T)$ taken from [23]

where R_0 denoted the rejections quoted above and the functions F_1 and F_2 are given in TAB. 4.1 and TAB. 4.2.

A jet is tagged as a b- or light-jet randomly according to the probabilities obtained from the parametrisations of the rejections given above using an b-tagging efficiency of 60%. In order to cover the whole range of p_T, the rejection is assumed to be constant for all $p_T > 300$ GeV. The b-tagging efficiency of 50% is assumed to be too pessimistic as a parametrisation of the achievable off-line b-tagging and therefore not used in this analysis.

4.4 Neural Networks

In order to make a precise measurement of a known quantity or to search for hypothetical new particles, from the sample of events recorded those events are selected which show characteristics resembling the characteristics of the desired signal, while as many background events as possible are rejected. Neural Network methods have become one of the favoured techniques for separating signal from background samples.

An Artificial Neural Network (ANN) or commonly just neural network (NN) is an information processing paradigm that is inspired by the way biological nervous systems, such as the brain, process information. The key element of this paradigm is the novel structure of the information processing system. It is composed of a large number of highly interconnected processing elements (neurons) working in unison to solve specific problems. ANNs, like people, learn by example. An

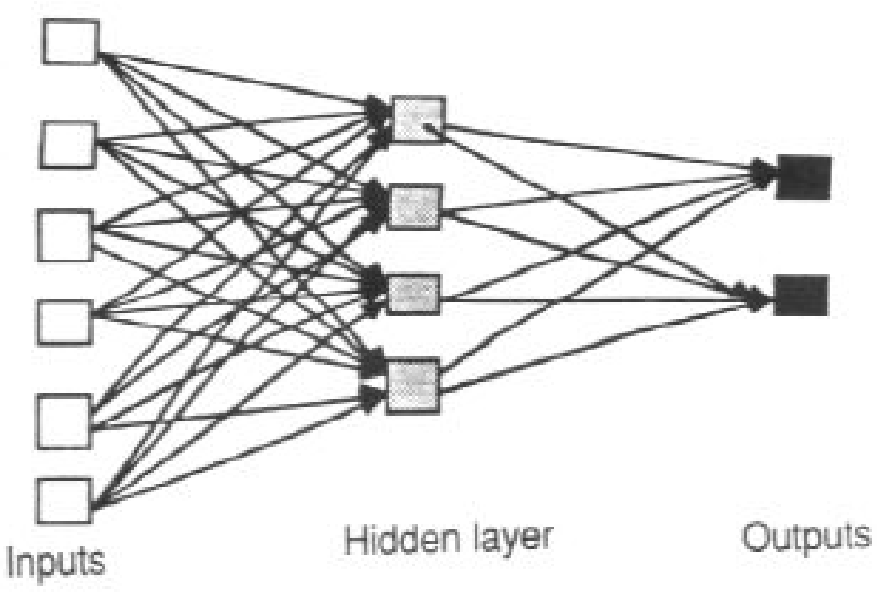

Figure 4.2: Schematic depiction of a neural network

ANN is configured for a specific application, such as pattern recognition or data classification, through a learning process. Learning in biological systems involves adjustments to the synaptic connections that exist between the neurons. This is true of ANNs as well.

Neural networks, with their remarkable ability to derive meaning from complicated or imprecise data, can be used to extract patterns and detect trends that are too complex to be noticed by either humans or other computer techniques. A trained neural network can be thought of as an "expert" in the category of information it has been given to analyse. This expert can then be used to provide projections given new situations of interest and answer "what if" questions. Other advantages include:

1. Adaptive learning: An ability to learn how to do tasks based on the data given for training or initial experience.

2. Self-Organisation: An ANN can create its own organisation or representation of the information it receives during learning time.

3. Real Time Operation: ANN computations may be carried out in parallel, and special hardware devices are being designed and manufactured which take advantage of this capability.

4. Fault Tolerance via Redundant Information Coding: Partial destruction of a network leads to the corresponding degradation of performance. However, some network capabilities may be retained even with major network damage.

The commonest type of artificial neural network consists of three groups, or layers, of units: a layer of "input" units is connected to a layer of "hidden" units, which is connected to a layer of "output" units as can be seen in FIG. 4.2. For a multilayer network with a single output, there is usually no advantage to using more than one hidden layer, except for very complicated separation surfaces.

In the computer science literature many variations of the neural network approach exist, but in high energy physics the main type used is called a "feed-forward multilayer perceptron", which is "trained" using a "back-propagation" algorithm. Despite the intimidating (or skepticism-arousing) names and jargon, a feed-forward network can be thought of as a single-valued function of an array (or vector) of input values. The function (the net) has many parameters, called weights and thresholds, the values of which determine the output for a given input vector (event quantities). Usually the output ranges from 0 to 1 continuously, e.g. the case in which we have two classes - signal and background, we have:

$$\text{output} = \begin{cases} 1 & \text{for signal,} \\ 0 & \text{for background.} \end{cases} \tag{4.2}$$

The mathematical expression for a general FFNN (Feed-Forward Neural Networks) with one hidden layer and one output node is

$$y = g\left(\frac{1}{T}\Sigma_j^{N_h}\omega_j g\left(\frac{1}{T}\Sigma_i^{N_j}\omega_{ji}x_i + \theta_j\right) + \theta\right) \tag{4.3}$$

where N_j is the number of input nodes, N_h is the number of hidden nodes, ω_{ji} are the weights connecting the input nodes x_i to hidden nodes j and the ω_j connects the hidden nodes to the output value y. θ_j and θ are the thresholds of the hidden and output nodes respectively. Therefore, the FFNN can be considered as a non-linear function of $\vec{x}$ with several parameters ω,

$$y = F(\vec{x}, \omega) \tag{4.4}$$

where $F(\vec{x}, \omega)$ is a probability density function which is to be modelled to arbitrarily high accuracy. [26, 27]

"Training the network" is in fact a function minimisation procedure; back-propagation is in essence a gradient descent, starting with random weights and thresholds.

The aim is to reduce the "error function" which is essentially a chi-square-like quantity, the sum of the squared deviations of the neural network output from the desired output for signal (usually 1) and background (usually 0). Then the trained network with its optimised weights and thresholds is used with real events, and the net output for each event is the single criterion on which a decision about signal selection is made.

It is in fact rather simple to write one's own neural net software, but many such packages exist. Perhaps the best known and most widely used is JETNET. In CDF, the OSU group has written a handy ROOT interface to this package. The JETNET web-site also has many references to neural network papers, which are an excellent introduction to the subject.

There are many common questions which arise in conjunction with using neural network techniques. "What is the network actually doing?" "Can I tell what the individual network nodes are selecting?" "Does the network approach give me some new, hidden source of systematic error?" "Do I actually benefit from using a neural net rather than cuts?" A few answers follow [28]:

- Given signal and background samples in the n-dimensional space of the input vectors (set of quantities), a well-trained neural network uses a combination of (n-1)-dimensional hyperplanes to separate the samples. (Each hidden node corresponds to another hyperplane available to help discriminate.)
- Neural networks thus take advantage of all correlations existing among the input variables, some of which may be difficult or impossible to see with a two-dimensional scatter plot!
- A neural network adds no more (or less) systematic uncertainty than cut (or other) methods do - the real limiting factor is how well-modelled the signal and background samples are.
- Typically, neural network approaches work very well even when the space of input (or cut) variables is large, say 15 or more.

Chapter 5

Physics at the LHC

5.1 Top Quark Production at the LHC

5.1.1 Introduction

The top quark, discovered at Fermilab in 1995 [29–32] completed the three-generation structure of the Standard Model (SM) and opened the new field of top quark physics. The top-quark has a mass 35 times larger than the mass of

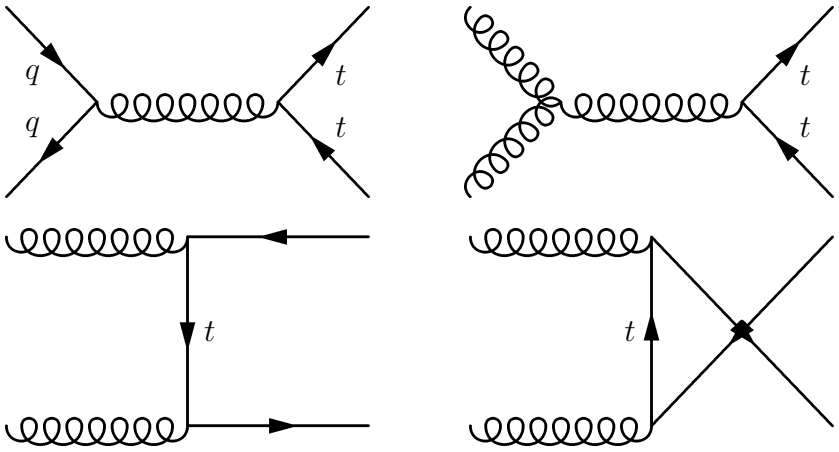

Figure 5.1: The LO Feynman-graphs for $t\bar{t}$ production in proton-proton collisions

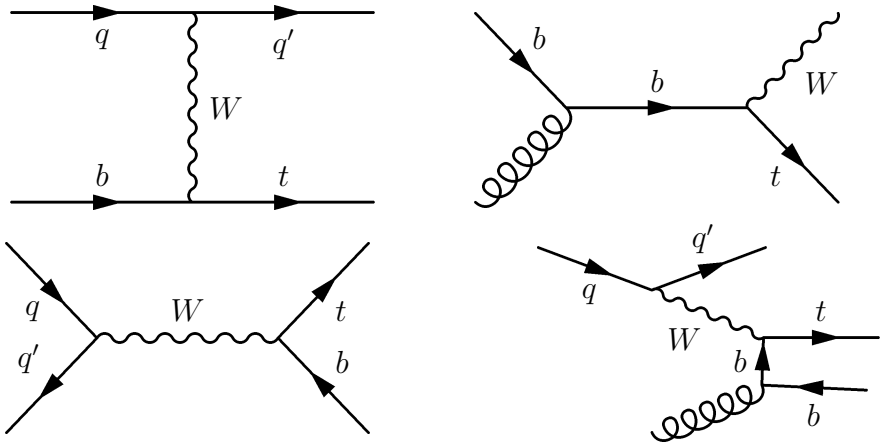

Figure 5.2: The dominant Fenyman-graphs for single-top production in proton-proton collisions

the next heavy quark, a mass close to the scale of electroweak (EW) symmetry breaking.

Even if the top-quark is nothing else than the sixth SM quark, discrepancies between the observations and SM predictions for the top-quark properties may be the sign of new particles and couplings unreachable at lower scales. Moreover, top processes may be important backgrounds for many analysis, such as some Higgs searches. Understanding the top quark properties and probing SM predictions is the natural path towards new physics [33].

With more than 8 millions of top pairs and more than 2 millions of single top events produced every year at low luminosity, the LHC era will open a new opportunity for top quark physics. One of the first goals is the determination of the top quark mass at the 1% level, an important test for the electro-weak sector. This determination will also put stringent constraints onto its symmetry breaking mechanism, either in the Standard Model (SM) or in a super-symmetric framework (e. g. MSSM). The top quark spin properties, through W polarisation and top spin correlation measurements at a precision better than 5% level, will also lead to a deep insight into the nature of the top quark couplings to fermions and to the mechanisms responsible for its production. Also, the precise determination of the (electro-weak) single-top production cross-sections at few percent precision level also constitutes a stringent test of SM [34].

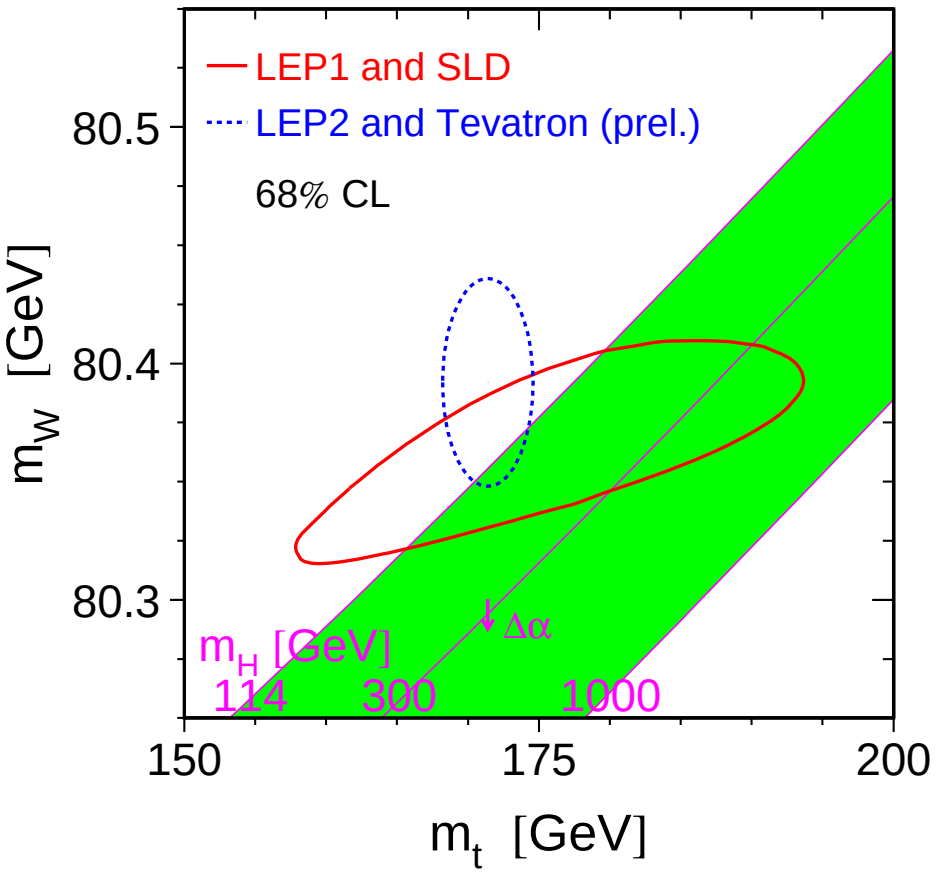

Figure 5.3: The LEP measurements for m_t and m_W together with the predicted correlation between the two quantities.

5.1.2 Production Processes at LHC

In hadron colliders, $t\bar{t}$ pairs are predominantly produced through strong interactions. The relevant Feynman-diagrams in leading order (LO) are shown in FIG. 5.1.

At the Tevatron, where protons and anti-protons are collided, anti-quarks with a momentum fraction x sufficiently high to produce a $t\bar{t}$ pair in a collision, are present in large amount due to the valence-anti-quarks of the antiproton. This

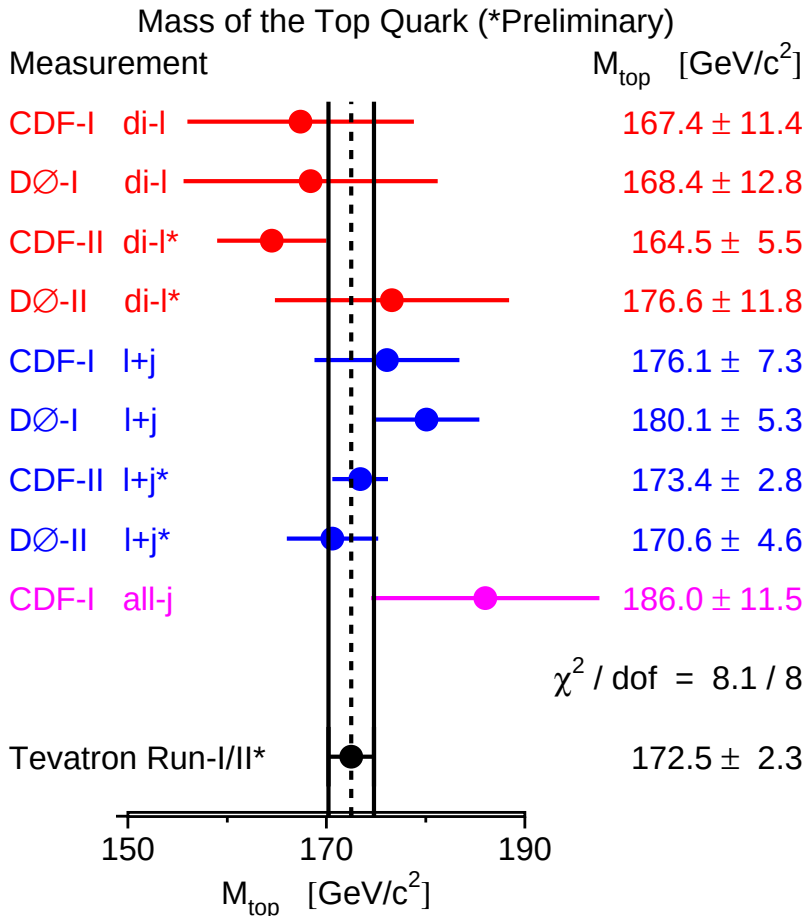

Figure 5.4: The measurements of the top mass and their average

makes the s-channel annihilation process (top left in FIG. 5.1) the most important $t\bar{t}$ production process in proton anti-proton collisions. It contributes 90% of the total $t\bar{t}$ production cross-section at Tevatron.

In proton-proton collisions at LHC no valance-anti-quarks are present and the sea-anti-quarks of the colliding protons are predominantly of low x. Sea-gluons of the colliding protons generally carry larger fractions of the proton momentum than the sea quarks. This and the larger gluon coupling make the gluon-gluon fusion the dominant $t\bar{t}$ production process at the LHC. The s-channel graph shown in FIG. 5.1 on top right has the largest contribution to the $t\bar{t}$ production cross-section, but also the t-channel processes shown in the bottom of FIG. 5.1 contribute substantially. Gluon-gluon fusion in total contributes 90% of the total $t\bar{t}$-pair production cross-section at the LHC. The total cross section prediction at

next-to-next-to-leading order (NNLO) including soft gluon corrections is $\sigma_{t\bar{t}} = 873$ pb for $m_t = 175$ GeV [35].

Besides the production of $t\bar{t}$-pairs, top quarks are also produced in hadron collisions as single quarks via processes of the weak interaction. The dominant Feynman-diagrams for single-top production at the LHC are shown in FIG. 5.2. Single-top production provides an additional field for studies of the properties of top quarks. However, as the final state of these events contains only one top quark, these processes are not studied in this analysis.

5.1.3 Decay Modes

The top quark has only a very short decay-time of the order of 10^{-25}s. The decay time of the top quark is much shorter than the typical time-scale for hadronisation processes. Therefore, strong interactions may influence the final state of the top quark, but hadrons containing top quarks are not formed [36]. In the SM, the top quark decays almost always into a b-quark and a W-boson. The relevant CKM coupling V_{tb} is determined by the (three-generation) unitarity of the CKM matrix. Rare decays and CP violation are unmeasurable small in the SM [37].

Although the direct decay of the top quarks into a b-quark and a W-boson is fully determined, the produced W-boson itself decays, too. The W-decays are usually distinguished into hadronic decays, where the W-boson decays into a $q\bar{q}'$ pair and leptonic decays, where the W-boson decays into a charged lepton and the corresponding neutrino. Usually only the (by experimental definition) stable leptons e and μ are considered here, whereas the decay into an instable τ, which itself could decay hadronically forms a special case. In the following the most important decay channels of $t\bar{t}$ events are discussed.

Multi-Jet (Full-Hadronic) Channel

The largest sample of $t\bar{t}$ events consists of the topology $t\bar{t} \rightarrow W^+W^-b\bar{b} \rightarrow (jj)(jj)b\bar{b}$. The product of branching ratios of about $6/9 \times 6/9 \simeq 44.4\%$ implies the production of 3.7 million multi-jet events for an integrated luminosity of 10fb^{-1} at LHC . The final state consists of 6 high p_T-jets, two of them being b-jets and no energetic neutrinos. Despite having the largest branching ratio and the most kinematic constraints due to a completely visible final state, this decay channel suffers from QCD light jets background and ambiguities in the assignment of the jets to the originating $t\bar{t}$ decays. In addition, the all-jets channel posses difficulties for triggering [37].

Single Lepton + Jets (Semi-Leptonic) Channel

The single lepton plus jets topology, $t\bar{t} \to W^+W^-b\bar{b} \to (l\nu)(jj)b\bar{b}$ arises in $2 \times 2/9 \times 6/9 \simeq 29.6\%$ of all $t\bar{t}$ events. At LHC for an integrated luminosity of $10 fb^{-1}$ almost 2.5 million events are expected. The presence of a high-p_T isolated lepton provides an efficient trigger. The lepton and the high value of E_T^{miss} give a good discrimination against backgrounds like QCD light jets and $b\bar{b}$ production. For the single lepton plus jets sample it is possible to fully reconstruct the final state by setting the $m\nu = 0$, assigning $E_T^{\nu} = E_T^{\text{miss}}$ and calculating p_{ν}^{z} with a quadratic ambiguity, by applying the constraint that $m_{l\nu} = m_W$.

Di-Lepton Channel

In the di-lepton topology both W's decay leptonically, providing a particularly clean sample of $t\bar{t}$ events. Di-lepton events are characterised by two energetic, isolated leptons of opposite charge, two energetic b-jets and missing transverse energy E_T^{miss}. The branching ratio is small $2/9 \times 2/9 \simeq 4.9\%$. With this branching ratio $400,000$ di-lepton events are expected for an integrated luminosity of 10fb^{-1}. Even if the branching ratio is small, pure event samples can be obtained requiring the two leptons in the event to be reconstructed. The reconstruction and selection of $t\bar{t}$ events is based on reconstructing the directions and energies or momenta of isolated electrons or muons and jets, and on reconstructing the missing transverse energy E_T^{miss} from the transverse momentum balance in the event. The purity of the event sample can be enhanced by identifying jets that originated from a b-quark (b-tagging), since in the SM every $t\bar{t}$ event contains two b-jets [38, 39].

5.1.4 Top quark mass measurements

A fundamental parameter of the Standard Model is the mass of the top quark m_t. It should therefore be measured as precisely as possible. Also in the SM, the masses of the W and Higgs gauge bosons are related to m_t through radiative corrections. Furthermore, a high level of accuracy on the top mass value (for example $\delta m_t \leq 1\text{GeV}$) is desirable both within the SM and MSSM framework [15, 16].

In the SM such an accuracy would significantly improve the precision on the W-boson mass prediction while in MSSM it would put constraints on the parameters of the scalar top sector and would therefore allow sensitive tests of the model by comparing predictions with direct observations. Because the top quark, as other

quarks, cannot be observed as a free particle, the top quark mass is a purely theoretical notion and depends on the concept adopted for its definition [39]. Experimentally, the top quark mass has been defined by the position of the peak in the invariant mass distribution of the top quarks decay products, a W-boson and a b-quark jet. This closely corresponds to the pole of the top quark, defined as the real part of the pole in the top quark propagator.

FIG. 5.3 shows the measured values for the top and W masses compared with their mutual dependence as predicted by the SM or an unconstrained SUSY model. The dashed line shows the 68% confidence level limits in the (m_W, m_t)-plane, for the indirect (LEP1, SLD data) and direct (LEP2, $p\bar{p}$ data) determination in a global fit to electro-weak precision data [40].

Summarised top mass measurements at D0 and CDF experiments at Fermilab using the combined Run-I (1992-1996) measurements with the most recent preliminary Run-II (2001-present) measurements using up to 750pb^{-1} of data give a top quark mass known with a precision of 1.3%, a 20% improvement relative to the previous combination. Taking correlated uncertainties properly into account the resulting preliminary world average of the top quark mass is [41]

$$m_t = 172.5 \pm 1.3(\text{stat.}) \pm 1.9(\text{syst.})\text{GeV} \tag{5.1}$$

which corresponds to a total uncertainty of 2.3GeV as shown in FIG. 5.4.

5.1.5 Spin Correlations

An important property of the top quark is that its spin orientation is transferred to its decay products and should be directly observable. Due to the large mass of the top quark, it decays on a time scale ($\tau \sim 10^{-24}$ s) much smaller than the time in which hadronisation can take place. As a consequence, the spin orientation of the top quark should be preserved in its decay. If the top quark would hadronise, the spin information would be lost when the quark depolarises in mesons. Hence, direct observation of a quark spin is only possible in top quark decays.

Top quark pairs produced at LHC will have correlated spins most of the time [42]. Specifically, the top and anti-top will both have right-handed helicity $t_R\bar{t}_R$, or both have left-handed helicity $t_L\bar{t}_L$ with a probability of around 65%. The angular distribution of the top decay products can be used to analyse the spin of the top quarks, measure the degree of spin correlation and look for possible anomalous couplings and CP violation [43]. There are many methods to investigate the spin correlations [37]. One method will be to look at the opening angle

between the two oppositely charged leptons, $\cos\theta_u$, in the "di-lepton" channel ($t\bar{t} \rightarrow (bl\nu)(bl\nu)$) which is sensitive to the amount of spin correlation. Other methods include looking at the "lepton + jets" channel, reconstructing the $t\bar{t}$ system, and measuring the angular distributions of the decay products directly.

5.1.6 Single top

As mentioned already, top quarks are produced in pairs through the strong interaction. In the weak interaction, top quarks are produced together with a b-quark in the final state, or with a W-boson through bg fusion. These types of processes are called single top production. Although non-dominant, the single top production represents a third of the total top quark pair production. While a 5σ-evidence of single-top events at the Fermilab $p\bar{p}$ collider seems to be achievable with 2.4fb^{-1}, precise measurements will only be possible at the LHC [34]. The main interest in the single top production is the possibility to directly determine the coupling strength for the t-W-b vertex and to measure the coupling constant of $W^+ \rightarrow \bar{b} + t$, V_{tb}, at the 1% level of precision. The single top cross-section is unambiguously predicted by the SM (apart from the coupling), and it is an important test to cross check the W-gluon fusion, Wt and W^* cross-sections separately. The single top production constitutes a powerful probe for new physics, the W^* channel is sensitive to an additional heavy $W^{'}$ boson, since new s-channel diagrams in which the $W^{'}$ is exchanged would occur. In contrast, additional contributions to the W-gluon fusion process for new t-channel diagrams with a $W^{'}$ would be suppressed by $\frac{1}{m^2_{W'}}$. On the other hand the W-gluon fusion process channel is more sensitive to modifications of the top quark's coupling to the other SM particles [16, 34]

5.2 MSSM Higgs Physics at the LHC

5.2.1 MSSM Higgs Production at the LHC

Introduction

As discussed in the chapter Standard Model and Beyond, the Higgs sector of the MSSM contains two charged $H^{\pm}$ and three neutral (h, H, A) mass eigenstates. At the tree level, the masses and couplings of all Higgs bosons depend on only two parameters, which can be chosen as e. g. the mass of the CP-odd boson m_A

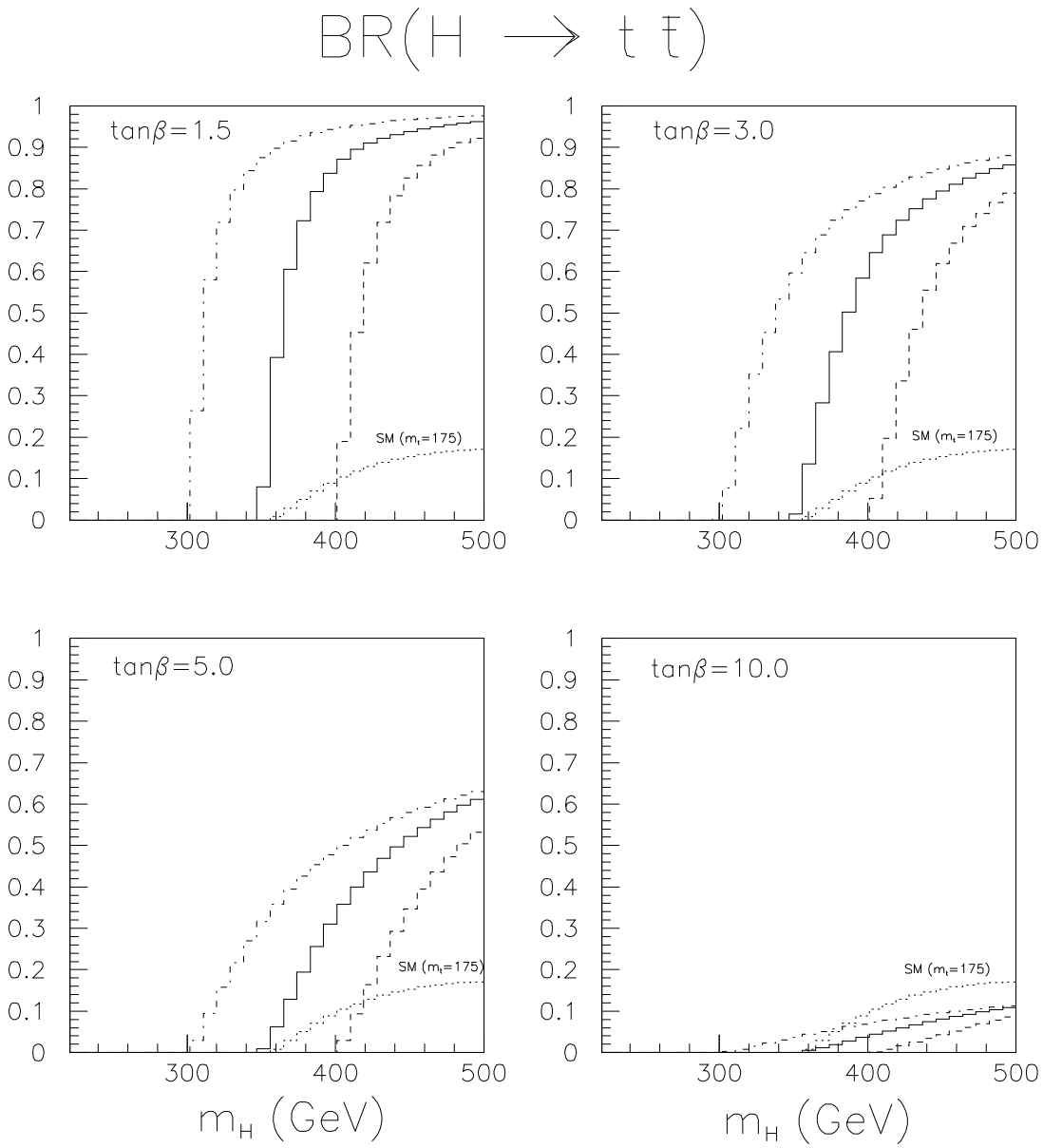

Figure 5.5: $H \to t\bar{t}$ branching ratio as a function of m_H for four values of $\tan\beta$. The solid line is for $m_t = 175$GeV, the dashed line for $m_t = 200$GeV and the dot-dashed one for $m_t = 150$GeV. The figures also show the standard model prediction SM for $m_t = 175$GeV (dotted line) [44]

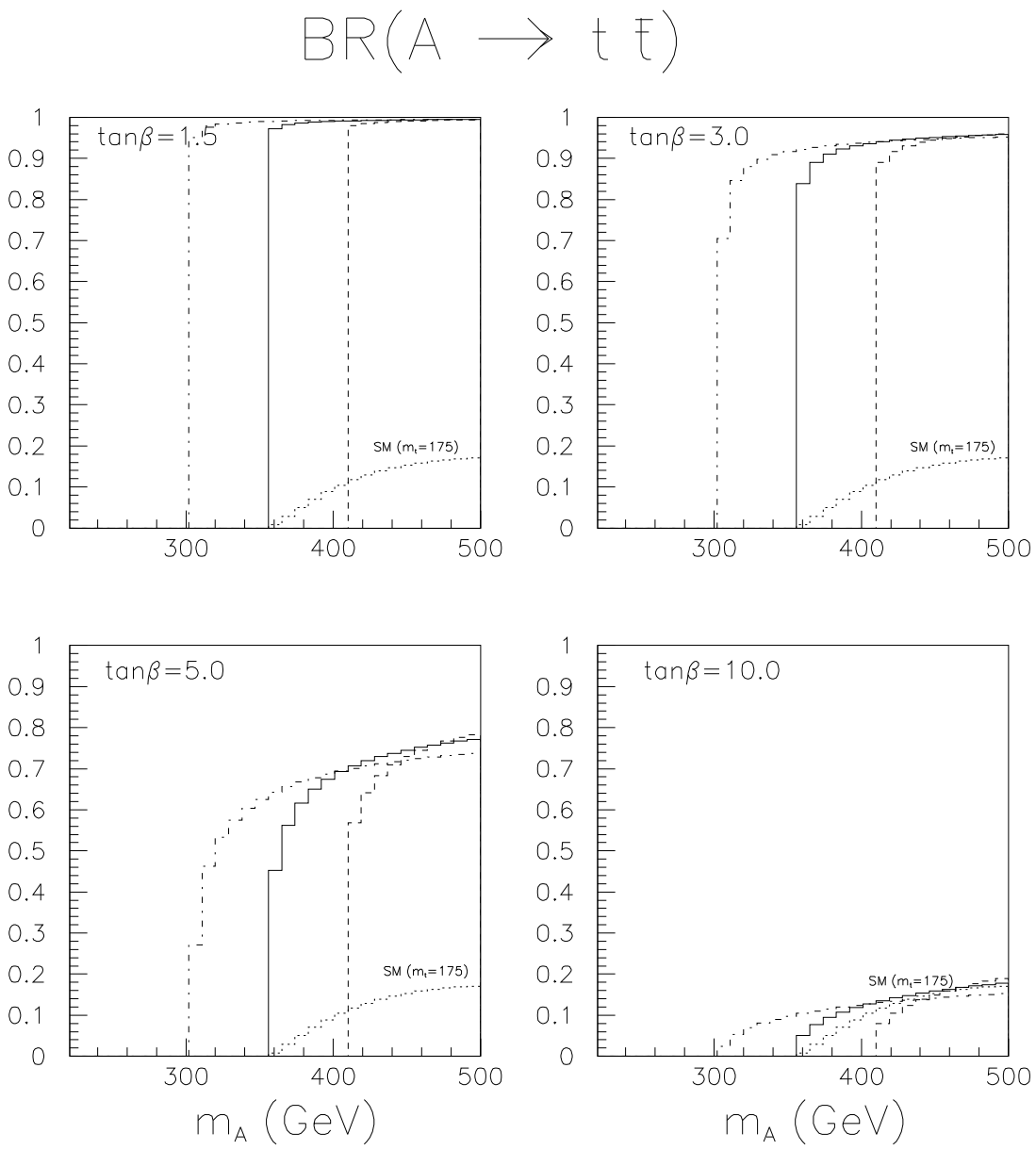

Figure 5.6: $A \to t\bar{t}$ branching ratio as a function of m_A for four values of $\tan\beta$. The solid line is for $m_t = 175$GeV, the dashed line for $m_t = 200$GeV and the dot-dashed one for $m_t = 150$GeV. The figures also show the standard model prediction SM for $m_t = 175$GeV (dotted line) [44]

and the ratio of the vacuum expectation values of the two Higgs doublets $\tan\beta$. A complete study is therefore more complicated than in the Standard Model, where the only free parameter is the Higgs mass. In addition, when considering production and decay of the Higgs bosons, the whole particle spectrum of the super-symmetric model has to be considered, as the R-odd particles (squarks, sleptons, gauginos, higgsinos) may play an important role. The total decay widths of the MSSM Higgs bosons differ significantly from that of the SM Higgs boson of the same mass. The decay width of the h-boson in the MSSM is usually larger than that of a SM Higgs boson of the same mass and is increasing significantly with $\tan\beta$. However, the h-boson width will nevertheless always be smaller than the experimental resolution for the signatures accessible at LHC.

We consider heavy Higgs bosons which decay into $t\bar{t}$, therefore $m_{H,A} \gg m_Z$. In this case, $m_A \sim m_H$ and g_{HZZ} is small. The decay widths of the H-boson and A-boson are very similar for $m_H = m_A$. They become large (3-25 GeV) for large values of m_H, m_A and of $\tan\beta$ and will have to be taken into account when studying the channels accessible in this region of parameter space [44].

The H-boson

The H-boson is the heavier of the CP-even neutral MSSM Higgs bosons. In the MSSM the spectrum of decay channels is much richer and varies strongly with m_A and $\tan\beta$. This is due to the strong suppression of the HZZ coupling, which enhances the branching ratios to other decay channels, such as $H \to \tau\tau$ and $H \to t\bar{t}$. As seen in FIG. 5.5, the $H \to t\bar{t}$ channel is the dominant one for low values of $\tan\beta$ and for $m_H > 2m_t$. For higher values of $\tan\beta$, the $H \to t\bar{t}$ channel is comparable to the $H \to b\bar{b}$ decay channel, and its branching ratio is reduced to less than 10% for $\tan\beta = 10$.

A-boson

The CP-odd neutral Higgs boson, the A-boson, is degenerate in mass with the H-boson over a large fraction of the $(m_A, \tan\beta)$ plane. Many of the interesting final states $(t\bar{t}, \tau^+\tau^-, \mu^+\mu-)$ would therefore be observable only for the H and A-boson together. The absence of tree-level couplings of the A-boson to gauge-boson pairs has important implications for the predictions. As shown in FIG. 5.6, the $A \to t\bar{t}$ channel is the dominant one for low values of $\tan\beta$ and for $m_A > 2m_t$. As $\tan\beta$ increases, the $A \to t\bar{t}$ channel competes with the $A \to b\bar{b}$ channel and its branching ratio is reduced to less than 20% for $\tan\beta = 10$, where it is close

to the SM branching ratio.

5.2.2 The Decay $H/A \to t\bar{t}$

In this section the decay of the MSSM Higgs bosons H/A into top quarks will be discussed, concentrating on searches for a Higgs boson with zero or suppressed coupling to the weak vector bosons, via its decay to $t\bar{t}$. H/A particles are expected to be produced in abundance (given their existence) at a hadron collider through gluon-gluon collisions, via a virtual top-quark loop [45] as shown in FIG. 5.7. However, at a hadron collider there is a large irreducible background from the QCD production of top quarks as seen in FIG. 5.8. Moreover, the signal $gg \to H/A \to t\bar{t}$ and the background $gg \to t\bar{t}$ interfere (see FIG. 5.9), generically resulting in a peak-dip structure at the Higgs mass. This phenomenon was first predicted in [46]. In some cases the dip dominates, such as the signal for the presence of the Higgs boson is a small deficit in the production of $t\bar{t}$-pairs of invariant mass near the Higgs mass.

Taking into account only the scalar Higgs particle H, the differential cross-section for $gg \to t\bar{t}$, including the squares of the scalar-Higgs amplitude and the continuum QCD amplitude, as well as the interference term of the two amplitudes is given as [47]

$$\begin{aligned}\frac{d\sigma}{dz} &= \frac{\alpha_s^2 G_F^2 m_t^2 s^2}{1536\pi^3}\beta^3 \left|\frac{N(s/m_t^2)}{s - m_H^2 + im_H\Gamma_H(s)}\right|^2 - \frac{\alpha_s^2 G_F m_t^2 s}{384\pi\sqrt{2}}\beta^3\left(\frac{1}{p_1\cdot p_3} + \frac{1}{p_2\cdot p_3}\right) \\ &\quad \times Re[\frac{N(s/m_t^2)}{s - m_H^2 + im_H\Gamma_H(s)}] + \frac{d\sigma_{QCD}}{dz} \qquad (5.2)\end{aligned}$$

where $p_{1,2}$ are the momenta of the incoming gluons, $p_{3,4}$ are the outgoing top-quark and top-anti-quark momenta, z is the cosine of the scattering angle between an incoming gluon and the top quark, m_t is the top-quark mass, and $\beta \equiv (1 - 4m_t^2/s)^{1/2}$ is the velocity of the top-quark and top-anti-quark in the centre of momentum frame. The dot product of the four momenta are

$$p_1 \cdot p_3 = \frac{1}{4}(1 - \beta z) \qquad (5.3)$$

$$p_2 \cdot p_3 = \frac{1}{4}(1 + \beta z) \qquad (5.4)$$

The function

$$N(s/m_t^2) = \frac{3}{2}\frac{m_t^2}{s}\left[4 - \left(1 - \frac{4m_t^2}{s}\right) I(s/m_t^2)\right] \qquad (5.5)$$

is associated with the virtual top-quark loop, where

$$I(s/m_t^2) = \left[\ln\frac{1+\beta}{1-\beta} - i\pi\right]^2 \text{ with } (s > 4m_t^2) \tag{5.6}$$

The energy dependent Higgs width $\Gamma_H(s)$ is given by the relation

$$m_H\Gamma_H(s) = \frac{3G_F m_t^2 s}{4\pi\sqrt{2}}\beta^3 \quad . \tag{5.7}$$

The cross section for the continuum QCD production of $gg \to t\bar{t}$ is:

$$\begin{aligned}\frac{d\sigma_{QCD}}{dz} &= \frac{\pi\alpha_s^2}{12s}\beta\left(\frac{s^2}{(p_1\cdot p_3)(p_2\cdot p_3)} - 9\right) \\ &\quad\times\left[\frac{(p_1\cdot p_3)^2}{s^2} + \frac{(p_2\cdot p_3)^2}{s^2} + \frac{m_t^2}{s} + \frac{m_t^4}{4p_1\cdot p_3 p_2\cdot p_3}\right]\end{aligned} \tag{5.8}$$

The total cross-section is obtained from Eq. 5.2 by integrating over z, the cosine of the scattering angle between a gluon and the top-quark. The total cross-section comes out as

$$\sigma_{\text{total}}^{H0} = \sigma_{\text{QCD}} + \sigma_{H^0}^{\text{Higgs}} - \sigma_{H^0}^{\text{interference}} \tag{5.9}$$

with

$$\begin{aligned}\sigma_{\text{QCD}} = \pi\frac{\alpha_s^2}{12}\frac{\beta}{s}\left[\frac{1}{\beta}\log\left(\frac{1+\beta}{1-\beta}\right)\left(4 + 16\frac{m_t^2}{s} + 4\frac{m_t^4}{s^2}\right) - 6.25 - 0.75\beta^2\right. \\ \left. -64\frac{m_t^4}{s^2}\frac{1}{1-\beta^2} - 18\frac{m_t^2}{s}\right]\end{aligned} \tag{5.10}$$

and

$$\begin{aligned}&\sigma_{H^0}^{\text{Higgs}} = \alpha_s^2 G_F^2\beta^3\frac{3}{1024\pi^3}\cdot\frac{1}{\left[(s-m_H^2)^2 + \left(\frac{3G_F\beta^3 s m_t^2}{4\pi\sqrt{2}}\right)\right]^2} \\ &\cdot\left\{\left[4 + \left(\frac{4m_t^2}{s} - 1\right)\left(\log\left(\frac{1+\beta}{1-\beta}\right)^2 - \pi^2\right)\right]\right. \\ &(s-m_H^2) + \log\left(\frac{1+\beta}{1-\beta}\right)\left(1 - 4\frac{m_t^2}{s}\right)\frac{3G_F m_t^2 s\beta^3}{\sqrt{8}}\Bigg\}^2 \\ &\left\{2\pi\log\left(\frac{1+\beta}{1-\beta}\right)\left(1 - 4\frac{m_t^2}{s}\right)(s-m_H^2) - \right. \\ &\qquad\left.\left[4 - \left(1 - \frac{4m_t^2}{s}\right)\left(\log\left(\frac{1+\beta}{1-\beta}\right)^2 - \pi^2\right)\right]\frac{3G_F m_t^2 s\beta^3}{4\pi\sqrt{2}}\right\}^2\end{aligned} \tag{5.11}$$

as well as

$$\sigma_{H^0}^{\text{interference}} = \alpha_s^2 G_F \frac{\beta^2}{32\pi\sqrt{2}} \frac{m_t^4}{s} \frac{\log\left(\frac{1+\beta}{1-\beta}\right)}{\left(\left(s-m_H^2\right)^2 + \left(\frac{3G_F m_t^2 s\beta^3}{4\pi\sqrt{2}}\right)^2\right)}$$
$$\times \left\{ \left[4 + \left(1 - 4\frac{m_t^2}{s}\right)\left(\pi^2 - \log\left(\frac{1+\beta}{1-\beta}\right)^2\right)\right]\left(s-m_H^2\right) \right.$$
$$\left. + \frac{3G_F m_t^2 s\beta^3}{\sqrt{8}} \log\left(\frac{1+\beta}{1-\beta}\right)\right\} \quad . \quad (5.12)$$

In FIG. 5.10 the cross sections for $gg \to t\bar{t}$ as a function of the $t\bar{t}$ invariant mass, $\sqrt{s}$, for $m_t = 175GeV$ and for $m_H = 400, 500, 600, 700$ and $800GeV$ is shown. For $m_H = 400$GeV, the Higgs boson produces a narrow peak with a width of about 2.7GeV. For $m_H = 500$GeV and 600GeV, the presence of the Higgs boson produces a peak, followed by a dip near the Higgs mass caused by the interference. For larger Higgs masses the peak is absent, and the presence of a Higgs boson reveals itself as a dip in the $t\bar{t}$ invariant mass spectrum. For $m_H = 500$GeV, the total top-quark cross section differs little from the cross section with no Higgs present due to the cancellation between the peak and the dip. For larger Higgs masses the presence of the Higgs results in a small decrease in the total top-quark cross section.

Like the scalar H, the pseudo-scalar Higgs boson does not couple to the weak vector bosons, and couples to the top quark with SM strength if the ratio of vacuum-expectation values of the two Higgs doublets is close to unity.

The differential cross section for $gg \to t\bar{t}$, including the squares of the pseudo-scalar Higgs amplitude and the continuum QCD amplitude, as well as the interference of the two amplitudes is

$$\frac{d\sigma}{dz} = \frac{3\alpha_s^2 G_F^2 m_t^2 s^2}{2048\pi^3}\beta \left| \frac{P(s/m_t^2)}{s - m_A^2 + im_A\Gamma_A(s)} \right|^2 - \frac{\alpha_s^2 G_F m_t^2 s}{256\pi\sqrt{2}}\beta\left(\frac{1}{p_1\cdot p_3} + \frac{1}{p_2\cdot p_3}\right)$$
$$\times Re[\frac{P(s/m_t^2)}{s - m_A^2 + im_A\Gamma_A(s)}] + \frac{d\sigma_{QCD}}{dz} \quad (5.13)$$

There is no interference between the scalar Higgs H and the pseudo-scalar Higgs A amplitudes due to the opposite parities. The function associated with the virtual top-quark loop is

$$P(s/m_t^2) = -\frac{m_t^2}{s} I(s/m_t^2) \quad (5.14)$$

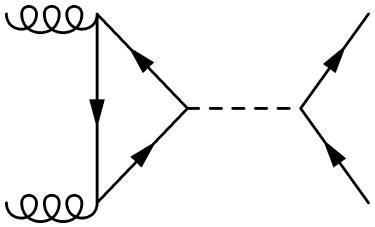

Figure 5.7: $t\bar{t}$ pair production through gluon fusion with an intermediate Higgs boson

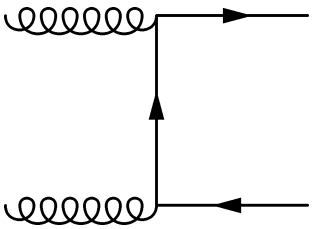

Figure 5.8: $t\bar{t}$ pair production through gluon fusion

The energy dependent Higgs width is given by:

$$m_A \Gamma_A(s) = \frac{3 G_F m_t^2 s}{4\pi\sqrt{2}} \beta \tag{5.15}$$

The total cross section is obtained from the expression Eq. 5.13 by integrating over z, the cosine of the scattering angle between a gluon and the top-quark. It comes out as

$$\sigma_{\text{total}}^{A0} = \sigma_{\text{QCD}} + \sigma_{A^0}^{\text{Higgs}} - \sigma_{A^0}^{\text{interference}} \tag{5.16}$$

with

$$\sigma_{A^0}^{\text{Higgs}} = \frac{3\alpha_s^2}{1024\pi^3} m_t^6 \beta G_F^2 \cdot \frac{\left[\log\left(\frac{1+\beta}{1-\beta}\right)^2 - \pi^2\right]^2 + 4\pi^2}{(s - m_A^2)^2 + \left(\frac{3 G_F m_t^2 \beta s}{4\pi\sqrt{2}}\right)} \tag{5.17}$$

and

$$\begin{aligned}\sigma_{A^0}^{\text{interference}} = &-\frac{\alpha_s^2}{32\pi\sqrt{2}} \frac{m_t^4}{s} G_F \frac{\log\left(\frac{1+\beta}{1-\beta}\right)}{(s - m_A^2)^2 + \left(\frac{3 G_F m_t^2 \beta s}{4\pi\sqrt{2}}\right)} \\ &\cdot \left\{ \log\left(\frac{1+\beta}{1-\beta}\right)^2 (s - m_A^2) - \frac{3 G_F m_t^2 s \beta}{\sqrt{8}} - \pi^2 (s - m_A^2) \right\}\end{aligned} \tag{5.18}$$

The resulting cross sections shown in Fig. 5.11 are qualitatively similar to the cross sections calculated for the scalar Higgs. The pseudo-scalar Higgs width is suppressed by β, rather than β^3 as is the scalar Higgs width, so the pseudo-scalar Higgs boson's mass peak is noticeably wider than the scalar Higgs boson's, especially for $m_{H,A} = 400, 500\text{GeV}$. As already stated above, H and A are degenerate in masses over a large fraction of the parameter space and can in this case only

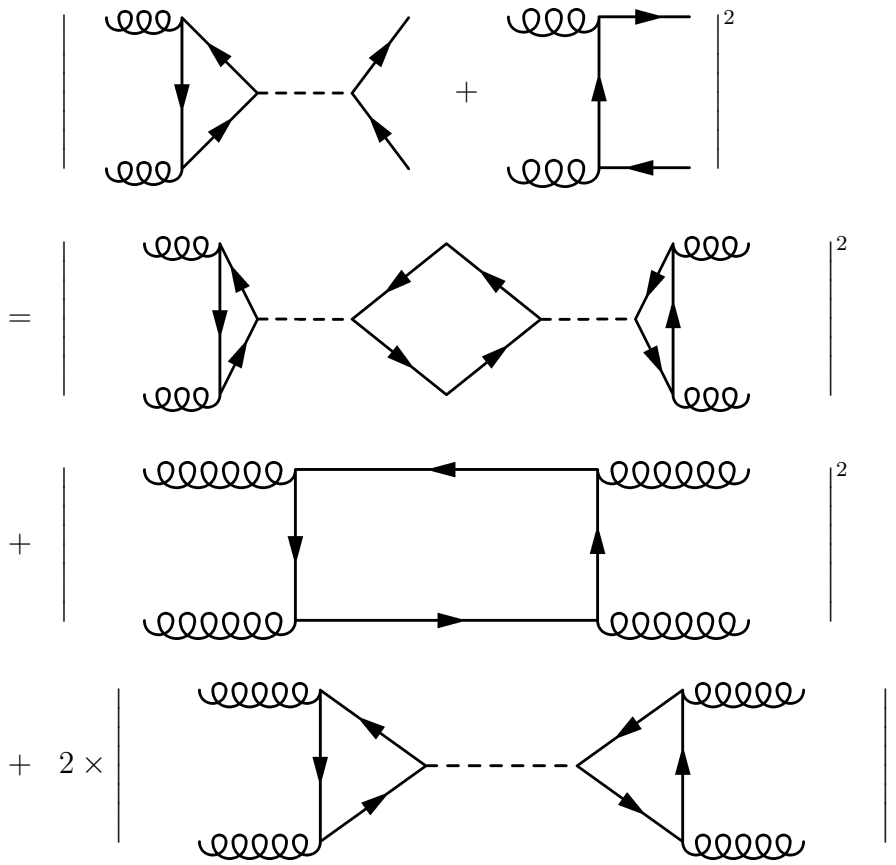

Figure 5.9: Interference between the two $t\bar{t}$ production channels appears when the square of the matrix element is taken

be observed together. In FIG. 5.12, the combined cross-section for the production of H and A bosons for different assumed masses of the two bosons is shown. The shape of the cross-section is similar to that of only H or A production, but the structures in the cross section are more pronounced here. Like in the cross section for the A boson production, the size of the peak and the dip structure are roughly equal also in the combined production cross section for a Higgs mass around 500GeV. Peak-dip structures due to final state interactions are well-known in hadronic physics [48]. This structure in the $t\bar{t}$ invariant mass spectrum results whenever there is a resonant final state interaction of the $t\bar{t}$ pair, regardless of the physics which produces the resonant final state interaction [49]. In this context, the H and the A act similar to a bound state. It was also shown that the peak-dip structure is not washed out by QCD corrections, since it depends only on the final state interaction of the $t\bar{t}$ pair, whose production may in principle be

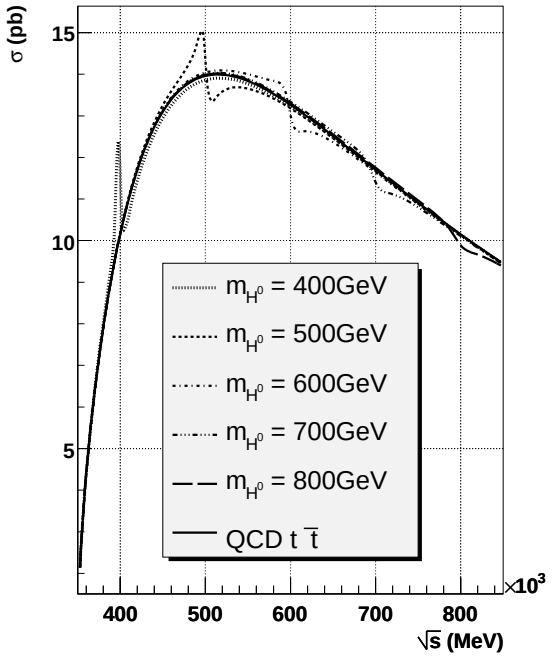

Figure 5.10: The inclusive cross-section for H^0 production as a function of $\sqrt{s}$ for different H^0 masses.

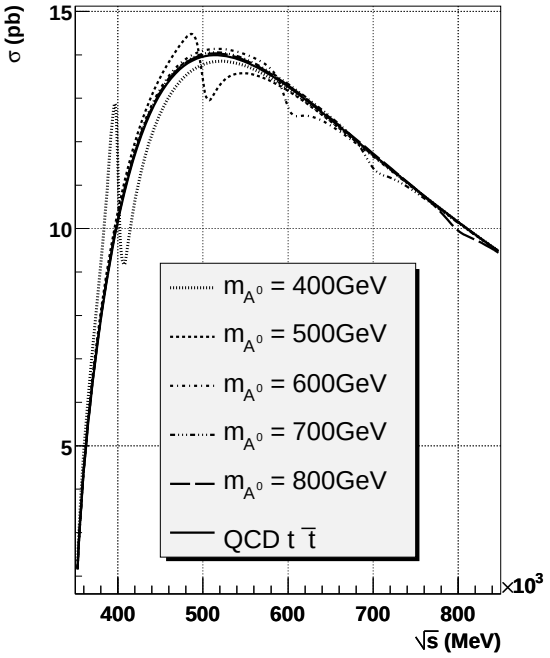

Figure 5.11: The inclusive cross-section for A^0 production as a function of $\sqrt{s}$ for different A^0 masses.

calculated to any order in QCD.

At the Tevatron, Fermilab, a top quark anti-quark pair is predominantly produced via quark-anti-quark annihilation. For example, for $m_t = 170GeV$, the gluon-fusion contribution to the total top-quark cross section is only about 20% [50]. Thus any structure in the $gg \to H/A \to t\bar{t}$ cross section due to the Higgs boson would be buried underneath the $q\bar{q} \to t\bar{t}$ continuum, and requires a very large statistics to uncover. In contrast, at a higher energy hadron collider, such as LHC, the gluon-fusion process is the dominant source of top quarks. Even assuming that the $t\bar{t}$ invariant mass distribution can be reconstructed with reasonable resolution, the effect of the scalar and pseudo-scalar Higgs bosons on the $t\bar{t}$ invariant mass distribution will be quite small and requires large statistics to be observed. For example, the peaks in FIG. 5.10 due to a scalar Higgs of mass 500GeV are each about a 10% effect, each contained in a bin of width about 25GeV. The statistical significance of the peak and dip depends on the number of $t\bar{t}$ events in the mass bin containing the signal.

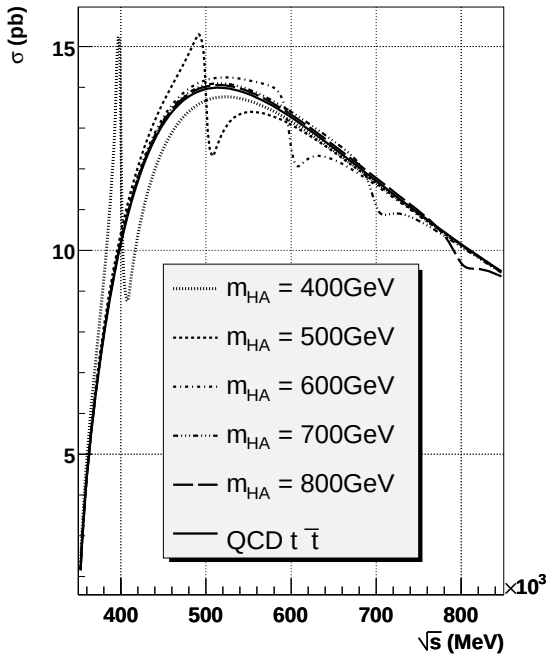

Figure 5.12: The inclusive cross-section for the production of degenerate H^0 and A^0 as a function of $\sqrt{s}$ for different H^0/A^0 masses.

Chapter 6

Analysis

In this study the prospects of analyses of top events and resonances decaying into top quarks with the fully hadronic final state are investigated. The fully hadronic final state is the kinematically most constrained decay mode of $t\bar{t}$ pairs and has the highest branching ratio. However, the final state of this decay mode consists of jets of hadrons which due to final state interactions only approximately represent the properties of the original partons coming out of the primary hard interaction. Moreover, the existence of at least six jets in the final state allows for a large number of permutations of the assignment of the jets to the top quark or anti-top quark. The largest challenge is still the enormous amount of QCD multi-jet background events with the $2 \cdot 10^8$ times larger total cross-section.

In the analysis presented here, simulated events in which H/A-bosons of an assumed mass of 500GeV decay into $t\bar{t}$-pairs, which in turn decay fully hadronically are studied. Because of the occurring interference between this production process and the production of $t\bar{t}$-pairs by strong interactions in gg fusion [47], which is caused by the common initial and final state, these two event types cannot be studied separately. Therefore a corresponding sample of QCD produced $t\bar{t}$-events has been simulated. Moreover, a large sample of QCD multi-jet events which form the main background to fully hadronically decaying $t\bar{t}$-pairs, is simulated.

The composition of the event samples is discussed in Sect. 6.1. In order to reconstruct the invariant mass of the initial $t\bar{t}$-pair of these events, a kinematic fit procedure is applied which is described in Sect. 6.2. For the separation of the QCD multi-jet events from the $t\bar{t}$-events, a neural network is applied. The training and the properties of the neural network and the applied cuts are discussed in Sect. 6.3. In order to search for a Higgs contribution to the distribution of invariant $t\bar{t}$-masses from the event sample accepted by the neural network, this

distribution is compared to the theoretical predictions presented in SECT. 5.2 and a χ^2-test is performed. By comparing the data sample without any Higgs contribution to the prediction which includes such a contribution, the expected upper mass limit for the possibility to exclude a Higgs contribution to the data sample at the LHC is derived. Likewise, comparing this prediction to the full data sample including a Higgs contribution illuminates the signature to be expected, if such a contribution is present. In a first step these comparisons are done for the idealised case that the jets which stem from $t\bar{t}$-decays are known and where no background due to QCD multi-jet events is present in order to study the limits of this approach. In a next step, the analysis is applied to a full data sample with a background of QCD multi-jet events while experimentally accessible assumptions are employed to determine the relevant jets in a given event. This analysis procedure is described in SECT. 6.4.

6.1 Event Sample

The event sample is generated using Pythia 6.221 and passed through the ATLFAST detector simulation using ATHENA version 8.7.0. The event sample contains QCD multi-jet events, QCD produced $t\bar{t}$-events and events where MSSM Higgs H^0/A^0 bosons decay into a $t\bar{t}$ pair. The used event generator Pythia has been discussed in chapter CHAP. 4. For the event generation a top mass of 175 GeV consistent with the present mass measurements [14] is assumed. The mass of the simulated H/A bosons is set to 500GeV in agreement with expectations for the scalar/pseudo-scalar MSSM Higgs when tests for a small value of the ratio of the vacuum expectation values ($\tan\beta \simeq 1.5$) are made. For an integrated luminosity $\mathcal{L} = 35.8\text{fb}^{-1}$ corresponding to one year data taking at medium luminosity, around 40,000 fully hadronic H^0/A^0 events are to be expected.

For the same luminosity around 8,000,000 fully hadronic QCD produced $t\bar{t}$ events are expected as irreducible background. The cross-section for QCD multi-jet events is eight orders of magnitude larger than the $t\bar{t}$ cross-section and especially increases in the very forward region of the detector.

However, events which are concentrated in the forward direction of the detector do not trigger the readout of ATLAS. The most rejecting trigger condition in this context is the LVL1-4J threshold introduced in SECT. 3.3. This trigger condition requires at least four jets with a transverse momentum larger than 65 GeV. Events which fail this condition have no influence whatsoever on any analysis. Therefore the amount of events to be simulated can be reduced substantially by requiring a minimal sum of transverse momenta of the simulated initial hard interaction.

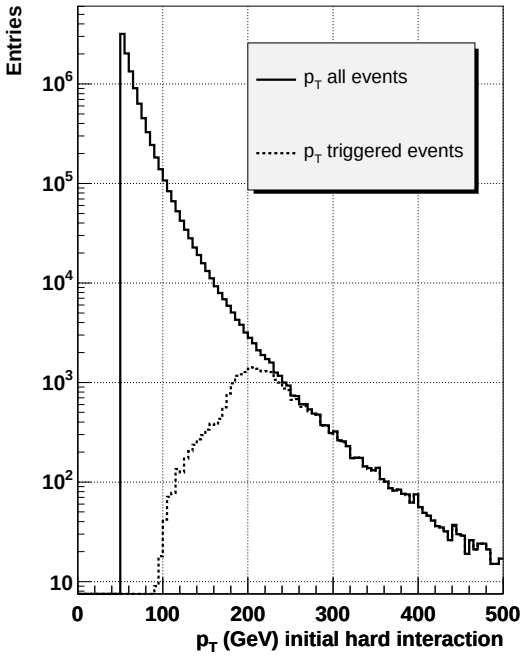

Figure 6.1: The distribution of the p_T of the initial hard interaction of QCD light jet events. The solid line represents all, the dashed line only the triggered events. A cut in the initial hard interaction of $p_T > 50$ GeV has been applied. Only very few events with $p_T < 100$ GeV are triggered.

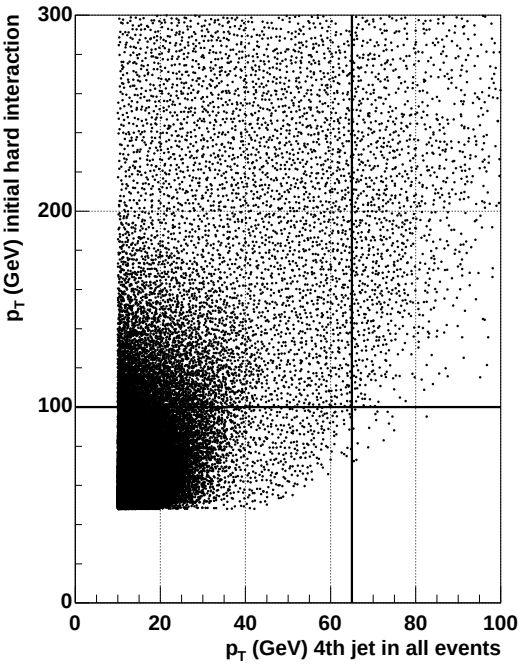

Figure 6.2: The fourth largest p_T of a jet vs. the p_T of the initial hard interaction in QCD light jet events. The solid line indicates the level 1 trigger condition of at least four jets with $p_T > 65$GeV. Only few events which fulfil this condition have a hard interaction with a $p_T < 100$ GeV.

In order to estimate a proper minimal p_T, QCD events are generated using a conservative p_T limit of 50 GeV. This cut already reduces the cross-section of QCD multi-jet events by three orders of magnitude.

In Fig. 6.1 the distribution of the transverse momentum of the initial hard interaction is shown as a solid line. The same distribution for triggered events is indicated by the dash-dotted line. As can be seen, the cut at $p_T > 50$ GeV did not remove any events which would have been triggered. Moreover, a cut at $p_T > 100$ GeV would reduce the number of events to be simulated furthermore substantially, while no significant number of triggered events would be lost.

sample	σ[mb]	N_{evt}
H^0/A^0 ($m = 500$ GeV)	$1.118 \cdot 10^{-9}$	$4.00 \cdot 10^4$
$t\bar{t}$	$2.216 \cdot 10^{-7}$	$7.93 \cdot 10^6$
QCD (no cut)	$5.522 \cdot 10^{-1}$	$1.87 \cdot 10^{13}$
QCD ($p_T > 50$ GeV)	$2.448 \cdot 10^{-2}$	$8.75 \cdot 10^{11}$
QCD ($p_T > 100$ GeV)	$1.389 \cdot 10^{-3}$	$4.97 \cdot 10^{10}$

Table 6.1: Cross-sections and numbers of events for different event samples. The event numbers are calculated for an assumed luminosity of 35.8 fb$^-$1.

In order to understand the connection between initial hard interaction and trigger condition better, in FIG. 6.2 the p_T of the initial hard interaction is plotted against the fourth largest p_T of a jet in an event. Events left of the vertical line at 65 GeV fail the trigger condition. The horizontal line at 100 GeV indicates the possible cut in the initial hard interaction. Only the small fraction of 0.0006% of the simulated events, which is in the lower right quadrant of these two lines are events which would be triggered but are not simulated when the 100 GeV cut is applied. The main part of the multi-jet background is avoided to be simulated, the cross-section is reduced by another order of magnitude to $\sigma = 1.389 \cdot 10^{-3}$ mb. This reduction is essential in order to make the simulation of the QCD light jet background events feasible. Therefore, the cut on the transverse momentum of the initial hard interaction of 100 GeV is applied throughout this analysis when simulating the QCD light jet background. The respective cross-sections calculated with PYTHIA and the number of events corresponding to an integrated luminosity of 35.8fb^{-1} are given in TAB. 6.1.

However, even with this cut in the transverse momentum of the initial hard interaction the cross-section for the production of QCD light-jet events stays too large to simulate the full event sample in an acceptable time. Therefore, only 40,000,000 of the expected events are simulated. The distributions and event rates obtained from this sample have then to be scaled up by a factor of 1242.4 to correspond to the actually expected numbers.

6.2 Kinematic Fit Procedure

The kinematic fit is a mathematical procedure in which the conservation laws governing a particle interaction or decay are used in order to improve the measurements of properties of the process. Being applied on the reconstruction of the

top mass, the kinematic fit is a powerful tool in discriminating events containing top quarks (QCD produced $t\bar{t}$-pairs and resonances decaying into $t\bar{t}$-pairs) from QCD multi-jet background. Kinematic fitting procedures are successfully used by many experiments as they:

- improve jet energy resolution
- help to reconstruct neutrinos and initial or final state photons
- help to find the correct assignments of jets to a decaying particle in an event

For the performed analysis a kinematic fit package called KINFIT [51] is used. It allows one to vary the measured 4-momenta of the jets within the estimated resolution of the jet measurement to fulfill energy and momentum conservation. Further constraints, like the masses of intermediate particles are taken into account by minimising a χ^2 that describes the deviations of the fitted quantities from the constraint values. The constraints applied in order to reconstruct the Higgs mass in the decay into $t\bar{t}$ are the mass of the top quarks as well as the mass of the W-bosons which are produced in the subsequent decay of the top quarks. The mass of the W is assumed to be $m_W = 80.4$ GeV, the mass of the top quarks is assumed to be $m_t = 175$ GeV, both values in agreement with the measurements of these quantities [14].

Events from collisions at LHC contain a large number of jets. To find the correct group of six jets originating in the decay of a $t\bar{t}$-pair is not trivial due to the large combinatorics involved. In a first attempt to apply KINFIT, the information available in the Monte-Carlo simulation is used to give KINFIT only the six jets produced in the decays of the top and the anti-top. The results obtained in this way give an upper limit for the improvement that can be achieved by optimising the selection procedure for the input jets. In a next step, the jets entered into KINFIT are selected using only experimentally accessible information. Here, the two jets which are b-tagged and the four not b-tagged jets with the highest transverse momentum are used as input to KINFIT. The branching ratio for the decay of a W with a b quark or anti-quark among the decay products is very low (0.000601 [9, 20]) so only light jets are considered as candidates for the reconstruction of the W-masses.

In order to allow the kinematic fit to vary the properties of the six selected jets to fit the constraints, it has to be found out, which constraint applies to which subgroup of the jets, i. e. which two light jets are produced by one decaying W and which by the other as well as which of the b jets forms together with which group of two light jets the decay products of a top-quark. In total, six permutations are

possible to divide the jets b_1, b_2, l_1, l_2, l_3 and l_4 into the sets $(bll)_1$ and $(bll)_2$. All six permutations are used as input to the KINFIT algorithm. The permutation which results in the smallest value for the χ^2 of the fit is considered to be the correct one and the resulting invariant $t\bar{t}$-mass is kept.

As input variables for KINFIT the energy, the polar and azimuthal angle of the jets are used. In order for the kinematic fit to vary these jet properties properly, the measurement resolution of these properties is an important input to the fit. This resolution is defined as the difference between the characteristics of the reconstructed jets and the initial quarks. While systematic shifts of these properties can and will be corrected for, the spread of the the difference between the respective values of the quarks and the jets gives an estimate for the resolution of the measurement. The determination of the resolutions is discussed in SECT. 6.2.1.

6.2.1 Jet-corrections and parametrisation of the jet resolution

Due to the process of gluon radiation and hadronisation, the properties of jets are not identical with the properties of the quarks initiating the jets. The information given to the KINFIT algorithm is meant to represent the properties of the quarks at the end of the decay chain $H^0/A^0 \to t\bar{t} \to b\bar{b}q_1q_2\bar{q}_3\bar{q}_4$, while only the properties of the jets are open to measurement. In order for KINFIT to work properly, this difference has to be corrected and the spread of the difference has to be assumed as an uncertainty of the quark-properties derived from the jet measurements. The uncertainty is a measure of how much KINFIT is allowed to vary a given quantity during the fit procedure. The KINFIT algorithm implies a χ^2-fit, so the uncertainties are assumed to correspond to approximately Gaussian errors of the measured jet properties. In order to obtain estimates for Gaussian errors, a Gaussian distribution is fitted to all studied differences of quark and jet properties and the width of the fitted Gaussian is used as an approximation of the Gaussian error.

In order to estimate the difference between the quark and corresponding jet properties, the partons which are decay products of the top quarks have to be mapped to the corresponding jets of hadrons. The conditions chosen to be fulfilled in order to assign a jet to one of the six quarks from the Higgs decay are:

- The distance $\Delta R = \sqrt{\Delta\phi^2 + \Delta\eta^2}$ between this and the nearest other jet should be larger than 0.4 in order to avoid the jets to overlap

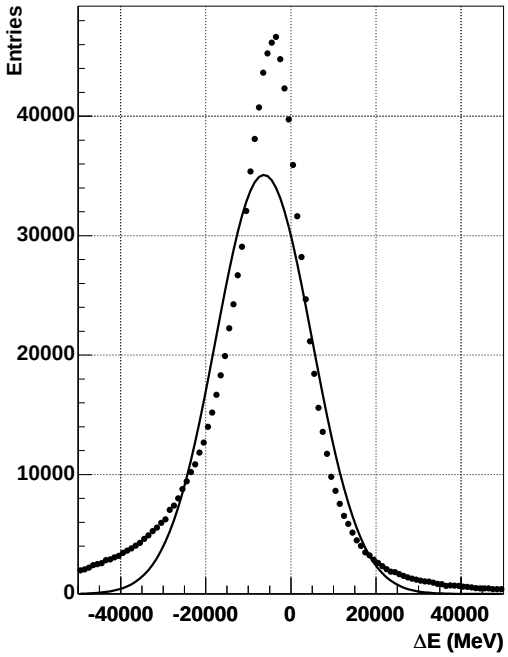

Figure 6.3: The difference between jet and quark energy for light jets.

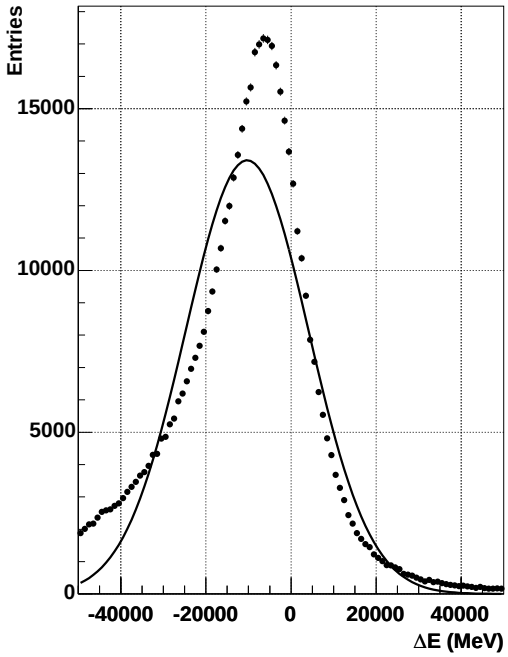

Figure 6.4: The difference between jet and quark energy for b-jets.

- The jet with the smallest distance ΔR to a given quark is assigned to this quark. The distance is required to be less than 0.4.
- A jet is required to be assigned to no more than one quark.

Events in which these conditions cannot be met are discarded. The sample of simulated H/A decays is used to determine the differences. The differences

$$\Delta E = E_{\text{jet}} - E_{\text{quark}} \quad , \tag{6.1}$$

$$\Delta\theta = \theta_{\text{jet}} - \theta_{\text{quark}} \quad \text{and} \tag{6.2}$$

$$\Delta\phi = \phi_{\text{jet}} - \phi_{\text{quark}} \tag{6.3}$$

between the energy and the direction angles θ and ϕ of the assigned jets and the quark are shown in FIG. 6.3, FIG. 6.5 and FIG. 6.7 for the light jets from the decay of the W-bosons and in FIG. 6.4, FIG. 6.6 and FIG. 6.8 for the jets associated to the b-quarks.

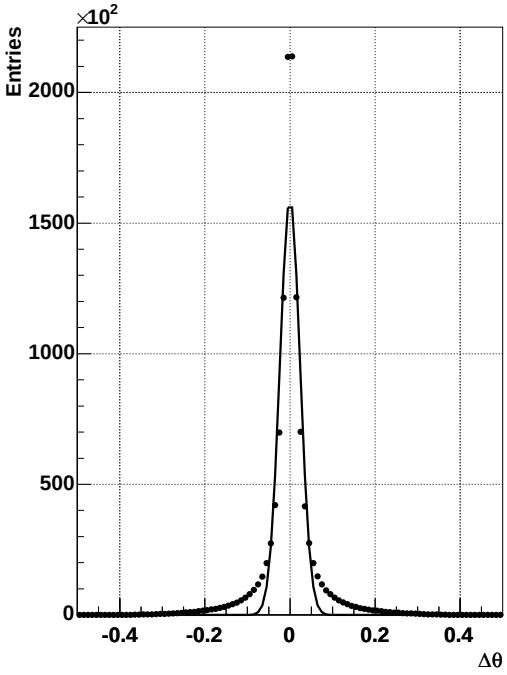

Figure 6.5: The difference between the θ of the jet and the quark for light jets.

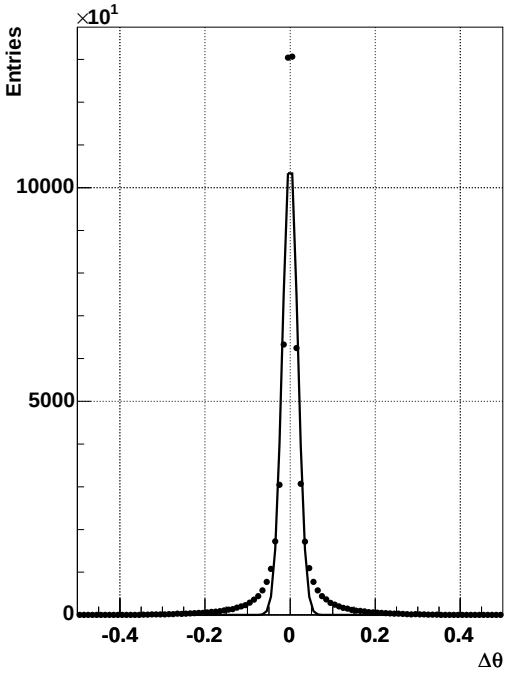

Figure 6.6: The difference between the θ of the jet and the quark for b-jets.

The peak for the energy difference ΔE in FIG. 6.3 and FIG. 6.4 is not centred around zero but shifted towards negative values indicating that the jet energy underestimates the quark energy. The distribution itself is not Gaussian, but shows long, asymmetric tails which extend more into the negative than the positive direction. This effect is due to the radiation of gluons by the quarks. The energy carried away by the gluon may not end up completely in the jet defining cone thus effectively reducing the jet's energy. The shift of the distribution away from zero is a systematic effect for which a correction will be applied, the width of the distribution serves as an estimate of the resolution of the quark energy. For the other two variables, $\Delta\theta$ and $\Delta\phi$, the resolution distribution is centred around zero and its shape is symmetric.

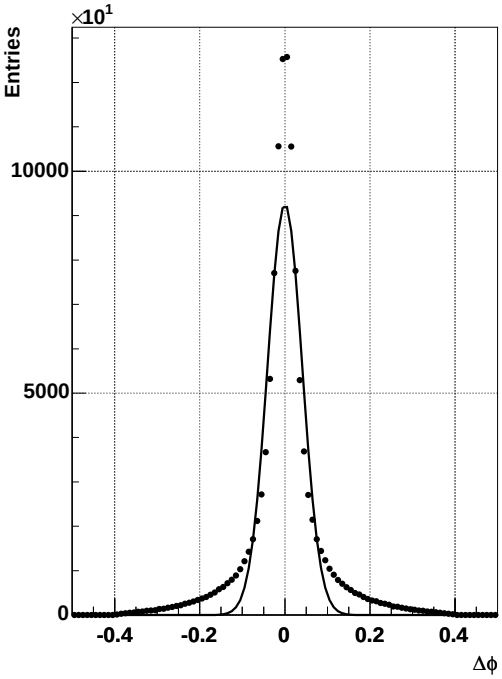

Figure 6.7: The difference between the ϕ of the jet and the quark for light jets.

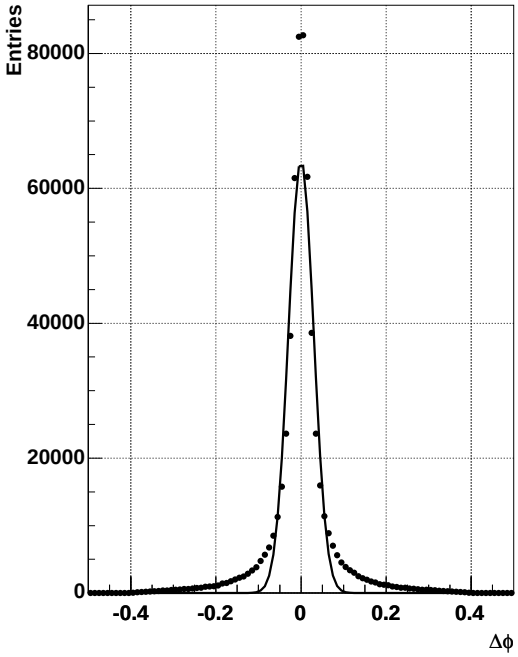

Figure 6.8: The difference between the θ of the jet and the quark for b-jets.

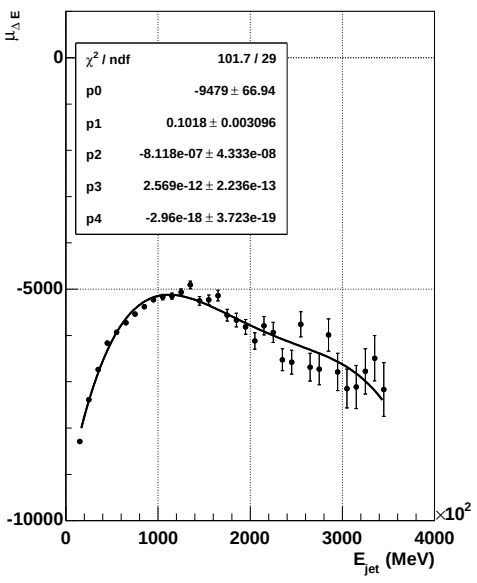

Figure 6.9: The mean value of ΔE as a function of the jet energy for light jets

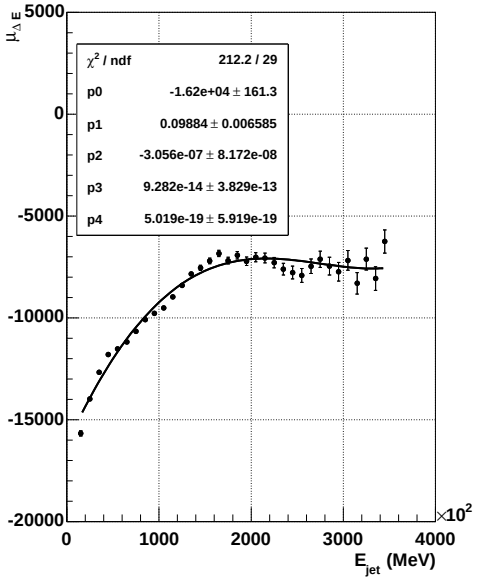

Figure 6.10: The mean value of ΔE as a function of the jet energy for b-jets

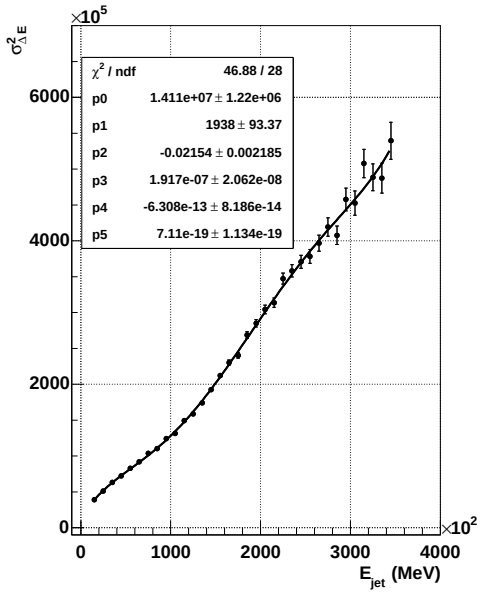

Figure 6.11: The variance of ΔE as a function of the jet energy for light jets

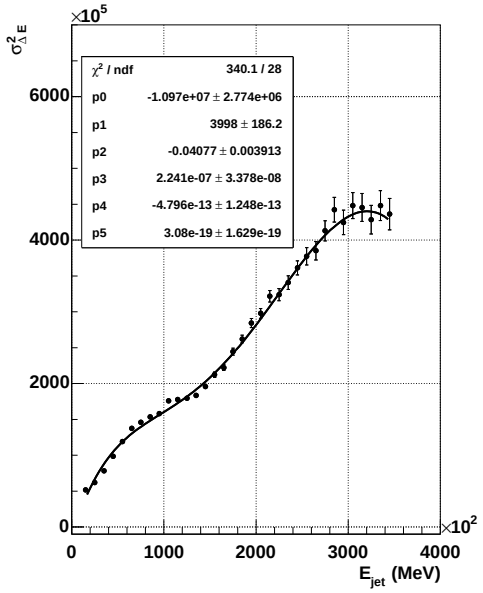

Figure 6.12: The variance of ΔE as a function of the jet energy for b-jets

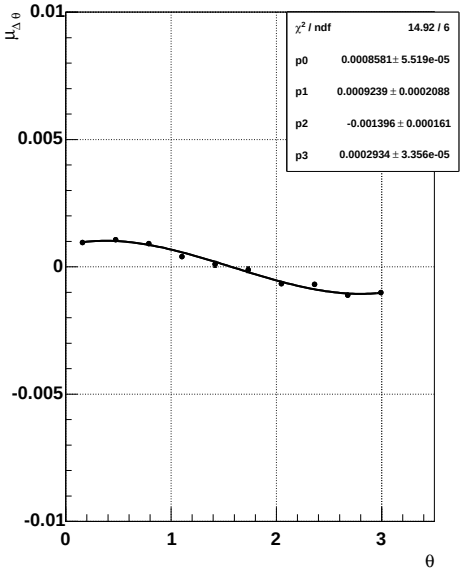

Figure 6.13: The mean value of $\Delta\theta$ as a function of the jet θ for light jets

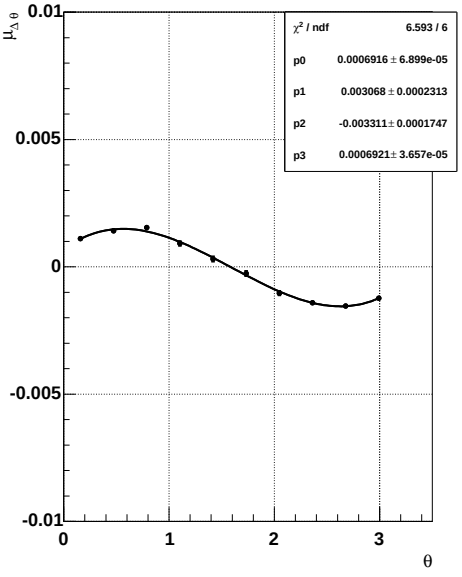

Figure 6.14: The mean value of $\Delta\theta$ as a function of the jet θ for b-jets

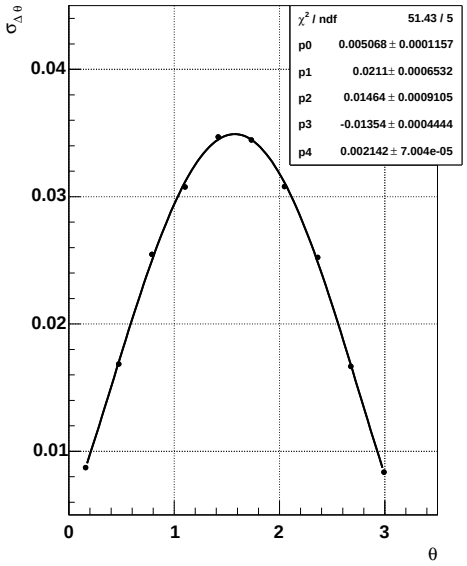

Figure 6.15: The standard variation of $\Delta\theta$ as a function of θ for light jets

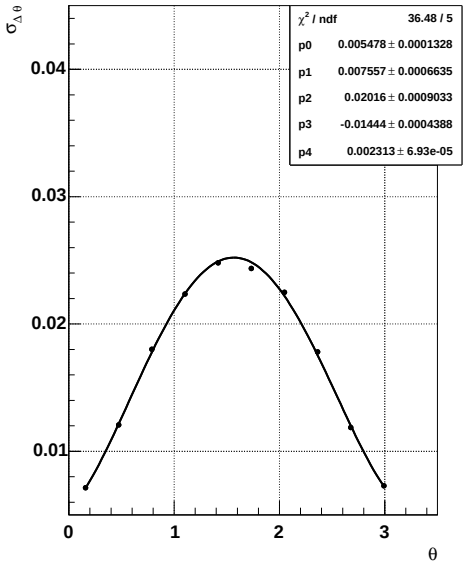

Figure 6.16: The standard variation of $\Delta\theta$ as a function of θ for b-jets

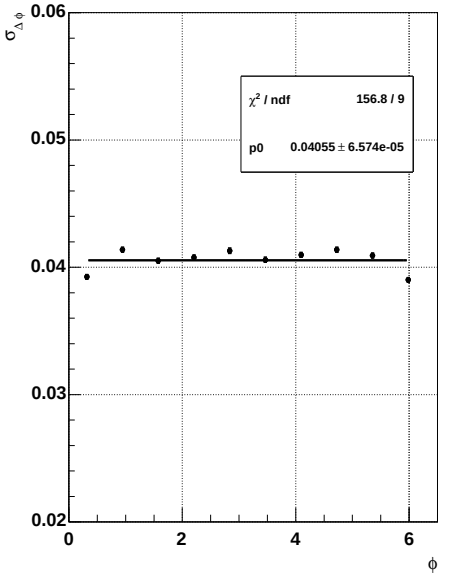

Figure 6.17: The standard variation of $\Delta\phi$ as a function of ϕ for light jets

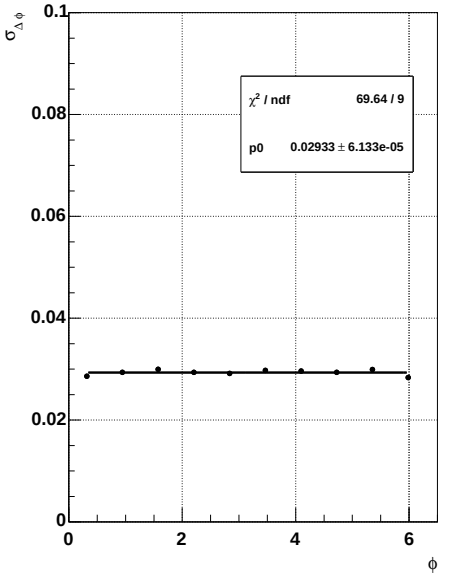

Figure 6.18: The standard variation of $\Delta\phi$ as a function of ϕ for b-jets

The scatter of ΔE, $\Delta\theta$ and $\Delta\phi$ as well as their deviation from zero may depend on the value of the corresponding jet property E, θ or ϕ, respectively. Especially for the energy and for the polar angle θ a strong dependence on the property value is expected. In order to obtain Gaussian errors for ΔE, $\Delta\theta$ and $\Delta\phi$ as functions of the values of the corresponding jet property, the distributions of the deviations are studied separately for different ranges in E, ϕ and θ. The ΔE distribution is analysed for each of 34 intervals of 10 GeV in jet energy between 10 GeV and 350 GeV, the distribution for $\Delta\theta$ is taken for each of ten intervals in θ between 0 and π, analogously the distribution for $\Delta\phi$ is taken for each of ten intervals in ϕ between 0 and 2π. These distributions are then fitted with gauss-functions. The obtained Gaussian parameters $\mu_{\Delta E}$ and $\sigma^2_{\Delta E}$ for the mean and the scatter of ΔE obtained from the fits to the ΔE distributions are shown in FIG. 6.9 and FIG. 6.11 for light jets and in FIG. 6.10 and FIG. 6.12 for b-jets as a function of the jet energy.

It can be seen that the $\mu_{\Delta E}$ has larger absolute values for b- than for light quarks, indicating a larger difference between the energy of the quark and the jet. Furthermore $\mu_{\Delta E}$ for the b-jets is behaving like a constant for large energies, while for light jets $\mu_{\Delta E}$ decreases to larger negative numbers for large energies. To obtain continuous parametrisations for $\mu_{\Delta E}$ for later corrections, the obtained values for $\mu_{\Delta E}$ for light and b-jets are fitted each with a polynomial of order four in E. The fitted functions are indicated by the solid lines in FIG. 6.9 and FIG. 6.10. The description of the $\mu_{\Delta E}$-values is reasonable. The corrections are assumed to be constant for energies larger than 350 GeV.

The width of the fitted distributions $\sigma_{\Delta E}$ represents the uncertainty of the quark energy when it is estimated by measuring the energy of the corresponding jet. The parametrisation

$$\frac{\sigma_{\Delta E}}{E} = \frac{a}{\sqrt{E}} \oplus b \oplus \frac{c}{E} \tag{6.4}$$

is commonly used to describe the energy resolution of calorimeters. The symbol $\oplus$ represents an addition in quadrature. The first term on the right-hand side of EQ. 6.4 is called the sampling term. As sampling is a statistical process, with the measured energy being proportional to the number of samples, the energy resolution is therefore proportional to $\sqrt{\text{no. of samples}}$. This term decreases in importance with increasing energy due to the factor $\sqrt{E}$ in the denominator. The second term in EQ. 6.4 is known as the constant term, as it is independent of energy. This term can become the dominant source of errors at high energies due to the fact that the other two terms in EQ. 6.4 shrink when the energy is increased. The third resolution term describes the electronic noise effects and usually becomes important at low energies.

As the calorimeter resolution is the main contribution to the width of the resolution variable shown in FIG. 6.3 and FIG. 6.4, it is used to find a parametrisation that describes the energy dependence of $\sigma_{\Delta E}$ and which can be later used to obtain Gaussian errors as an input for the KINFIT procedure. Solving EQ. 6.4 for $\sigma^2_{\Delta E}$ gives a polynomial of the order two in E. Therefore, the variance $\sigma^2_{\Delta E}$ is plotted as function of the jet energy for light- and b-jets in FIG. 6.11 and FIG. 6.12, respectively. It turns out that a polynomial of order two in E is not sufficient to describe the energy dependence of $\sigma^2_{\Delta E}$. Instead, a polynomial of order five in E is fitted to the points shown in FIG. 6.11 and FIG. 6.12.

Again, the description of the obtained $\sigma^2_{\Delta E}$-values by the fit indicated by the solid lines in FIG. 6.11 and FIG. 6.12 is reasonable. Like the mean values $\mu_{\Delta E}$ also the values of $\sigma^2_{\Delta E}$ are considered constant for $E > 350\text{GeV}$.

The same procedure is also applied to the $\mu_{\Delta\theta}$ and $\sigma_{\Delta\theta}$ values shown in FIG. 6.13, 6.14, 6.15 and 6.16. The difference $\Delta\theta$ is positive for small θ, going through zero around $\theta = \pi/2$ and negative for angles close to π indicating that the quarks directions on average are closer to the beam direction than the direction of the reconstructed jets. This can be understood e.g. through particles which belong to a jet but are too close to a beam-pipe to be reconstructed by the detector. This loss of particles preferably close to the beam pipe increases the angle between the reconstructed jets and the beam-pipe. However, the systematic shifts are very small, typically in the order of 1/1000 radian. $\sigma_{\Delta\theta}$ shown in FIG. 6.15 and FIG. 6.16 is symmetric around $\theta = \pi/2$ as it is expected. To fit the data, polynomials of order three for the $\mu_{\Delta\theta}$-values and of order four for the $\sigma_{\Delta\theta}$-values are used. The fits describe the obtained values reasonable and are used as continuous parametrisations for the correction of the θ-angle of a jet and the error on θ used as input to the KINFIT procedure.

Due to rotational symmetry in the ϕ-direction no systematic shift of the ϕ-direction of the quark with respect to the direction of the jet is expected. Indeed, the values obtained for $\mu_{\Delta\phi}$ are all compatible with zero, so no correction on ϕ is applied. The values for the statistical spread $\sigma_{\Delta\phi}$ of the jet direction in ϕ around the direction of the quark are shown in FIG. 6.17 for light- and in FIG. 6.18 for b-quarks. As expected, the $\sigma_{\Delta\phi}$-values are independent of ϕ. A constant is fitted to the $\sigma_{\Delta\phi}$-values for light- and b-jets, giving $\sigma_{\Delta\phi} = (4.055 \pm 0.007) \cdot 10^{-2}$ for light and $\sigma_{\Delta\phi} = (2.934 \pm 0.006) \cdot 10^{-2}$ for b-jets.

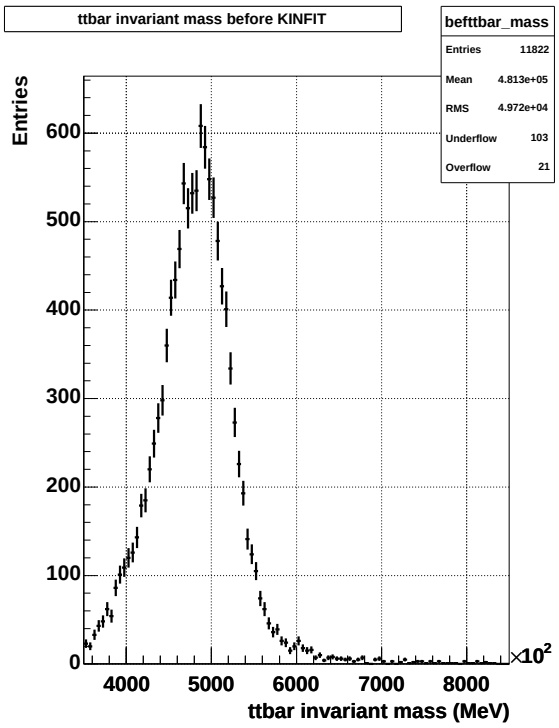

Figure 6.19: The distribution of the invariant mass of the six jets from the reaction $H/A \to t\bar{t} \to$jets when calculated directly

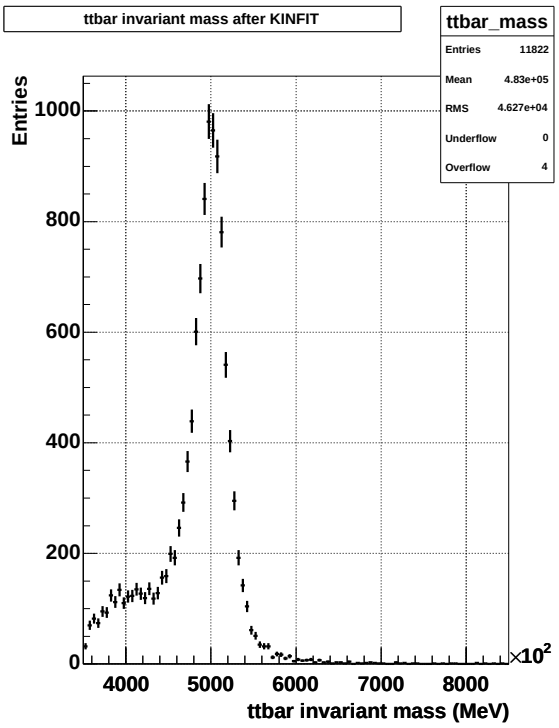

Figure 6.20: The distribution of the invariant mass of the six jets from the reaction $H/A \to t\bar{t} \to$jets obtained from the kinematic fit procedure

6.2.2 Reconstruction of the $t\bar{t}$ invariant mass

The KINFIT procedure is applied in order to improve the resolution of the reconstructed Higgs mass. With the Gaussian errors of the jet properties obtained in Sect. 6.2.1, all input needed for the KINFIT procedure is given. In this section the effect of KINFIT on the resolution of the reconstructed Higgs mass is discussed. For this a sample of simulated Higgs decays into a $t\bar{t}$-pair with an assumed Higgs mass of $m_H = 500$ GeV is used. The sample consists of 40,000 events.

In Fig. 6.19 the distribution of the invariant mass of the six jets of the decay products of the $t\bar{t}$-pair is shown. The six jets have been identified using the assignment method described in Sect. 6.2.1 and the corrections to the jet energy and the polar angle θ have been applied. The jet identification failed in about 2/3 of the events reducing the sample to $\sim 13,000$ events. A broad peak with

a width of $\sigma \simeq 50$ GeV around $\mu \simeq 480$ GeV is reconstructed. Using the KINFIT algorithm to calculate the invariant mass of the $t\bar{t}$-pair, the result shown in FIG. 6.20 is obtained. All possible permutations of the six jets are used as input for the algorithm and the invariant mass calculated from the permutation with the minimal χ^2 from the constrains on m_t and m_W is used. The kinematic fit performed by KINFIT failed to converge in $\sim 10\%$ of the events. Compared to the result shown in FIG. 6.19, the width of the peak is substantially reduced to ~ 20 GeV while the peak position is moved to the expected position at 500 GeV. However, a shoulder to the peak towards smaller invariant masses still remains, due to the misassignment of jets to the initial quarks and the very large discrepancy between the energy of the quarks and assigned jets.

6.3 Separation of $t\bar{t}$ events from QCD multijet background

The final aim of this analysis is the reconstruction of the invariant mass of H^0/A^0 in the full hadronic decay mode via a $t\bar{t}$-pair and to study the prospects of analyses of this decay mode in terms of sensitivity and significance. In a first step, the separation of the huge background of QCD multi-jet events which do not contain top-quarks from events which contain top-quarks is investigated.

Several variables distinguish between $t\bar{t}$-events and QCD multi-jet events, but in general these variables are strongly but not fully correlated. In this analysis a neural network is used to combine these variables into a single discriminatory variable. In this way the complex correlations between these variables are properly considered. In SECT. 6.3.1 the input variables and their discriminating power are described. The training and the structure of the neural network are then presented in SECT. 6.3.2, before in SECT. 6.3.3 the performance of the neural network decision and its impact on QCD produced $t\bar{t}$-events are discussed. The impact of the cut in the neural network output on QCD light jet events and Higgs events are studied in SECT. 6.3.4 and SECT. 6.3.5. Finally in SECT. 6.3.6 the results obtained with several neural networks trained over mutual disjunct mass ranges are discussed.

6.3.1 Discriminating Variables

The bulk of QCD light-jet events does not feature some of the most prominent properties of events with a $t\bar{t}$-pair. The high mass of the top-quarks leads espe-

cially to a number of jets with high transverse momenta, while in light-jet events small transverse momenta dominate. However, a large amount of events with predominantly small p_T-jets would already be suppressed by the ATLAS trigger system (see SECT. 3.3). In order to separate the remaining QCD light-jet events from the $t\bar{t}$-events further discriminative variables have to be studied.

One of the most promising methods to verify the presence of a Higgs contribution in a data sample uses a comparison of the distribution of the reconstructed invariant masses with a theoretical prediction of the combined $t\bar{t}$-production via Higgs bosons and QCD processes (see SECT. 6.4). As the prediction to which the reconstructed mass distribution will be compared includes both contributions and their interference, it is desireable, that the selection procedure alters the relative contributions due to the two production processes as little as possible. That is, the efficiency of the selection procedure for QCD produced $t\bar{t}$-events should be as close as possible to the efficiency for $t\bar{t}$-events from Higgs decays. Therefore, discriminating variables have to be found which allow to distinguish $t\bar{t}$ events from QCD light jet events, but which are not or nearly not sensitive to the difference between the two possible production processes of the $t\bar{t}$-pair.

Most of the the discriminating variables are constructed utilising the kinematic differences between $t\bar{t}$-events and light jet events. In $t\bar{t}$-events the large invariant mass of the decaying top quark allows for very high transverse momenta of the decay products, which also have to be balanced due to momentum conservation. This gives $t\bar{t}$-events a rather spheric appearance. In QCD light jet events the multitude of jets originates in successive radiation of hard gluons. Generally, the energy is distributed less equally among the jets than in $t\bar{t}$-events. Moreover, the gluon radiation is subdued to strong interferences which limit this radiation and give light jet events in general a more planar appearance.

The following candidates for discriminative variables have been investigated [52]:

- The **Aplanarity** A is defined as

$$A = \frac{3}{2} Q_1 \tag{6.5}$$

  where Q_1 is the smallest eigenvalue of the normalised momentum tensor

$$T_{ij} = \frac{\sum p_{ia} p_{ja}}{\sum p_a^2} \quad .$$

  On average, events containing a $t\bar{t}$-pair are expected to show a larger aplanarity.

- The **Sphericity** [53] is defined as

$$S = \frac{3}{2}(Q_1 + Q_2) \tag{6.6}$$

where Q_1 and Q_2 are the first two eigenvalues of the normalised momentum tensor defined above. Due to the large top mass and the decay chain of the top quark, events containing a $t\bar{t}$-pair are expected to have on average a larger sphericity than QCD light jet events.

- The **Centrality** C is defined as the ratio of the total transverse energy over the total energy:

$$C = \frac{H_T}{H_E}. \tag{6.7}$$

QCD light jet events are expected to show on average a smaller Centrality than $t\bar{t}$-events.

- The largest transverse energy of a jet in an event divided by the total transverse energy of this event

$$ET1 = \frac{E_T^1}{H_T}. \tag{6.8}$$

Events containing a $t\bar{t}$-pair are expected to have six jets with rather large transverse energy, while in QCD light jet events most of the transverse energy is expected to be concentrated in the first few leading jets. This leads to larger values of $ET1$ in light-jet than in $t\bar{t}$-events.

- The geometric mean of the fifth and sixth largest transverse energy of a jet in an event

$$E_T^{(5,6)} = \sqrt{E_T^{(5)} \cdot E_T^{(6)}}. \tag{6.9}$$

Events with fully hadronically decaying $t\bar{t}$-events have six jets of comparable transverse energy, while in QCD light jet events the transverse energy is concentrated in a few leading jets. Therefore, higher values of $E_T^{5,6}$ are expected in $t\bar{t}$-events than in QCD light jet events.

- The sum of the transverse energies of the six jets from the assumed $t\bar{t}$ decay,

$$H_T = \sum_{i=1}^{6} E_{T,i} \tag{6.10}$$

The transverse energy in $t\bar{t}$ events is on average higher than in QCD light jet events due to the high top mass.

- The sum of the transverse energies of the four sub-leading jets from the assumed $t\bar{t}$ decay

$$HT3j = \sum_{i=3}^{6} E_{T,i} = H_T - E_{T,1} - E_{T,2} \tag{6.11}$$

- The invariant mass of the two b-tagged jets[1]. QCD light jet events produce mainly jets with low invariant masses with respect to each other. In case two of these jets are b-jets are accidently mis-tagged as b-jets, their invariant mass is on average smaller than the invariant mass of the two b-jets in an $t\bar{t}$ event.

- The χ^2-value obtained from the KINFIT procedure is used to discriminate between events containing a $t\bar{t}$-pair and QCD light-jet events. As the mass of the top-quarks as well as the mass of the W-bosons produced in their decay are constraints to the kinematic fit, light jet events in which the reconstruction of a $t\bar{t}$-pair is artificially forced are expected to correlate to higher values for χ^2.

The first three variables A, S and C are calculated both, in the rest frame of the detector as well as in the rest frame of the initial hard interaction, where the latter is usually boosted with respect to the former along the beam-axis. The rest frame of the initial hard interaction is defined as the rest frame of the assumed $t\bar{t}$-pair which is reconstructed in a given event. The boost between those two frames allows for the definition of further discriminating variables:

- The β**-factor** of the boost. Due to the large mass of top-quarks, events containing a $t\bar{t}$-pair are expected to be less boosted than events which contain only light jets.

- The cosine of the angle between the direction of the top-quark[2] and the beam axis in the rest frame of the $t\bar{t}$-pair $\mathbf{cos}\theta^*$. This variable is mainly used to distinguish between events with a QCD produced $t\bar{t}$-pair from events in which the $t\bar{t}$-pair is produced in the decay of a Higgs boson. The Higgs boson is a scalar particle, so no direction in its rest frame is preferred and the distribution of $\cos\theta^*$ is expected to be flat for these events. $t\bar{t}$-pairs

[1] This is the square of the sum of the four-momenta of the two jets. The invariant mass of each single jet is not considered here, they are assumed massless.

[2] As the top and the anti-top are necessarily moving back-to-back in their common rest frame, the variable remains unchanged if the direction of the quark or the anti-quark is used for its definition

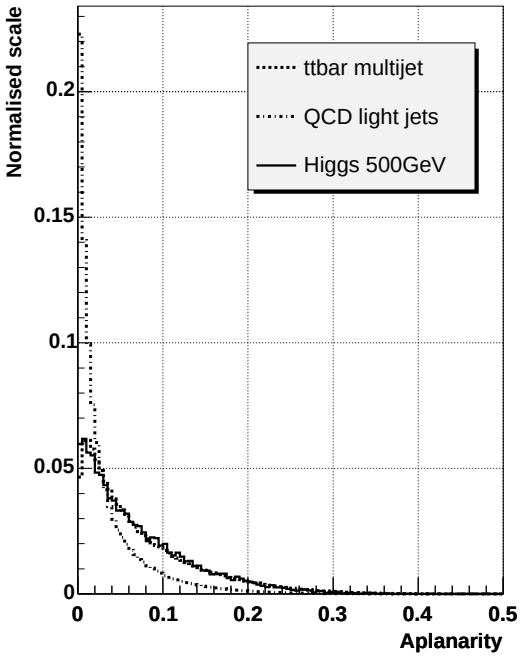

Figure 6.21: Distribution of aplanarity A for the three event samples in the laboratory frame

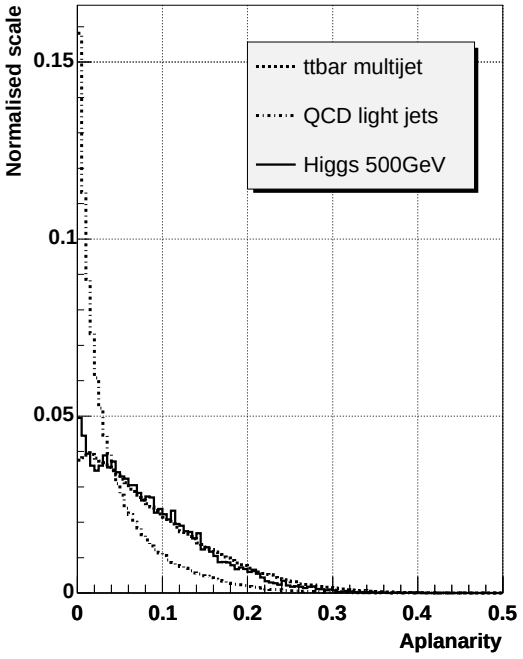

Figure 6.22: Distribution of aplanarity A for the three event samples in the rest frame of the event

from strong interactions are produced via intermediate gluons, which are vector-bosons, so an increased production of these events at large absolute values of $\cos\theta^*$ is expected. However, this variable would also allow to distinguish between $t\bar{t}$-events and QCD light jet events, because the QCD light jet events are more concentrated in the region of large absolute values of $cos\theta^*$ than both types of $t\bar{t}$-events. But as this variable distinguishes between Higgs produced $t\bar{t}$-events and QCD produced $t\bar{t}$-events, the inclusion of $cos\theta^*$ into the neural network input would lead to different selection efficiencies for the two $t\bar{t}$-event types. As discussed in the beginning of this section, this is disfavoured in this analysis.

The power of these variables to discriminate between QCD light-jet and QCD $t\bar{t}$-events has been studied on an event sample, which passed the ATLFAST detector simulation, but was not required to fulfill the trigger conditions. For the selection of jets as input to the kinematic fit, only experimentally accessible information

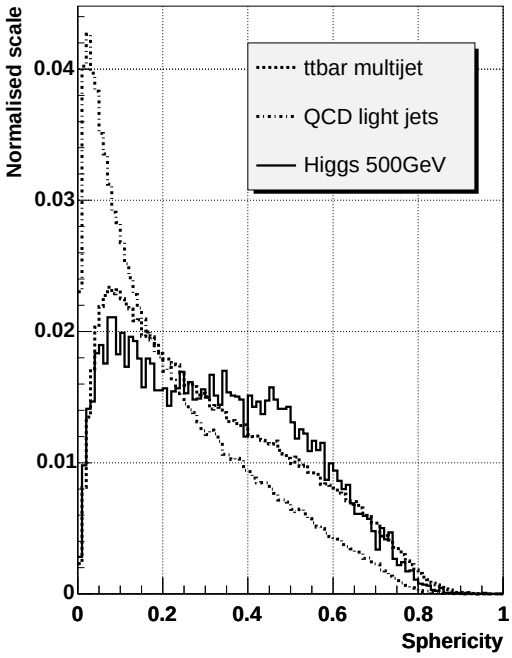

Figure 6.23: Distribution of sphericity S for the three event samples in the laboratory frame

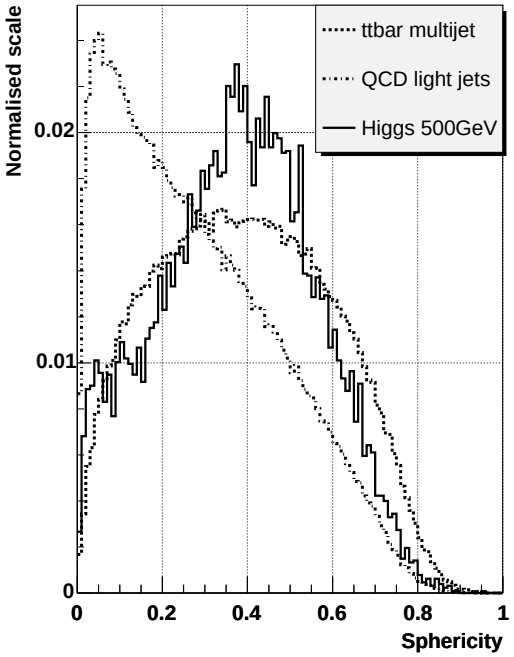

Figure 6.24: Distribution of sphericity S for the three event samples in the rest frame of the event

is used and the jets are selected according to the following criteria:

- The simulated b-tagging procedure described in SECT. 4.3 is used to identify b-jets. The two b-tagged jets with the highest transverse momenta are considered to be the decay products of the $t\bar{t}$-pair. Events with less than two positively b-tagged jets are discarded.
- The four anti-b-tagged jets with the highest transverse momenta are considered to be the decay products of the W-bosons produced in the decay of the $t\bar{t}$-pair.

The studies are done with an assumed Higgs mass of 500 GeV, results for different masses may differ.

In FIG. 6.21 the distribution of the aplanarity A is shown for the signal ($t\bar{t}$) and the background (QCD light jets) events. The distribution of the aplanarity

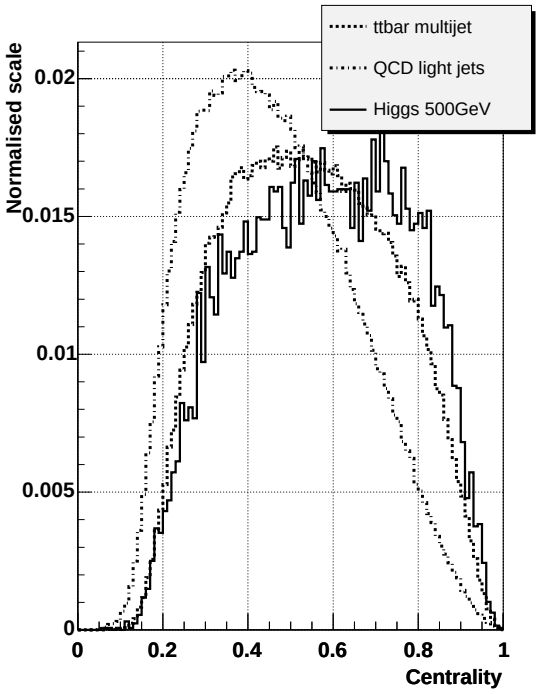

Figure 6.25: Distribution of centrality C for the three event samples in the laboratory frame

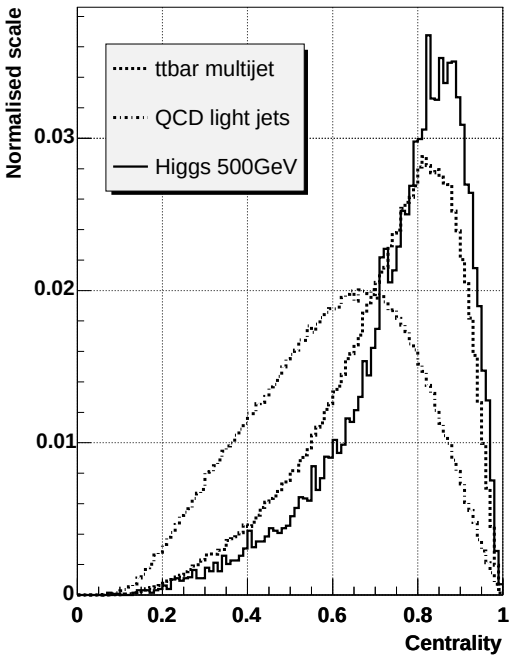

Figure 6.26: Distribution of centrality C for the three event samples in the rest frame of the event

in the rest frame of the event is shown in FIG. 6.22. In both distributions the background events are peaked at small values of A, while the distribution of the signal events is flatter and extends more to high values of A. The aplanarity distributions for Higgs produced $t\bar{t}$ and QCD produced $t\bar{t}$ events are in very good agreement.

In FIG. 6.23 and FIG. 6.24 the distributions for the sphericity S in the rest frame of the experiment and in the rest frame of the event are shown. In the rest frame of the event the distribution of the background events peaks at low values of S and falls nearly linearly with increasing S, while the distribution for the signal events is symmetric around a maximum at $S \sim 0.4$. This variable has a large discrimination power for these two event types. The distributions for both $t\bar{t}$ production processes are very similar, the difference between them is small compared to the difference to the sphericity distribution of the QCD light jet events.

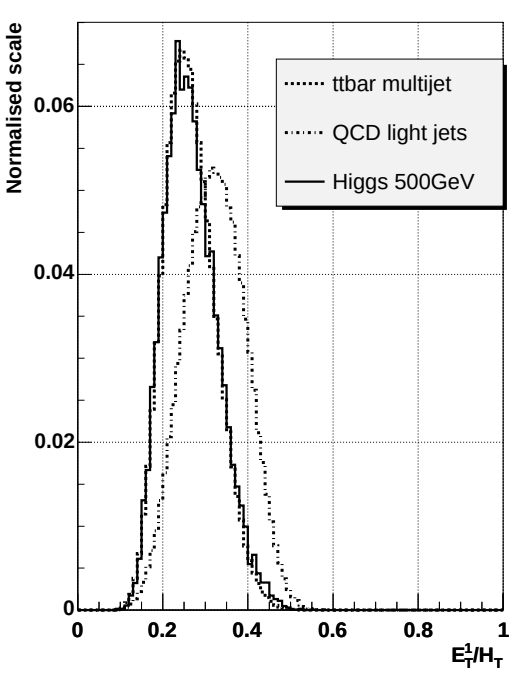

Figure 6.27: Distribution of $ET1$ for the three event samples in the laboratory frame

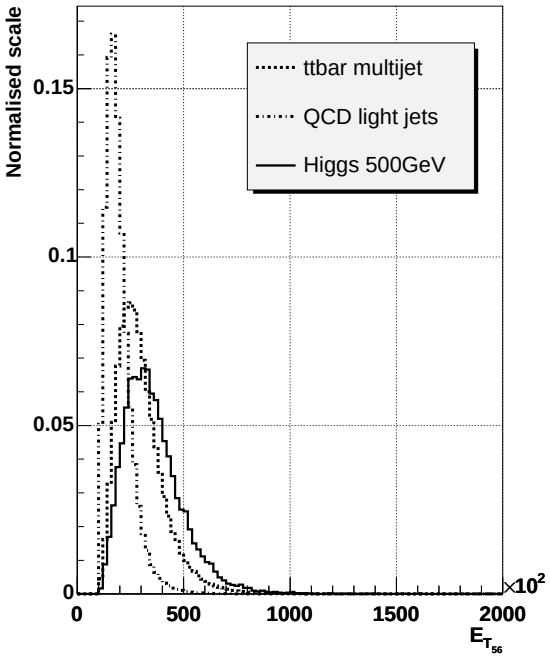

Figure 6.28: Distribution of $E_T^{(5,6)}$ for the three event samples in the laboratory frame. The abscissa shows units of MeV.

The distribution of the centrality C is shown in FIG. 6.25 for the rest frame of the experiment and in FIG. 6.26 for the rest frame of the event for both types of signal and background events. While in the laboratory frame signal and background distributions are similar to the distribution for the background events being slightly shifted to lower values, the difference between signal and background distributions is larger when studied in the rest frame of the event. Here the distribution for the signal events peaks at high values of centrality and decreases rapidly towards lower values of C, while the distribution for the background events shows a broad peak at $C \sim 0.65$. The distributions for both types of signal events are again in good agreement. Also this variable has potential to separate both event types although both distributions are broad and have a substantial overlap.

In FIG. 6.27 the distributions of the energy fraction $ET1$ are shown. The distributions for signal events is shifted towards smaller values of $ET1$ with respect

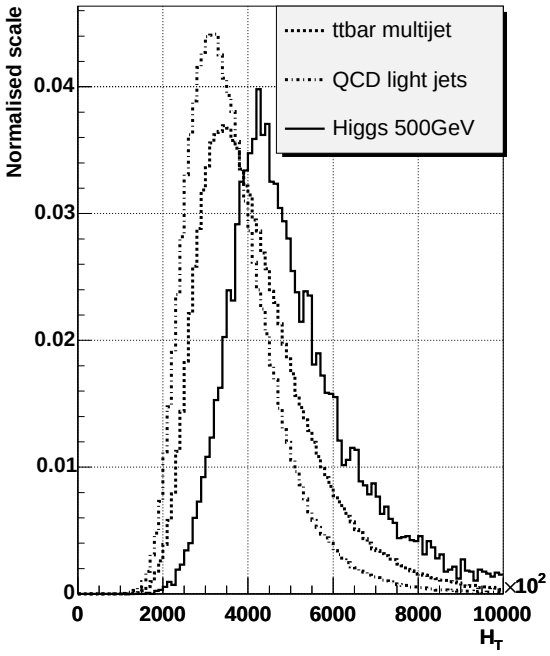

Figure 6.29: Distribution of H_T for the three event samples in the laboratory frame. The abscissa shows units of MeV.

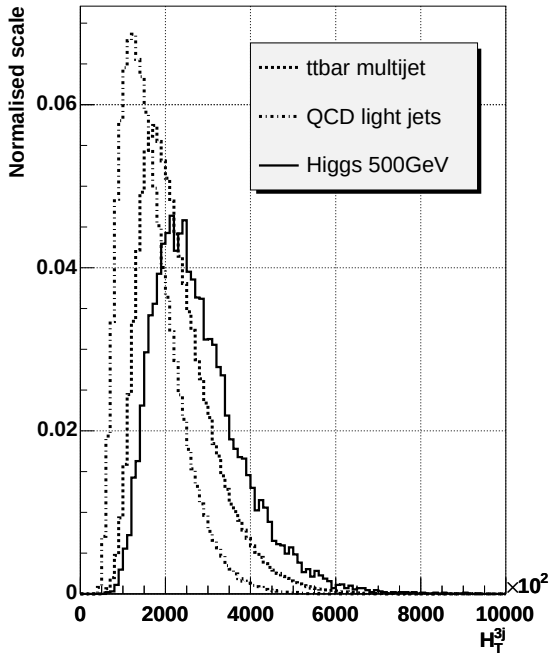

Figure 6.30: Distribution of $HT3j$ for the three event samples in the laboratory frame. The abscissa shows units of MeV.

to the distribution of the background events with a substantial overlap of both distributions. The distributions of both types of signal events cannot be distinguished.

In FIG. 6.28 the distributions for the energy mean $E_T^{(5,6)}$ are shown. Here the background distribution peaks at low values of $E_T^{(5,6)}$ while the signal distribution is broader and shifted towards higher values of $E_T^{(5,6)}$. The distributions for both types of signal events differ slightly, but the difference is still small compared to the difference between the signal and the background distributions. QCD produced $t\bar{t}$ events have on average smaller invariant $t\bar{t}$ masses than Higgs produced $t\bar{t}$ events. This leads to the small shift of $E_T^{(5,6)}$ to lower values for the QCD produced $t\bar{t}$ events compared to the Higgs produced $t\bar{t}$ events. Although for both energy-related variables the distributions for signal and background events overlap, these variables show some discrimination power which can be used.

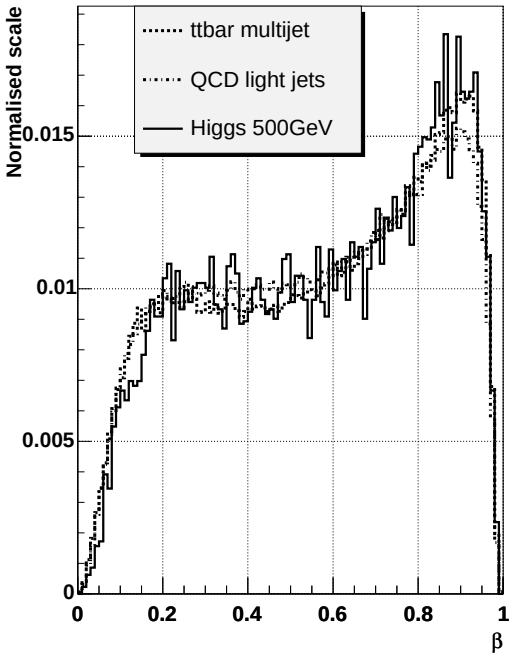

Figure 6.31: Distribution of β for the three event samples with respect to the laboratory frame

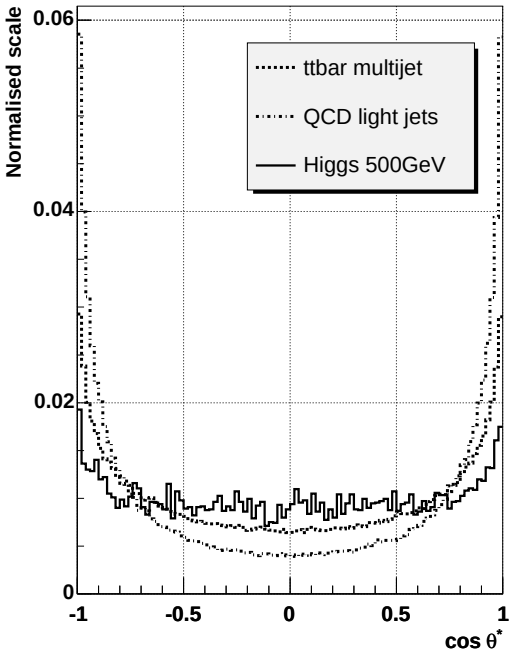

Figure 6.32: Distribution of $\cos\theta^*$ in the $t\bar{t}$-rest frame for the three event samples

FIG. 6.29 shows the distributions of the variable H_T as defined in EQ. 6.10. The distributions for all three data samples show a peak with a tail to higher values of H_T. The distribution for QCD light jet events and QCD produced $t\bar{t}$ events overlap largely, while the distribution for Higgs produced $t\bar{t}$ events peaks at higher values of H_T due to the high Higgs mass in the simulated data sample. Because of the large overlap between the QCD light jet and the QCD produced $t\bar{t}$ sample, which does not allow for a good separation between this two channels, and especially because of the large differences between the two $t\bar{t}$ channels, this variable is not used as an input to the neural net.

In FIG. 6.30 the variable $HT3j$ as defined in EQ. 6.11 is shown. The situation here is similar to the situation for H_T discussed above, therefore also this variable does not enter the neural net to separate QCD light jet events from $t\bar{t}$ events.

The distributions of the β-values for signal and background events are shown in FIG. 6.31. Both distributions are very similar in shape, so this variable does not

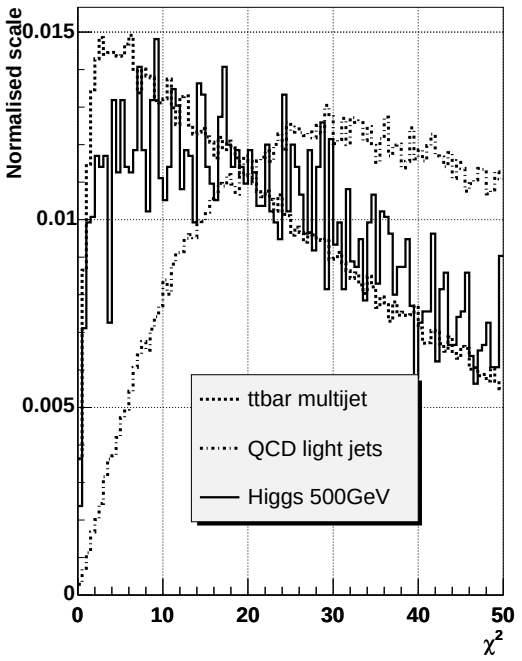

Figure 6.33: The distribution of the minimum χ^2 value from the kinematic fit for the three event samples

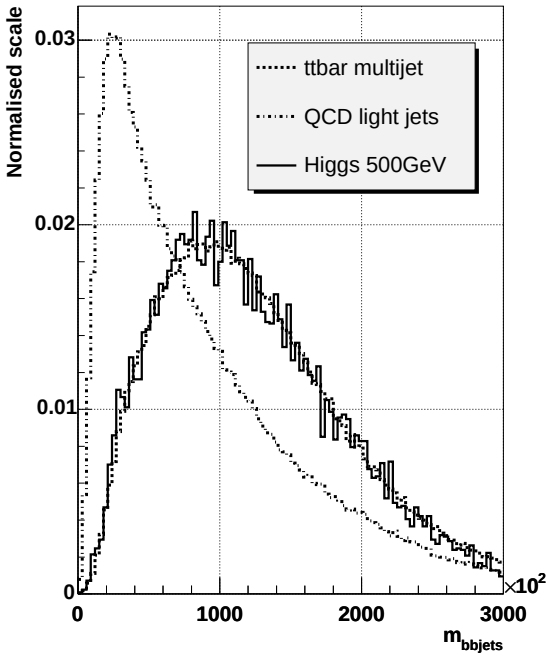

Figure 6.34: The distribution of the invariant mass of the two b-tagged jets for the three event samples. The abscissa shows units of MeV.

exhibit a large discrimination power for these two event types.

The variable $\cos\theta^*$, shown in FIG. 6.32 has been introduced to distinguish between events with an intermediate Higgs boson and those without, so this variable is not expected to discriminate between QCD light jet event and QCD produced $t\bar{t}$ events, where in both event types the intermediate particle is a vector-boson. As expected, both these distributions shown in FIG. 6.32 show a similar behaviour: They peak at large absolute values of $\cos\theta^*$ and are low around zero. The distributions for Higgs produced $t\bar{t}$ is as expected nearly constant.

One of the most promising variables, provided by the KINFIT procedure, is the minimal χ^2-value of an event, reflecting the quality of the reconstruction of the W- and top-masses in the event. This variable is not to be used in studies of the top-mass itself, as it enters as a parameter here, but it can be utilised to select top-events for other studies as e.g. the search for resonances decaying into $t\bar{t}$-pairs.

The distributions of χ^2 for signal and background events are shown in FIG. 6.33. Events from the signal sample show, as expected, rather low values of χ^2 and the distribution drops for increasing χ^2, while in background events predominantly large values for χ^2 are found. This variable has a large discrimination power for this two event types.

In FIG. 6.34 the distribution of the invariant mass calculated from the sum of the momenta of the two b-tagged jets is shown for the three event samples. As expected, the distribution for the QCD light jet event sample in which the b-tagged jets are light jets which have been mis-tagged, peaks at low invariant masses, while the invariant mass of the b-tagged jets for the two event samples in which the b-tagged jets most likely are true b-jets from top decays, is generally much higher. Furthermore, the distribution is the same for both samples, the QCD produced top events and the events with top quarks from Higgs decays.

6.3.2 Training of the Neural Network

In order to perform cuts on the discriminating variables, a neural network is used to combine these variables into one meaningful cut variable. The neural network here is a feed forward neural network provided in the RootJetNet package. It consists of 10 input nodes and 20 hidden layers and one output node. As input quantities the variables A (EQ. 6.5), C (EQ. 6.7), S (EQ. 6.6), $ET1$ (EQ. 6.8), $E_T^{(5,6)}$ (EQ. 6.9), the minimum χ^2 value of the kinematic fit procedure and the invariant mass of the two b-tagged jets are used. A, C and S are evaluated in the laboratory frame as well as in the rest frame of the assumed $t\bar{t}$ pair.

The shape of the distributions of the discriminating input variables may, and in many cases do, depend on the invariant $t\bar{t}$ mass. As the aim of this procedure is to obtain the distribution of the reconstructed $t\bar{t}$ mass, this quantity is not allowed to enter the neural network directly nor indirectly.

In an attempt to achieve nevertheless an optimised selection procedure which takes the change of the distributions' shape with the invariant $t\bar{t}$-mass into account, it has been suggested for the scope of this analysis to train several independent neural networks, each of which only being trained with and applied to events with an invariant $t\bar{t}$-mass within a given range of mass values [55]. The mass ranges of the different neural networks are mutually exclusive. Due to the specialisation of the neural networks on only a limited mass range, the change of the distributions' shape due to their mass dependence is also limited. This would allow for a better discrimination power of the output variable of the specialised

neural networks compared to a neural network trained for the whole range of studied invariant masses.

To this end, four neural networks are trained, each of these neural networks receiving only events where the reconstructed $t\bar{t}$ mass is within a certain interval. The four intervals in $m_{t\bar{t}}$ used are

$$\begin{aligned} 350\text{GeV} &\leq m_{t\bar{t}} < 450\text{GeV}, \\ 450\text{GeV} &\leq m_{t\bar{t}} < 550\text{GeV}, \\ 550\text{GeV} &\leq m_{t\bar{t}} < 650\text{GeV and} \\ 650\text{GeV} &\leq m_{t\bar{t}} \quad . \end{aligned}$$

In parallel, a single neural network is trained with all events, indiscriminate against the reconstructed $t\bar{t}$ mass.

In order to train the neural networks, additional event samples had to be simulated. The events of these samples had to be processed with the fast simulation of the ATLAS detector and they had to pass the b-tagging procedure and the kinematic fit as described in Sect. 6.1 and Sect. 6.2. This reduces the number of events available for training substantially. In order to have still enough accepted events to even train the neural network corresponding to the highest range in invariant reconstructed mass where the event rate is very low, 1,000,000 $t\bar{t}$ events and around 12,000,000 QCD light jet events have been produced. This ensured at least 10,000 events of each of the two samples in every mass range. The b-tagging and the kinematic fit procedure fail significantly more often in QCD light jet events, which makes the larger amount of produced light jet events necessary.

For the training of the single neural network, 55,000 QCD produced $t\bar{t}$ events and 55,000 QCD light jet events are taken from these samples. For each of the two event types, 30,000 events are used to train the neural network, while the remaining 25,000 events are given to the neural network for testing.

The neural net is supposed to distinguish only between light jet events and events which contain a decaying $t\bar{t}$-pair, it is not supposed to distinguish between the different production processes of the $t\bar{t}$-pair. Therefore, no Higgs decays into $t\bar{t}$-pairs need to be simulated for the training of the neural network. However, the assumption that the neural network does not distinguish between QCD produced $t\bar{t}$-events and Higgs decays into $t\bar{t}$-pairs will be verified later.

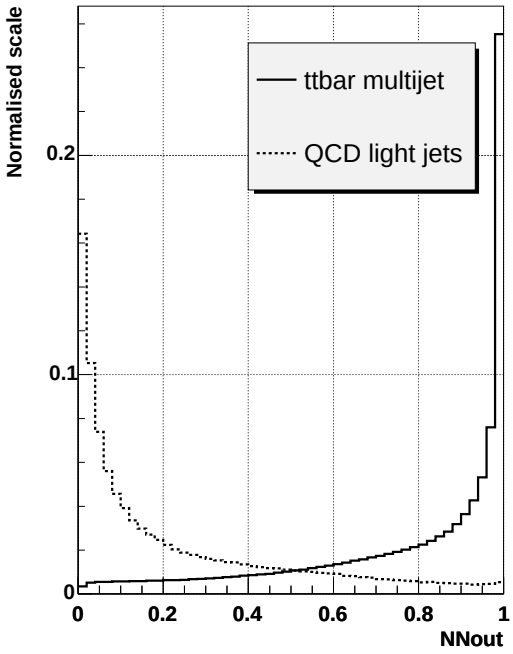

Figure 6.35: The output variable NN_{out} of the neural network for one neural network trained over all the mass-range

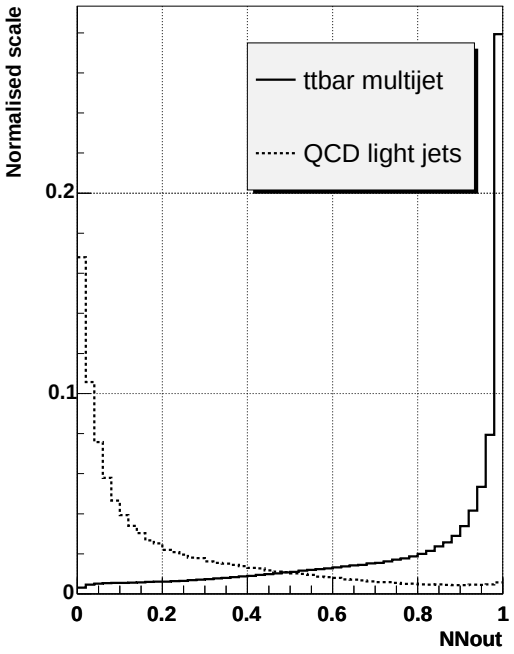

Figure 6.36: The output variable NN_{out} of the neural network for four neural networks trained over different mass-ranges

6.3.3 Efficiency and Purity of the Selection Procedure

In FIG. 6.35 and FIG. 6.36 the distribution of the output variables of the neural networks trained as described in SECT. 6.3.2 are shown. These distributions are obtained using the simulated data samples of QCD light jet events and QCD produced $t\bar{t}$ events. The sample of background (light jet) events is much larger for a given luminosity than the sample of signal ($t\bar{t}$) events. In order to make a meaningful comparison, the distributions of NN_{out} are all normalised to unity. FIG. 6.35 shows the distribution for one neural network which is trained over all the studied mass range, while in FIG. 6.36 the cumulative distribution for the four neural networks which were trained and applied only on limited mass ranges are shown. In both figures the background distribution peaks around zero and drops very fast for higher values of the output variable while the signal distribution in both figures peaks around one and drops very fast for lower values of the output

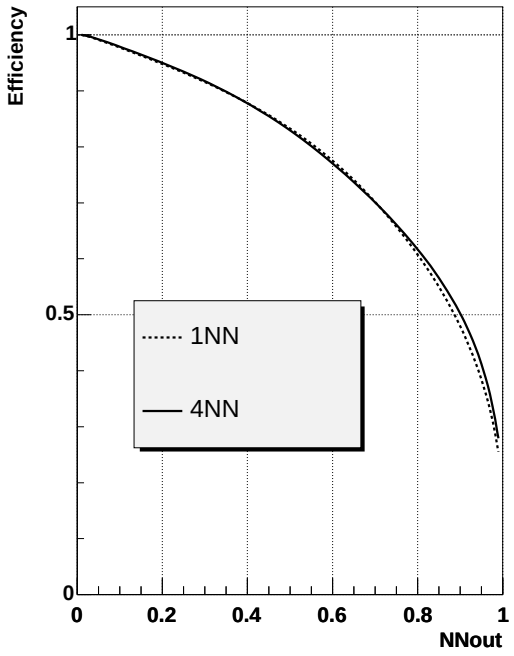

Figure 6.37: The efficiency of one neural network trained over the whole mass-range in comparison to the efficiency of four neural networks trained over mutual exclusive parts of the mass-range as a function of the cut in NN_{out}

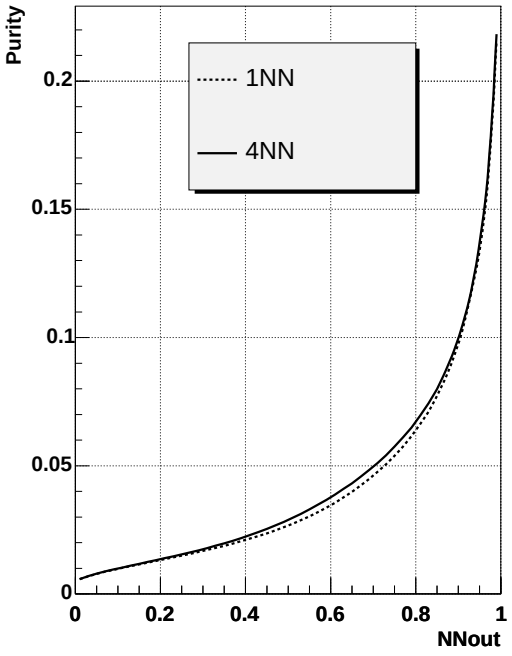

Figure 6.38: The purity of one neural network trained over the whole mass-range in comparison to the purity of four neural networks trained over mutual exclusive parts of the mass-range as a function of the cut in the network output NN_{out}

variable.

From this distributions the efficiency ϵ and the purity p can be calculated for each assumed cut on the output variable. The efficiency is defined as

$$\epsilon = \frac{N_{\text{sig}}^{\text{sel}}}{N_{\text{sig}}^{\text{rec}}} \tag{6.12}$$

and the purity as

$$p = \frac{N_{\text{sig}}^{\text{sel}}}{N_{\text{sig}}^{\text{sel}} + N_{\text{bkg}}^{\text{sel}}} = \frac{N_{\text{sig}}^{\text{sel}}}{N^{\text{sel}}} \tag{6.13}$$

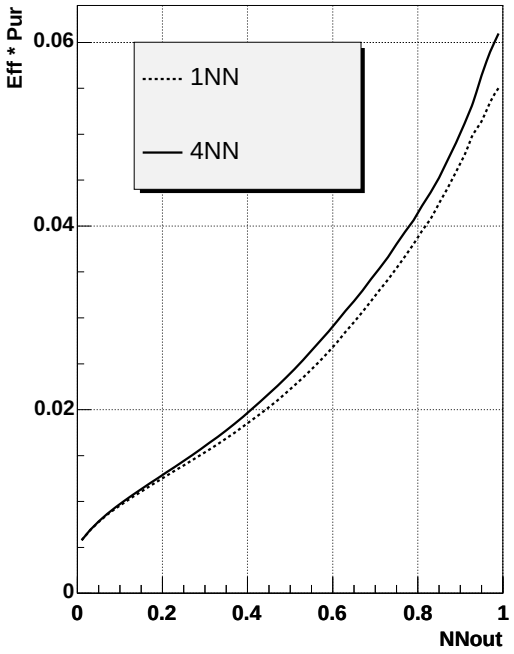

Figure 6.39: The product of efficiency and purity for one neural network trained over the whole mass-range in comparision to the same product four neural networks trained over mutual exclusive parts of the mass-range as a function of the cut in NN_{out}

where N_{sig} and N_{bkg} denote the number of signal ($t\bar{t}$) and the number of background (light jet) events. The number of background events is scaled up with the factor 1242.4 to compensate for the smaller number of generated QCD light jet events as discussed in Sect. 6.1. The index "rec" indicates the number of events of a given type that pass the b-tagging requirements and for which the kinematic fit converged. The index "sel" indicates the number of events of a given type that additionally pass a cut in the output variable of the neural network. The absolute value of the obtained efficiencies and purities reflects therefore the combined effects of selection and reconstruction while the dependence on NN_{out} reflects the effect of the neural network cut only.

The efficiencies for selecting $t\bar{t}$ events as a function of the cut in NN_{out} are shown in Fig. 6.37 for one over-all neural network (dashed line) and for four specialised neural networks (solid line). Accordingly Fig. 6.38 shows the purity while Fig. 6.39 and shows the product of purity and efficiency when using one

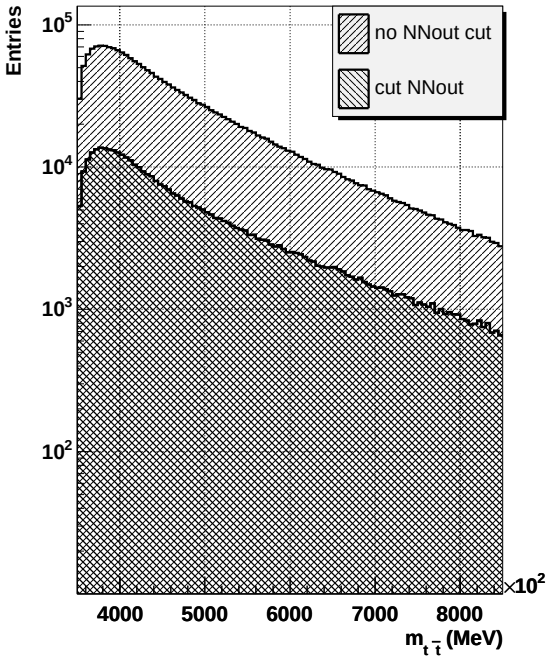

Figure 6.40: The mass distribution for QCD produced $t\bar{t}$ events before and after applying a cut in NN_{out}

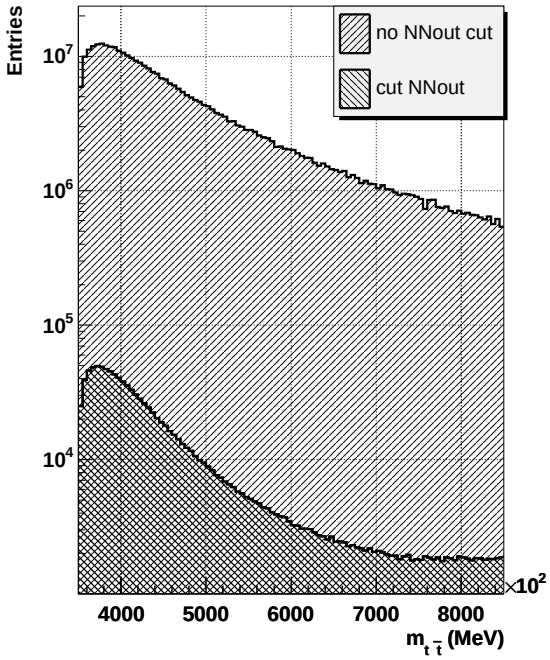

Figure 6.41: The mass distribution for QCD light jet events before and after applying a cut in NN_{out}

or four neural networks, respectively. The purity is large for large cuts in NN_{out}, reaching values of more than 20% for cut values close to 1. The purity even at large cut values remains well below 100%. This is caused by the composition of the simulated data sample which is hugely dominated by QCD light jet events. For smaller cut values the purity drops rapidly, falling below 5% at a cut value around 0.7 and approaching 0.005 for cut values around zero. Both purity curves behave similarly, but the purity obtained with four specialised neural networks for a given cut value is usually slightly higher than the corresponding purity obtained using one neural network for all the mass range.

The efficiencies shown in FIG. 6.37 are also similar. Trivially, both curves start at 100% for no cut or a cut at very small values of NN_{out} applied. For larger cut values in NN_{out} the efficiency declines increasingly fast, reflecting the shape of the distribution of NN_{out} which peaks at 1. Both efficiency curves are similar, but again the use of four specialised neural networks yields slightly better results than the use of one neural network over all the studied mass range.

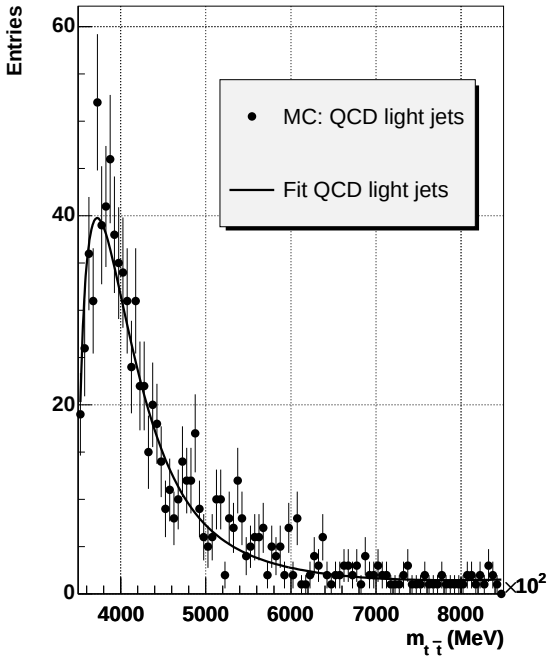

Figure 6.42: The mass distribution for QCD light jet events that pass a cut in NN_{out} of 0.99 and the parametrisation fitted to the distribution

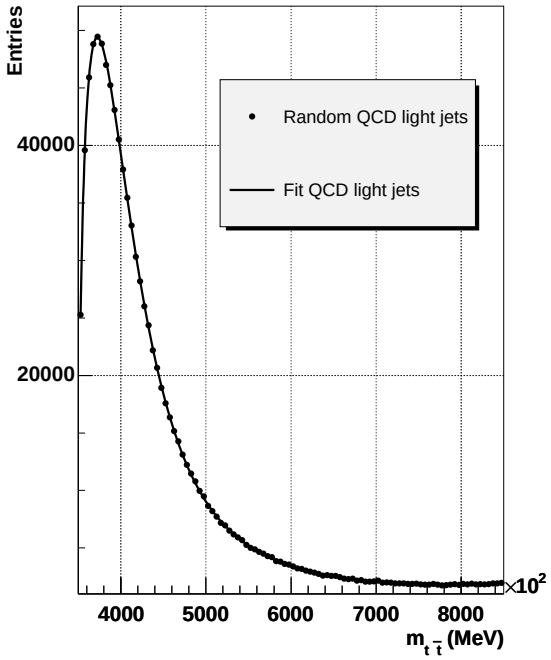

Figure 6.43: The scaled up parametrisation from FIG. 6.42 with the randomly scattered pseudo data distribution

The products of efficiency and purity in FIG. 6.39 show the better performance of four neural networks compared to one over-all neural network in efficiency and purity combined. However, the product of efficiency and purity is monotonously rising with increasing cut values in NN_{out}, indicating that a cut as hard as reasonably possible should be applied.

In FIG. 6.40 the mass distribution for QCD produced $t\bar{t}$ events is shown before and after the application of a cut $NN_{\text{out}} > 0.99$. The cut in NN_{out} reduces the number of selected events by a factor of ~ 50, but preserves the shape of the distribution. However, an even larger reduction of the QCD light jet background due to this cut is expected.

	gene-rated	after Kinfit	after cut in NN_{out}	reduction rate
QCD light jet events	$4.97 \cdot 10^{10}$	$3.92 \cdot 10^{8}$	$1.21 \cdot 10^{6}$	$2.43 \cdot 10^{-5}$
QCD $t\bar{t}$ events	$7.93 \cdot 10^{6}$	$2.29 \cdot 10^{6}$	$4.44 \cdot 10^{5}$	$5.60 \cdot 10^{-2}$
Higgs events (500GeV)	40,000	12,759	3,403	$8.51 \cdot 10^{-2}$
Signal to background	$1.60 \cdot 10^{-4}$	$5.87 \cdot 10^{-3}$	$3.67 \cdot 10^{-1}$	

Table 6.2: The number of generated and accepted events. Note that the number of light jet events is scaled up in order to compensate for the smaller amount of actually simulated events.

6.3.4 Impact of the Neural Network cut on the simulated QCD light jet sample

Applying a cut in NN_{out} reduces the number of QCD light jet events substantially. As already discussed in Sect. 6.1, only a fraction of the expected QCD light jet background could be simulated and the number of events has to be scaled up accordingly by three orders of magnitude. This lack of actually simulated QCD light jet events leads to a very small number of these simulated events which pass the cut in NN_{out} which is 973 events. The statistical errors of the distribution are therefore very large and the large scatter of the scaled up distribution does not allow for a reasonable comparison with the mass distributions of the $t\bar{t}$ event samples. In order to nevertheless obtain a reasonable estimation of the background distribution, a parametrisation is fitted to the mass distribution of the selected QCD light jet events and this function is scaled up. From this scaled function a pseudo mass distribution is then obtained by adding a random Gaussian scatter to the function values in each bin of the distribution. Assuming Poissonian errors, the variance of the used Gaussian is set equal to the function value in the respective bin.

In Fig. 6.42 the mass distribution for the QCD light jet events which pass the cut $NN_{\text{out}} > 0.99$ is shown. The line indicates the fitted parametrisation

$$f(m) = \sigma_{t\bar{t}}(m) \cdot \left[p_0 + p_1 \cdot m^{-p_2} + p_3 \cdot m^{-p_2 \cdot p_6} + p_4 \cdot e^{-p_5 \cdot m} \right] \tag{6.14}$$

where $\sigma_{t\bar{t}}$ is the predicted mass distribution for QCD produced $t\bar{t}$ events given in Eq. 5.8. The fit gives a χ^2 value of 73.3 with 92 degrees of freedom. The

p_0	$(7.57 \pm 0.04) \cdot 10^{2}$
p_1	$(1.42 \pm 0.06) \cdot 10^{3}$
p_2	$(1.08 \pm 0.05) \cdot 10^{-1}$
p_3	$(-1.695 \pm 0.005) \cdot 10^{3}$
p_4	$(9.5 \pm 5.4) \cdot 10^{4}$
p_5	$(2.6 \pm 0.1) \cdot 10^{-5}$
p_6	$(3.05 \pm 0.04) \cdot 10^{-1}$

Table 6.3: The parameter values for the fitted function Eq. 6.14

obtained parameter values are listed in Tab. 6.3. Fig. 6.43 shows the scaled up parametrisation with the randomly scattered pseudo distribution which will be used for the further studies.

In Fig. 6.41 the distribution of the reconstructed invariant $t\bar{t}$ mass is shown for the QCD light jet events before and after the application of the cut $NN_{\text{out}} > 0.99$. The histogram representing the distribution after the cut is the scattered pseudo distribution described above.

The shape of the distribution is nearly the same for both curves and a reduction of the QCD light jet events by a factor of ~ 200 can be observed.

The exact numbers of simulated events, events which passed the kinematic fit and b-tagging procedure and events which remain after the cut in NN_{out} are given in Tab. 6.2. The numbers given for light jet events are the numbers of the simulated event sample scaled up to the correct luminosity. Therefore, the number of selected QCD light jet events given in Tab. 6.2 does not exactly correspond to the integral of the distribution shown in Fig. 6.41, which is derived from the fitted parametrisation Eq. 6.14.

In Fig. 6.44 the mass distribution for all accepted events after the cut in NN_{out}, i. e. the sum of the lower histograms in Fig. 6.41 and Fig. 6.40, is shown. The mass distribution is despite the hard cut still dominated by the light jet events, which is a general problem of the fully hadronic final state. However, the signal to background ratio has improved from 1:10,000 in the simulated events to 1:3 in the accepted events (see Tab. 6.2). Note, that the simulated events were reduced in number from the beginning due to the cut in the initial hard interaction below which no events have been simulated (see Sect. 6.1).

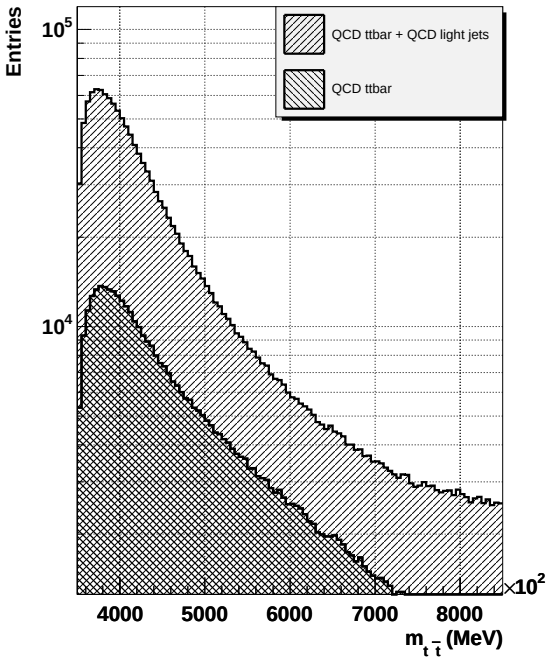

Figure 6.44: The mass distribution of the selected QCD light jet and QCD produced $t\bar{t}$ events. The $t\bar{t}$ contribution to this mass distribution is indicated by the lower histogram.

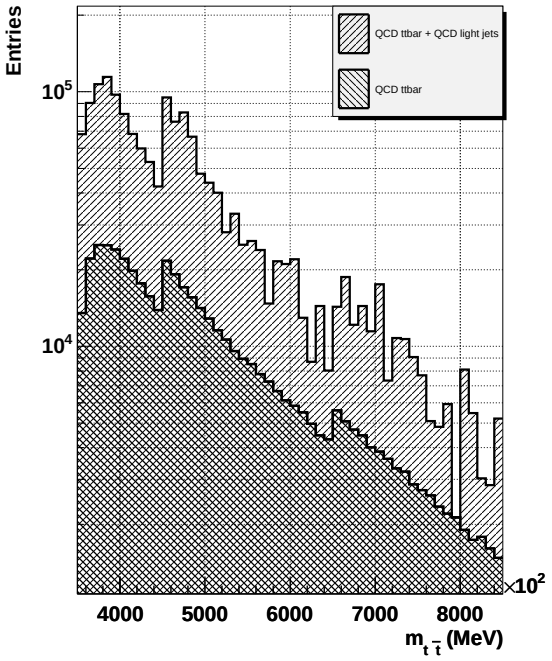

Figure 6.45: The mass distribution of all selected light jet and QCD produced $t\bar{t}$ events obtained with four neural networks, each of which specialised on a certain mass range. The $t\bar{t}$ contribution to this mass distribution is indicated by the lower histogram.

6.3.5 Impact of the neural network cut on the Higgs mass peak

In the previous section the training of the neural network with the aim to separate light jet events from events with $t\bar{t}$ pairs has been described. In order to apply the neural network when searching for a contribution to the $t\bar{t}$ production due to intermediate Higgs bosons, the effect of a cut in the neural network output variable NN_{out} has to be studied.

In FIG. 6.48 the distribution of the output variable NN_{out} is shown for all three simulated data samples: QCD light jet events, QCD produced $t\bar{t}$ events and Higgs

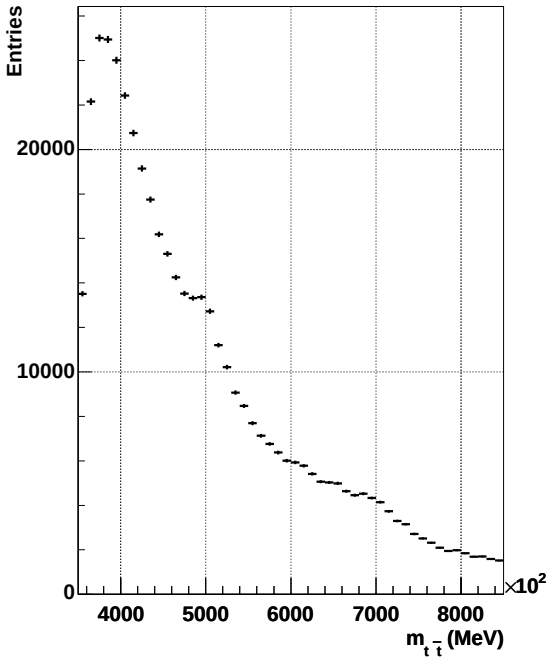

Figure 6.46: The mass distribution for QCD produced $t\bar{t}$ events obtained with four neural networks and a smoothing procedure to average the neural network outputs.

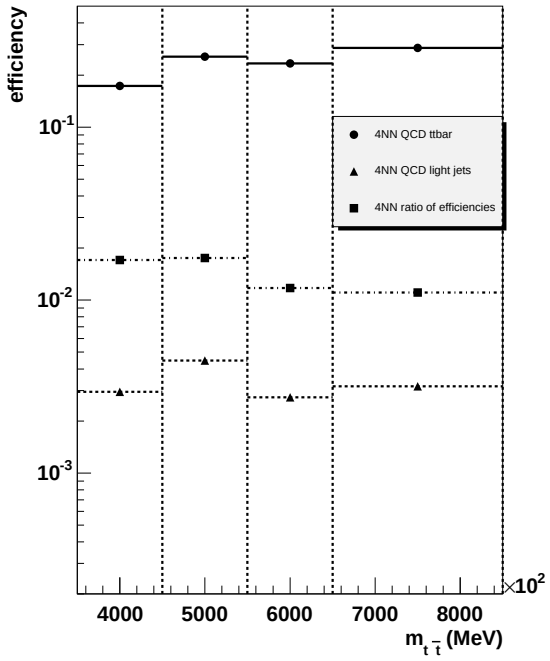

Figure 6.47: The efficiencies of the four neural networks to select QCD light jet events and QCD produced $t\bar{t}$ events as well as the ratio of these efficiencies plotted over the mass ranges, the neural networks are specialised in.

decaying into $t\bar{t}$ pairs. The shape for both samples in which $t\bar{t}$ pairs are produced agree very well, with slightly higher values in NN_{out} for Higgs produced than for QCD produced $t\bar{t}$ pairs. This slightly better separation power for Higgs produced $t\bar{t}$ events is due to the more pronounced event structure in these events, where the $t\bar{t}$ pair always has an energy equivalent to the Higgs mass (here 500GeV).

In order to optimise the cut in NN_{out} for the identification of Higgs contributions to the mass spectrum, the dependence of the *significance*, s, of the Higgs contribution on the cut in NN_{out} is studied. The significance is defined as

$$s = \frac{N_{\text{Higgs}}^{\text{sel}}}{\sqrt{N_{\text{lj}}^{\text{sel}} + N_{t\bar{t}}^{\text{sel}}}} \tag{6.15}$$

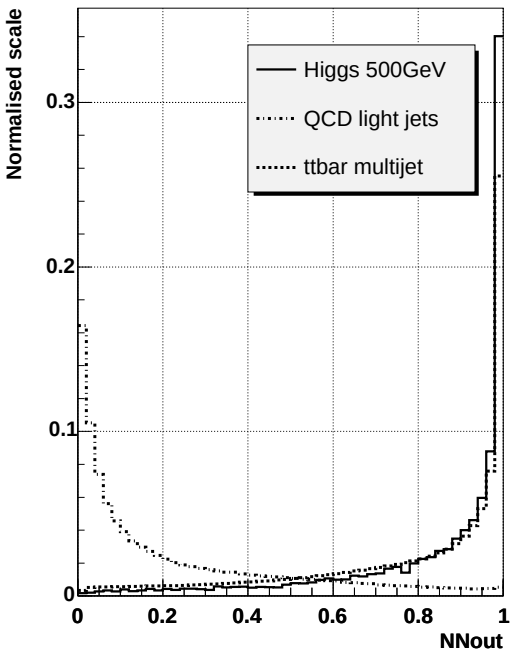

Figure 6.48: The distribution of the neural network output variable NN_{out} for all three event samples

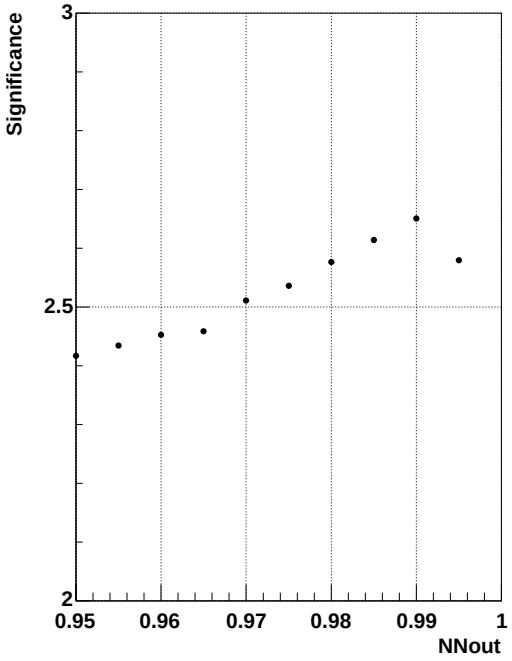

Figure 6.49: The significance of the Higgs contribution to the mass distribution in the interval from 450GeV to 550GeV as a function of the cut in NN_{out}

where $N^{\text{sel}}_{\text{Higgs}}$, $N^{\text{sel}}_{\text{lj}}$ and $N^{\text{sel}}_{t\bar{t}}$ are the number of selected Higgs, QCD light jet and QCD produced $t\bar{t}$ events. The significance represents the contribution to the mass spectrum due to Higgs production in multiples of the expected error of the background contributions. To get a reasonable estimation of s, only events with a reconstructed invariant $t\bar{t}$ mass in the region of the Higgs mass peak, i. e. within the interval [450GeV; 550GeV], are considered. The significance as a function of the cut is shown in FIG. 6.49. For cut values larger than 0.95 the significance is larger than 2.4 and increases with harder cuts due to the increasing fraction of Higgs events in the selected event sample. It reaches a maximum significance of ~ 2.66 at a cut value of 0.99 after which it decreases again. This motivates the use of a cut of $NN_{\text{out}} > 0.99$ which has already been applied in the discussion in the previous section. However, this is an optimistic estimation of the significance with the region of interest placed around the known position of the Higgs mass peak.

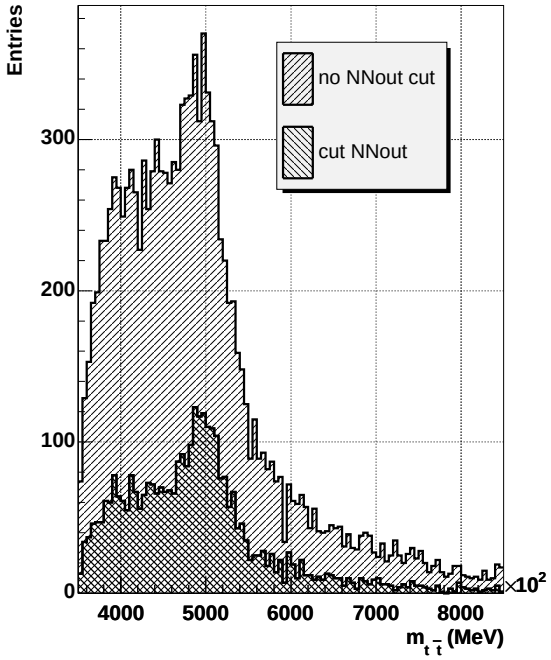

Figure 6.50: The distribution of the reconstructed $t\bar{t}$ mass for the Higgs data sample as obtained from the kinematic fit procedure before and after applying the cut $NN_{\text{out}} > 0.99$

It is to be expected that the significance in an analysis of real data is lower than this estimate. This would disqualify the fully hadronic decay mode as a discovery channel for a heavy MSSM Higgs boson decaying into a $t\bar{t}$ pair. However, given the mass resolution of the reconstruction, the restriction to events within a region of 100 GeV around the Higgs peak is a rather conservative approach and the significance is nevertheless large enough to be optimistic that this decay channel is visible and can contribute to the confirmation of the discovery of a heavy MSSM Higgs boson.

However, in Sect. 6.4 an analysis procedure will be discussed which does not only rely on the additional production of $t\bar{t}$ events due to Higgs decays, but also utilises the distinctive shape of the Higgs mass spectrum.

It is important to understand, if the cut in NN_{out} distorts the shape of the Higgs peak in the invariant mass spectrum. Fig. 6.50 shows the impact of the cut $NN_{\text{out}} > 0.99$ on the mass distribution of the Higgs sample. The upper histogram

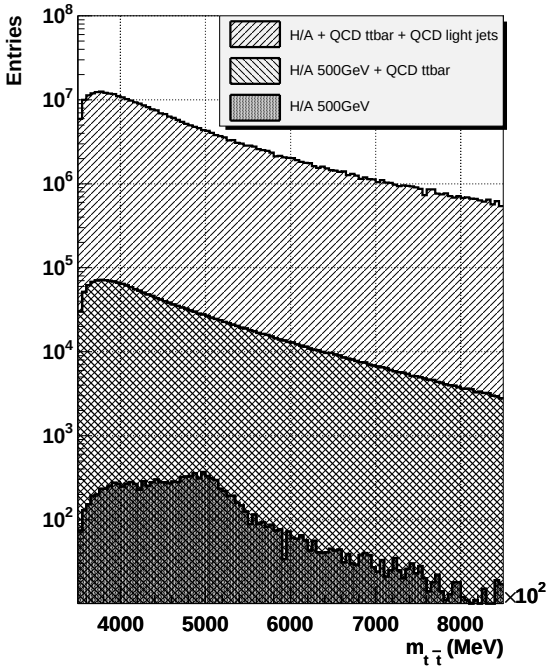

Figure 6.51: The distribution of the reconstructed $t\bar{t}$ mass for the full data sample as obtained with the kinematic fit procedure

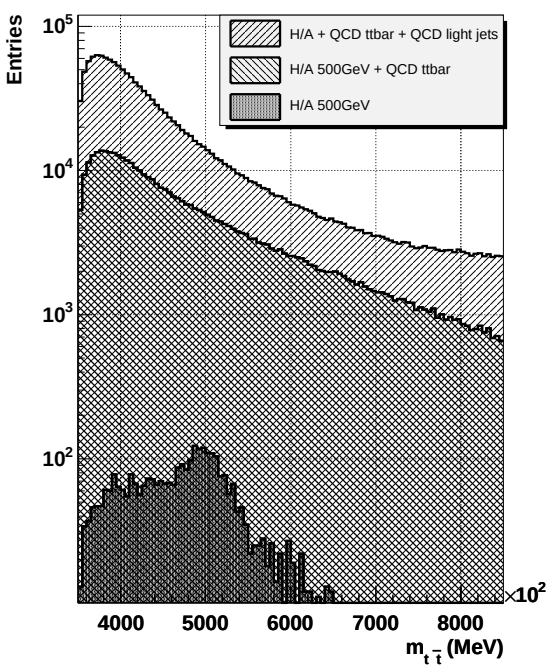

Figure 6.52: The distribution of the reconstructed $t\bar{t}$ mass for the full data sample as obtained with the kinematic fit procedure after applying the cut in $NN_{\text{out}} > 0.99$

shows the distribution of the reconstructed $t\bar{t}$ masses as they are obtained using the kinematic fit. In order to use only experimentally accessible information, not the jets known to come from the decays of the $t\bar{t}$ pair are used as input to the kinematic fit, but the two b-tagged jets and the four un-tagged jets with the highest transverse momentum. These jets are all required to be inside the central region of the detector satisfying $|\eta| < 3.2$. This distinguishes the distribution in FIG. 6.50 from the distribution shown in FIG. 6.20, where only the six jets which are known to be decay products of the $t\bar{t}$ pair are considered. Due to the limited experimentally accessible information the shape of the mass peak in FIG. 6.50 is affected, a shoulder on the left flank of the peak is formed reflecting the fact that a mis-selection of the input jets leads preferably to the reconstruction of lower masses. Nevertheless, the peak is still present and its position is unchanged. The lower histogram in FIG. 6.50 shows the mass distribution for these Higgs

produced $t\bar{t}$ events which pass the cut $NN_{\text{out}} > 0.99$. Comparing the two mass distributions it can be seen that the cut in the neural network output variable does not change the position of the peak and leaves the shape of the peak nearly unchanged. Only the shoulder left of the peak is reduced slightly due to this cut.

The mass distribution for the events of all three data samples can be seen in FIG. 6.51 without and in FIG. 6.52 with the cut $NN_{\text{out}} > 0.99$. The different contributions to the mass distribution are indicated by the shaded areas. Although the ratio between the Higgs contribution and the two other contributions is improved by the cut and the mass peak in the Higgs sample is slightly more pronounced when the cut is applied, the Higgs contribution is not directly recognisable in the sum of the three contributions due to the large difference in event rates and sophisticated methods to identify any contribution due to Higgs decay have to be applied.

6.3.6 Impact of the specialised neural networks on the mass distribution

Alternatively to the use of one neural network trained on the whole studied mass range, the use of several neural networks has been suggested [55]. Each of this networks is only trained on a part of the studied mass-range and its output is only referred to for events with a reconstructed $t\bar{t}$ mass within this range. This procedure is expected to improve the discriminating power of the neural network output by reducing the variation of distributions whose shape depends on the invariant $t\bar{t}$-mass.

In FIG. 6.45 the mass distribution obtained from QCD light jet events and QCD produced $t\bar{t}$ events using the four neural networks which are specialised on certain mass intervals is shown. The $t\bar{t}$ contribution is indicated in the lower histogram. The shape of the $t\bar{t}$ contribution to the mass distribution in FIG. 6.45 is very distorted with steps near the boundaries of the mass intervals of the different neural networks. The step structure is introduced by the different efficiencies the four neural networks have for selecting signal and background events. The efficiencies of the four neural networks to select light jet or QCD produced $t\bar{t}$ events are shown in FIG. 6.47, large differences between the efficiencies can be seen. The same step like behaviour as in the mass distribution for the selected $t\bar{t}$ events also occurs in the mass distribution of the accepted QCD light jet events. This prohibits the fitting procedure to achieve a reasonably smooth scaled up background distribution, which is described above. Therefore, the mass distribution for all accepted events in FIG. 6.45 is also plagued by a too high statistical scatter.

This step like behaviour of the mass distribution does not allow for a comparison with the (smooth) theoretical predictions for the mass distribution, which is crucial to the Higgs detection described in Sect. 6.4. Several suggestions have been made to overcome this shortcoming in the usage of four specialised neural networks:

- Smoothing of the mass distribution by cutting on a discriminative variable which is the average of the NN_{out} variables of two neighbouring mass intervals. The average is weighted with the inverse distance to the centre of the respective mass interval:

$$\begin{aligned} NN_{\text{comb}} &= \frac{1}{\frac{1}{c_1-m}+\frac{1}{m-c_2}}\left(\frac{1}{c_1-m}\cdot NN_1+\frac{1}{m-c_2}\cdot NN_2\right) \\ &= \frac{m-c_2}{c_1-c_2}\cdot NN_1+\frac{c_1-m}{c_1-c_2}\cdot NN_2 \end{aligned} \tag{6.16}$$

  where m is the reconstructed $t\bar{t}$ mass, c_1 and c_2 denote the centres of two adjacent mass intervals with $c_1 > m > c_2$ and NN_1 and NN_2 are the NN_{out} variables of the neural networks which correspond to the respective mass intervals. The mass distribution obtained with this procedure for four neural networks is shown in Fig. 6.46. This procedure leads to small peaks in the obtained mass distribution at the borders of the different mass intervals. The peaks are more pronounced, the harder the cut on NN_{out} is chosen. This behaviour directly comes from the averaging procedure. The differences between the efficiencies of the neural networks for two adjacent mass ranges are much larger than the variation of the efficiency within the mass range of a given neural network. This leads to a nearly linear increase in the efficiency of the combined output variable due to the linearly increasing weight of the more efficient neural network when varying the mass towards the centre of the more efficient of two adjacent neural networks.

- The scaling of the obtained mass distribution for each of the four neural networks with the inverse of the network's efficiency. This procedure joins the mass distributions within the four mass ranges for the selected signal events. However, in order to obtain a smooth mass distribution with this procedure either no or only little background should be in the selected data sample, or the ratio between the efficiencies to select signal events over the efficiency to select background events should be the same for each of the four neural networks. If neither of these conditions is fulfilled, the remaining background contribution is scaled up with the efficiency of the signal contribution, which is in no constant ratio to the background efficiency, leading

to a step like behaviour in the resulting mass distribution. In FIG. 6.47 the ratios of these efficiencies are shown. While the ratio for the first and the second neural network are somewhat similar and the ratio of the third and the fourth neural network are somewhat similar, there is a large difference between the ratios for the first and second neural network on the one and for the third and fourth neural network on the other side. Moreover, the efficiencies of the neural networks are not constant over the mass range they are trained in, but tend to be lower for low masses and to increase towards the upper end of the mass interval. This leads to an additional pronunciation of the step like structure.

Although the four specialised neural networks yield slightly better results in terms of efficiency and purity than one neural network for the whole mass range, the use of four neural networks leads to distortions of the mass distributions which hinder the intended comparison of the mass distribution with theoretical predictions and would have to be corrected for. The only small increase in sampling efficiency does not justify an additional artificial correction, so only one neural network for the whole mass range will be used in the following studies. Its properties have been discussed in the previous sections and its discriminating power is only slightly below the discriminating power of the four specialised neural networks, which will not have a large impact on the outcome of the analysis.

6.4 Search for Higgs Boson Production in the Mass-Spectrum

After the selection of events with $t\bar{t}$ pairs described in the previous section, this section deals with the identification of a possible contribution due to Higgs decays to the distribution of the invariant $t\bar{t}$ mass of the selected $t\bar{t}$ sample. The method utilises a comparison of the 'measured' mass distribution with theoretical predictions for these distributions which include Higgs contributions as well as with predictions which do not include this contribution. However, the simulation used to obtain the pseudo data sample does not take the interference between the two $t\bar{t}$ production processes into account. Therefore, before discussing the analysis of the obtained mass distributions, the inclusion of the interference into the simulated data sample is discussed.

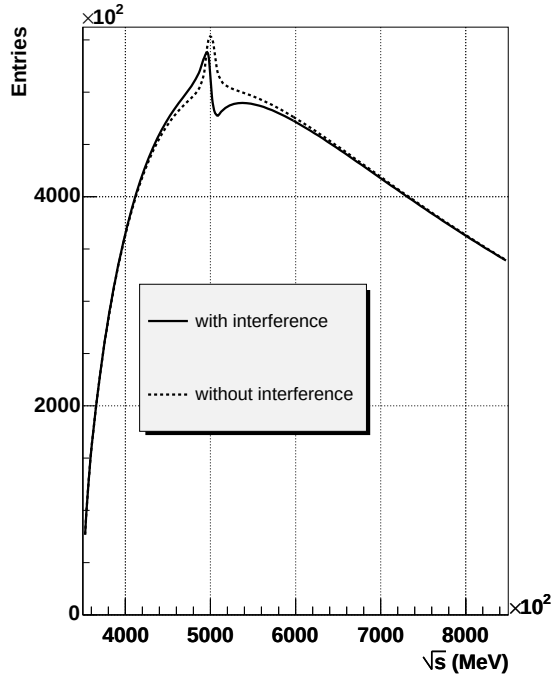

Figure 6.53: The total cross-section for $t\bar{t}$ production with the contribution due to H^0 decays. The solid line represents the full prediction, the dashed line represents the cross-section without interference between the two production channels, as it is implemented in the Monte-Carlo simulation

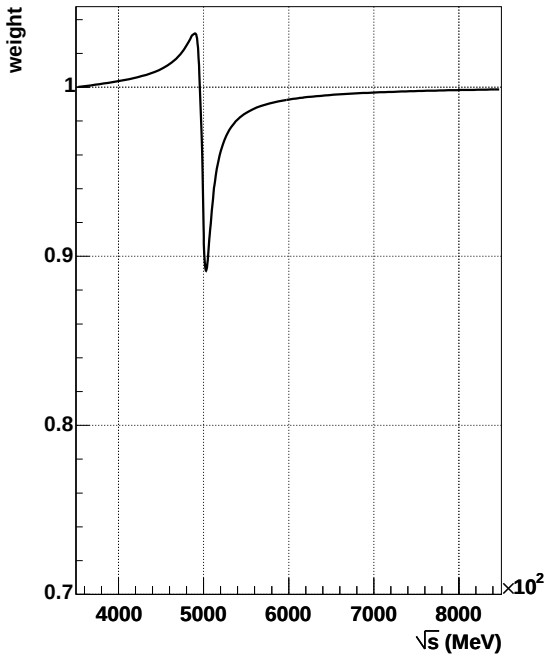

Figure 6.54: The ratio of the two curves shown in FIG. 6.53 which is used as an event weight

6.4.1 Introduction of the Interference

After applying cuts to increase the fraction of events with $t\bar{t}$-pairs in the selected event sample, the invariant mass of the reconstructed $t\bar{t}$ pair is calculated. The mass distribution of the background events provides a continuous distribution of mass-values, while the signal events will be concentrated in the region around the Higgs mass and produce a peak on top of the background distribution. As already discussed in SECT. 5.2.1 additionally to the more or less pronounced mass peak of the Higgs boson, the interference between the QCD-production and the Higgs-production of $t\bar{t}$-pairs provides a signature for the existence of the Higgs

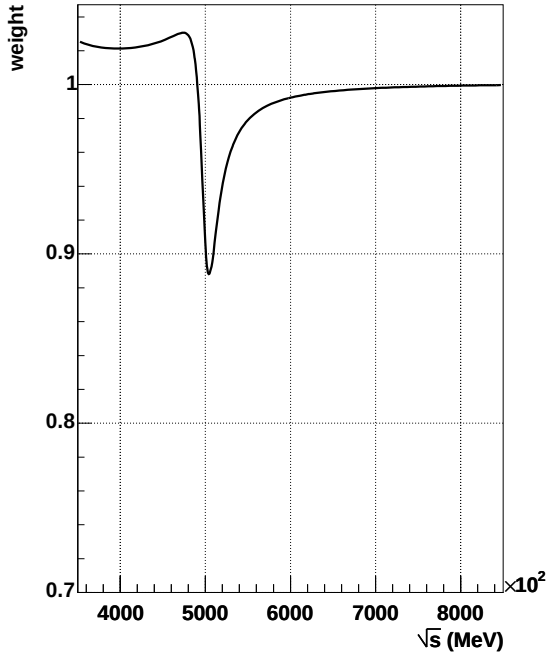

Figure 6.55: The ratio between the theoretical prediction including the contribution due to A^0-decays with interference and the same prediction, but without the interference term. This ratio is later used as part of the event weight for the Monte-Carlo simulation.

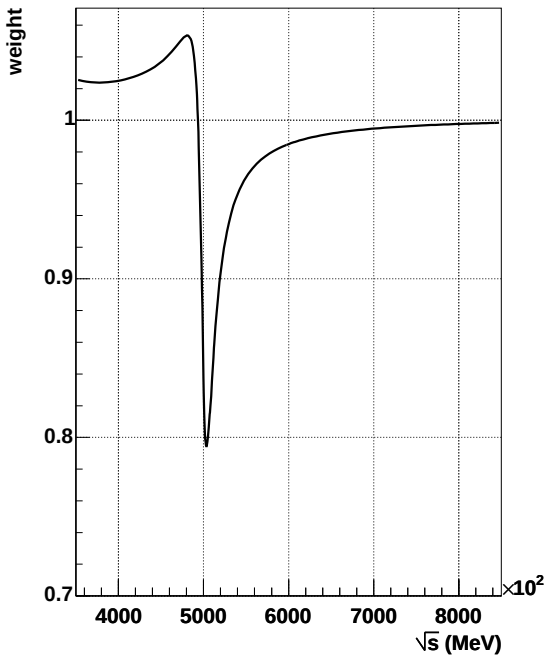

Figure 6.56: The ratio between the theoretical prediction including the contribution due to decays of H^0- and A^0-bosons with interference and the same prediction, but without the interference term. This ratio is later used as part of the event weight for the Monte-Carlo simulation.

boson. For high Higgs masses this interference signature is even more significant than the mass peak itself (see FIG. 5.12. Unfortunately, this interference is not yet implemented in the PYTHIA Monte-Carlo simulation package. A method to introduce the interference in the simulated events is described in the following section, before the mass spectra are studied.

In FIG. 6.53 the theoretical prediction for the $t\bar{t}$-production cross-section for strong interactions and H^0-decays is shown with an assumed Higgs mass of $m_{H^0} = 500$ GeV, where the solid line represents the full calculation, while the dashed line represents the contributions coming from the production processes, but neglecting the interference, as it is realised in the PYTHIA simulation. It

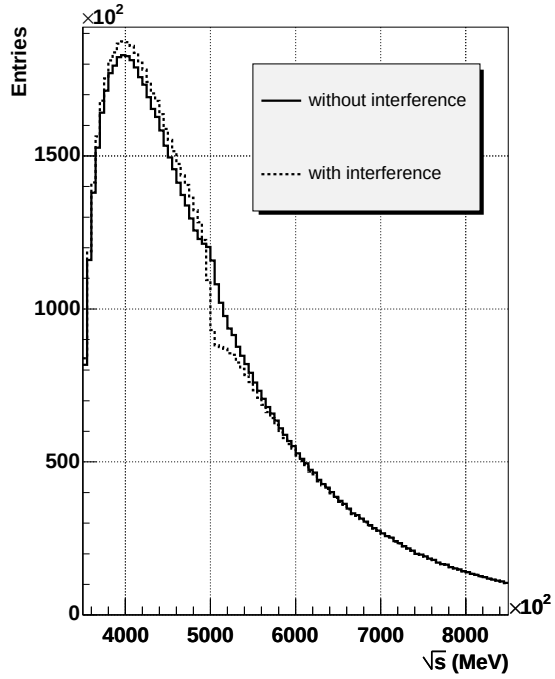

Figure 6.57: The distribution of the invariant $t\bar{t}$ mass reconstructed from the parton level information of the Monte-Carlo simulation with and without introduction of the interference through event weights

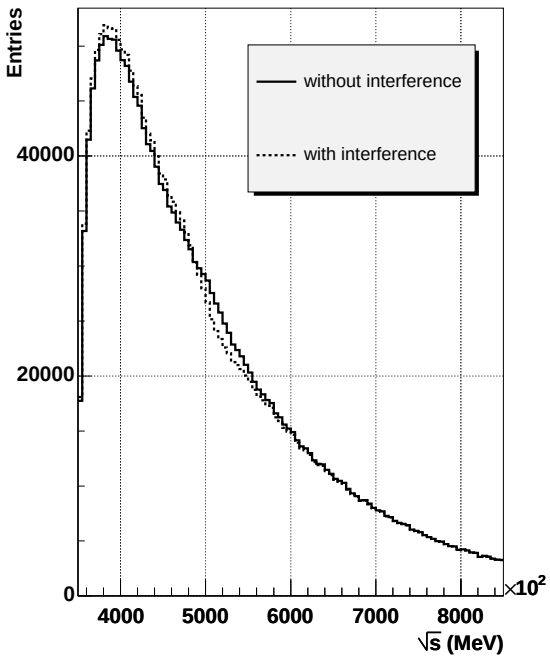

Figure 6.58: The distribution of the invariant $t\bar{t}$ mass reconstructed from the jet information of the Monte-Carlo simulation with and without introduction of the interference through event weights

can be seen that the consideration of the interference leads to a slightly increased cross-section at energies smaller than the Higgs mass, a diminished peak and a deep dip at energies slightly higher than the peak position. FIG. 6.54 shows the ratio between these two cross-sections as a function of the centre-of-mass energy of the initial hard interaction. Its structure reflects the differences discussed above: For energies smaller than the assumed Higgs mass it is larger than one, at energies higher than the assumed Higgs mass it shows a strong dip to low values and stays smaller than one over a large energy range. In FIG. 6.55 and FIG. 6.56 the respective ratios obtained under consideration of the production of A^0-Higgs bosons as well as the production of degenerate H^0/A^0 are shown. They show a behaviour similar to the ratio given in FIG. 6.54 but vary in scale and shape.

In order to introduce these interference effects into the Monte-Carlo simulation,

the generated events are weighted according to the corresponding ratios evaluated at the generated invariant mass. Events in which a H^0 has been produced are weighted according to the ratio shown in FIG. 6.54, events in which an A^0 has been produced are weighted according to the ratio shown in FIG. 6.55, while events in which a $t\bar{t}$-pair has been produced via strong interactions are weighted according to the ratio shown in FIG. 6.56, assuming that H^0 and A^0 are degenerate in mass [44].

The effect of these event weights is shown in FIG. 6.57 for the mass distribution of the partons produced in the decays of the $t\bar{t}$-pair using the properly weighted QCD-$t\bar{t}$ event sample and the Higgs event sample in which H^0 and A^0 are produced with a degenerate mass of $m_{H^0/A^0} = 500$ GeV. The dip introduced due to the interference can be clearly seen, a slight increase of the event rate at energies lower than the assumed Higgs mass is also present. In FIG. 6.58 the same distribution is shown, this time as it is obtained using the jets initiated by the partons from the top decays. Due to the hadronisation process and inefficiencies in the jet reconstruction the structure of the interference is smeared out, but the general pattern of an increased event rate at lower and a decreased event rate at higher invariant masses than the assumed Higgs mass can still be recognised.

6.4.2 Correction for the hadronic initial state

The predictions for the cross-sections of $t\bar{t}$ production given in SECT. 5.2.2 refer to an initial state of two gluons. The experimentally realised initial state at LHC consists of two protons which contain the interacting gluons. The cross-section for the production of a $t\bar{t}$ pair in a proton collision can approximately be written as the product

$$\sigma_{pp\to t\bar{t}}(m_{t\bar{t}}) = \sigma_{gg\to t\bar{t}}(m_{t\bar{t}}) \cdot P(m_{t\bar{t}}) \tag{6.17}$$

of the cross-section for the production of a $t\bar{t}$ pair from two gluons times the probability $P(m_{t\bar{t}})$ to find two gluons with the respective invariant mass inside the two protons. While $P(m_{t\bar{t}})$ is generally only a function of the parton density functions (PDF's) of the two colliding protons, a more specific definition of $P(m_{t\bar{t}})$ is applied here for practical reasons. $P(m_{t\bar{t}})$ is calculated as

$$P(m_{t\bar{t}}) = \frac{N_{\text{rec}}(m_{t\bar{t}})}{\mathcal{L} \cdot \sigma_{gg\to t\bar{t}}(m_{t\bar{t}})} \tag{6.18}$$

where $N_{\text{rec}}(m_{t\bar{t}})$ is the number of events inside a mass bin that pass the b-tagging and the reconstruction procedure and $\mathcal{L}$ is the luminosity assumed by PYTHIA

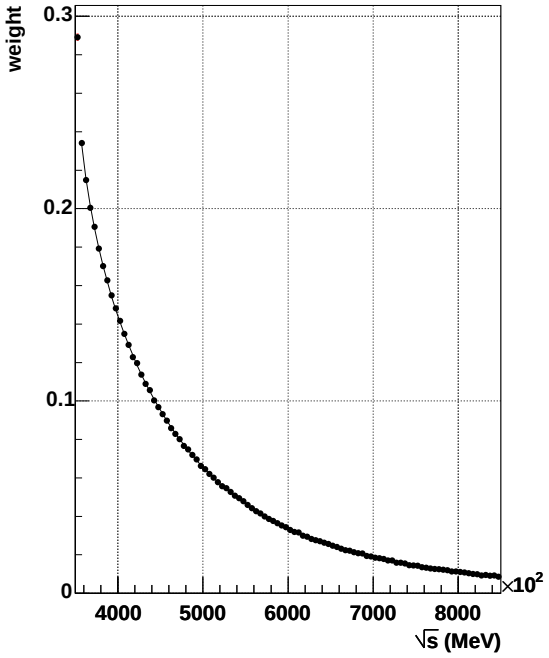

Figure 6.59: The function $P(m_{t\bar{t}})$ as defined in Eq. 6.18

to simulate the events. This definition of $P(m_{t\bar{t}})$ includes inefficiencies of the tagging and reconstruction procedure which makes $P(m_{t\bar{t}})$ not only a function of the PDF's, but also accounts for experimental effects by rescaling $P(m_{t\bar{t}})$. Fig. 6.59 shows the ratio defined in Eq. 6.18. To calculate $P(m_{t\bar{t}})$ only the sample of QCD produced $t\bar{t}$ events has been used, assuming that $P(m_{t\bar{t}})$ is the same for both samples of $t\bar{t}$ events. $P(m_{t\bar{t}})$ is around 0.3 for $m_{t\bar{t}} < 360$GeV and decreases rapidly for larger $m_{t\bar{t}}$. In order to obtain a continuous parametrisation of $P(m_{t\bar{t}})$, the function

$$P(m_{t\bar{t}}) = p_0 + p_1 \cdot m^{-p_2} + p_3 \cdot m^{-p_2 \cdot p_6} + p_4 \cdot e^{-p_5 \cdot m} \tag{6.19}$$

has been fitted to the simulated data points in Fig. 6.59. The functional expression of Eq. 6.19 is identical with the bracket term in Eq. 6.14. In the physical mass range > 355GeV the fit converges and yields a χ^2 value of 97.5 for 92 degrees of freedom. The overall description of the simulated data by the fit is good, the results for the fitted parameters are given in Tab. 6.4. However, the parametrisation Eq. 6.19 has only been chosen to obtain a smooth parametrisation for $P(m_{t\bar{t}})$ for convenience, it does not have a physical interpretation, nor do the

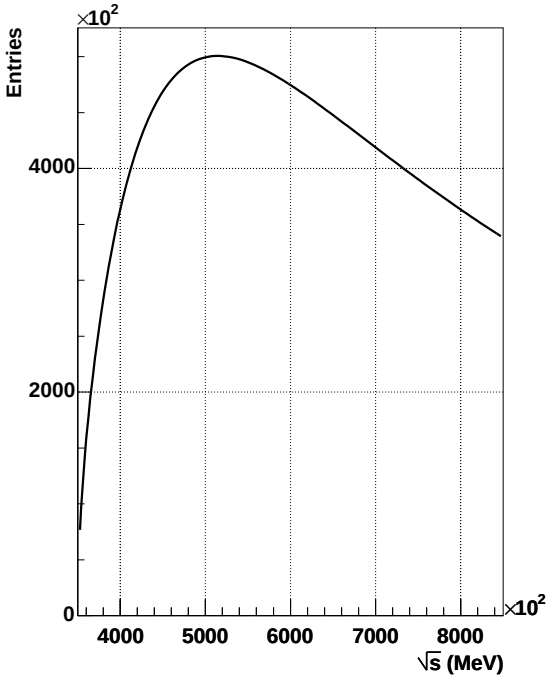

Figure 6.60: The theoretical prediction for $\sigma_{gg\to t\bar{t}}$

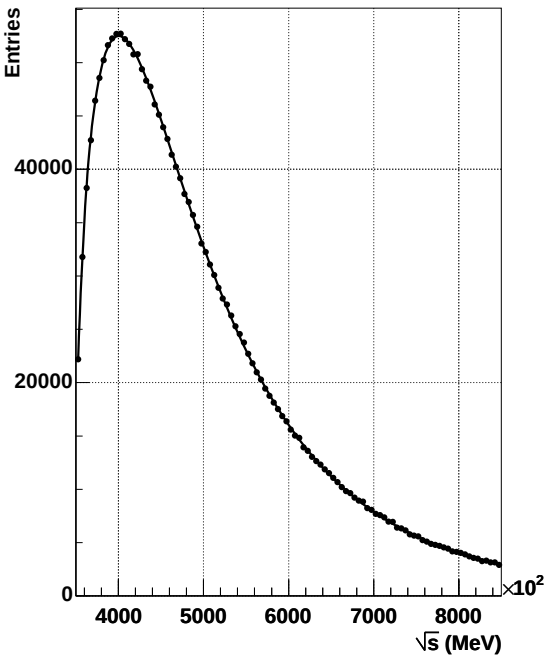

Figure 6.61: The prediction for $\sigma_{pp\to t\bar{t}}$ derived from the prediction shown in FIG. 6.60

fitted parameters. FIG. 6.60 shows the cross-section $\sigma_{gg\to t\bar{t}}$ as given by EQ. 5.8, in FIG. 6.61 the cross-section $\sigma_{pp\to t\bar{t}}$ obtained as the product of $\sigma_{gg\to t\bar{t}}$ and $P(m_{t\bar{t}})$ is shown. The multiplication with $P(m_{t\bar{t}})$ results in a narrowing of the curve and, most importantly, in a shift towards lower invariant $t\bar{t}$ masses. The maximum of $\sigma_{gg\to t\bar{t}}$ is around 500GeV, while the maximum for $\sigma_{pp\to t\bar{t}}$ is located around only 400GeV. This reflects the fact that gluons in the proton are predominantly soft and that the probability to find a gluon inside the proton decreases rapidly with increasing gluon energy.

6.4.3 Correction for limited reconstruction resolution

The reconstruction procedure with the kinematic fit gives an estimate for the invariant mass of the $t\bar{t}$ pair produced in an event. However, this estimate may deviate from the actual mass value due to detector inefficiencies, not properly

p_0	$(1.12 \pm 0.4) \cdot 10^{-3}$
p_1	$(-2.34 \pm 0.2) \cdot 10^{4}$
p_2	(1.12 ± 0.002)
p_3	$(5.02 \pm 0.13) \cdot 10^{17}$
p_4	$(7.95 \pm 0.22) \cdot 10^{10}$
p_5	$(8.1 \pm 0.76) \cdot 10^{-5}$
p_6	(2.95 ± 0.003)

Table 6.4: The parameter values for the fitted function Eq. 6.19

reconstructed jets, mis-tagged jets, etc. A mis-reconstruction of the $t\bar{t}$ mass corresponds to a horizontal shift in the mass distribution histogram. Especially the peak-dip structure is prone to be washed out, as more often events from the peak region are mis-reconstructed with masses in the dip region than vice versa, leading to a net flux of events from the peak to the dip thus levelling the peak-dip structure. This kind of effect cannot be represented by a multiplicative factor, as the effect introduces correlations between different bins of the mass distribution histogram. Instead, a matrix operation has to be applied to the theoretical prediction to simulate the effect of the limited reconstruction resolution.

In Fig. 6.62 the distribution of reconstructed $t\bar{t}$ masses (abscissa) is shown for different generated $t\bar{t}$ masses (ordinate). This distribution is obtained using QCD produced $t\bar{t}$ events which underwent the reconstruction procedure. The jets produced by the $t\bar{t}$-decay are identified using the b-tagging procedure and the p_T ordering assumptions described in Sect. 6.2. A concentration of entries can be observed around the main diagonal, representing an approximately correct reconstruction of the $t\bar{t}$ mass. However, a broad distribution around this concentration is also present, indicating that the mass is in a substantial fraction of the events not reconstructed correctly. A tendency to reconstruct the mass lower than it was generated can be observed in the larger amount of entries up-left of the main diagonal than down-right of the diagonal.

One reason for the misreconstruction of the $t\bar{t}$ mass are the assumptions made to identify the jets originating in the $t\bar{t}$ decay. Fig. 6.63 shows the distribution which is obtained when the jets which are known to originate from the $t\bar{t}$-pair are used to reconstruct $m_{t\bar{t}}$. The concentration around the main diagonal is much stronger than in Fig. 6.62 and the distribution around the main diagonal is much more narrow, both indicating a more reliable reconstruction of the $t\bar{t}$ mass. This clearly shows that an improvement of the analysis can be achieved by a more sophisticated selection procedure for the jets entering the reconstruction process.

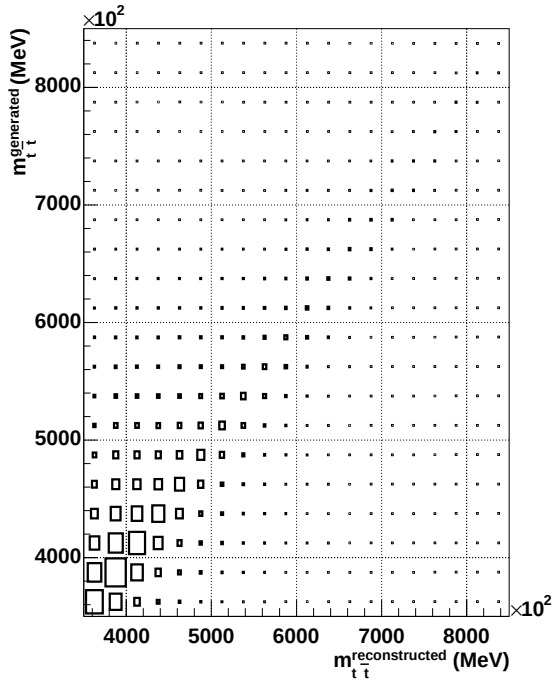

Figure 6.62: The reconstructed invariant $t\bar{t}$ masses in dependence of the generated $t\bar{t}$ mass

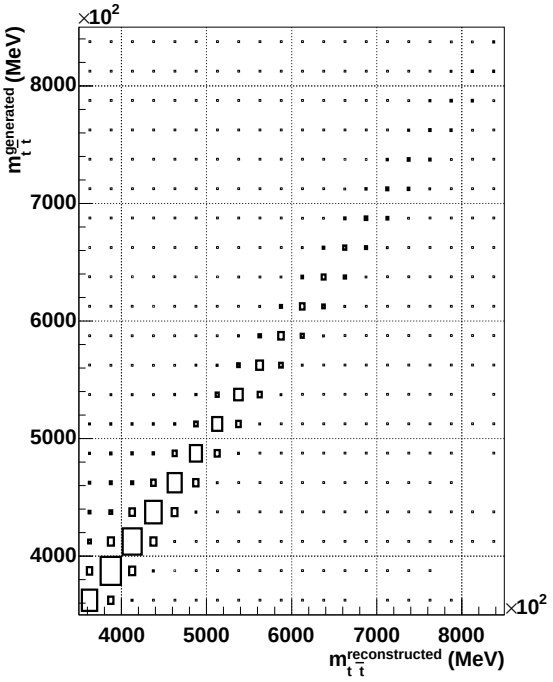

Figure 6.63: The reconstructed invariant $t\bar{t}$ masses in dependence of the generated $t\bar{t}$ mass when the jets known to originate form the $t\bar{t}$ decay are used for reconstruction

FIG. 6.64 shows the reconstructed $t\bar{t}$ mass versus the generated $t\bar{t}$ mass distribution which is obtained after selecting the jets due to the b-tagging and the p_T ordering criteria also a cut in the neural network output of $NN_{\text{out}} > 0.99$ is applied. An improvement of the reconstruction can be observed. The cut in NN_{out} is more likely to reject badly reconstructed events than events which are reconstructed relatively well.

In FIG. 6.65 and FIG. 6.66 the effect of applying the matrix to the theoretical predictions for the distribution of $m_{t\bar{t}}$ is shown. The theoretical prediction shown in both figures as a dashed line includes direct $t\bar{t}$ production via gluon fusion as well as $t\bar{t}$ production via Higgs decays and the resulting interference. The theoretical prediction has already been multiplied with the correction function for the hadronic initial state $P(m_{t\bar{t}})$ as described in SECT. 6.4.2.

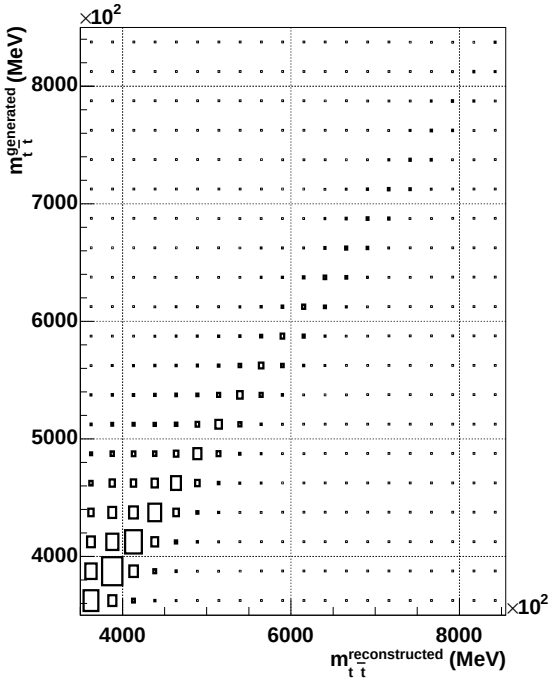

Figure 6.64: The reconstructed invariant $t\bar{t}$ masses in dependence of the generated $t\bar{t}$ mass when the cut $NN_{\text{out}} > 0.99$ is applied

The solid line in FIG. 6.65 shows the result of applying the correction matrix for the case that the jet known to originate in the $t\bar{t}$ decay are used for reconstruction as it is shown in FIG. 6.63 to the theoretical prediction indicated by the dashed line. The steep flank of the interference dip which is very prominent in the uncorrected theory is nearly completely washed out due to the imperfect mass reconstruction even in the ideal case that the correct jet pairing is known. However, even if the clearly localised peak-dip signature of the presence of a Higgs contribution disappears, a significant difference between the matrix corrected theory with a Higgs contribution and the matrix corrected theory without this contribution, which is indicated as a dotted line in FIG. 6.65, can be seen.

The solid line in FIG. 6.66 shows the result of applying the matrix correction shown in FIG. 6.64 to the theoretical prediction. This correction includes the effects of the misidentification of the jets from the $t\bar{t}$ decays as well as the effect of a cut on $NN_{\text{out}} > 0.99$. The inefficiency of the cut in NN_{out} is taken into account by the normalisation of the rows of the correction matrix, which is generally smaller than one due to the rejection of events. Due to this inefficiency, the matrix

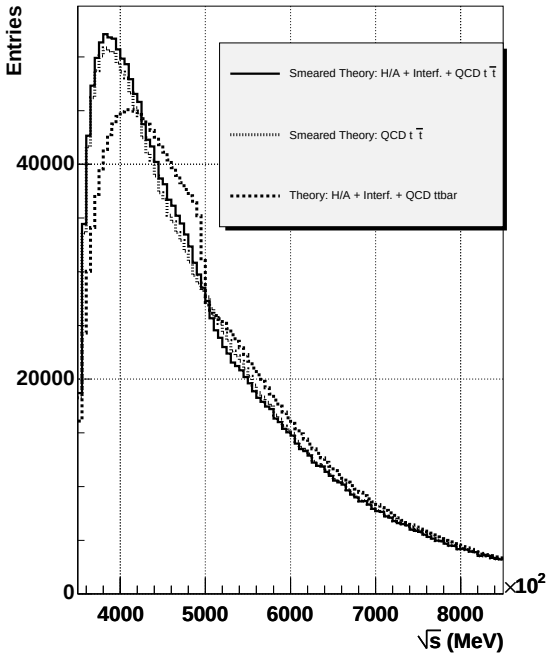

Figure 6.65: The theoretical prediction for the $t\bar{t}$ mass distribution before and after applying the matrix correction for reconstruction errors shown in FIG. 6.63

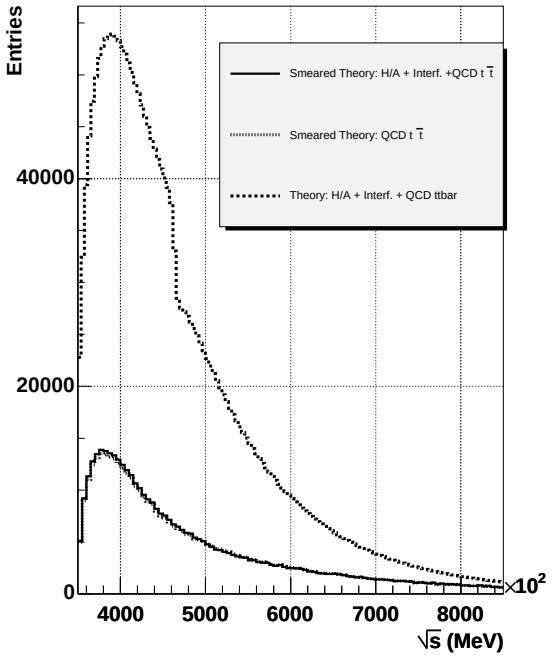

Figure 6.66: The theoretical prediction for the $t\bar{t}$ mass distribution before and after applying the matrix correction for reconstruction errors shown in FIG. 6.64

corrected prediction is much lower than the uncorrected prediction. Again, the prominent signature of a Higgs contribution is washed out and the difference between the matrix corrected prediction with Higgs contribution and the matrix corrected prediction without this contribution, as indicated by the dotted line, is much smaller than the difference found in FIG. 6.65 where the correctly identified jets from $t\bar{t}$ decays enter the reconstruction.

6.4.4 Comparison with theory

The main experimental goal of this analysis is to decide if in a given data sample of $t\bar{t}$-events a contribution due to decays of Higgs bosons is present or not. In order to make this decision, the distribution of the invariant $t\bar{t}$-masses of the data

sample is compared to theoretical predictions of this distribution. The following hypotheses are tested:

- **Hypothesis:** A Higgs contribution to the spectrum of invariant $t\bar{t}$-masses is present.
- **Antithesis:** No Higgs contribution is present, the spectrum of invariant $t\bar{t}$-masses is described by QCD production only.

The predictions are calculated for both, the hypothesis as well as the antithesis. In order to quantify the agreement of the data with the hypothesis or the antithesis, the bin-wise sum of the χ^2-values [54]

$$\chi^2 = \sum_i \chi_i^2 = \sum_i \left(\frac{d_i - t_i}{e_i} \right)^2 \tag{6.20}$$

is calculated. Here, d_i denotes the number of events in bin i of the histogrammed mass distribution of the data, e_i its uncertainty and t_i the number of events predicted for this bin by the respective theory. The theoretical prediction for the hypothesis depends on the mass of the assumed Higgs-boson, which is a priori not known. Therefore, the theoretical prediction including a contribution due to Higgs decays is calculated for different assumptions of the Higgs mass and χ^2 is calculated for each assumption. In this way, χ^2 for the hypothesis becomes a function of the assumed Higgs mass $m_{H/A}$.

The signature for the presence of a Higgs contribution to a given distribution of reconstructed $t\bar{t}$ masses would be a single local minimum in the function $\chi^2(m_{H/A})$, where the minimal χ^2-value should be significantly smaller than the χ^2-value obtained testing the antithesis that no contribution due to Higgs decays is present. The position of the minimum could then be interpreted as an estimator for the mass of the Higgs boson.

The signature of the absence of a contribution due to Higgs decays could also be observed in the χ^2 function for the hypothesis that a Higgs contribution is present. In this case, it would show generally higher values than the χ^2 value obtained for the antithesis, that no Higgs contribution is present.

In order to understand how good this procedure is principally working, first an ideal world scenario is studied, in which no background due to QCD light jet events is present and where the jets which are the products of the $t\bar{t}$ decay are known. A scenario closer to the reality of a physics analysis is discussed afterwards. This allows one also to understand where the largest amount of information is lost during the analysis procedure and which steps have to be improved upon.

In FIG. 6.67 the $m_{t\bar{t}}$ distribution of the simulated data sample without a Higgs contribution is compared to the theoretical predictions for the hypothesis (that a Higgs contribution is present) and for the antithesis (that no Higgs contribution is present). In order to reconstruct the $t\bar{t}$ masses in the simulated data sample, the jets known to be decay products of the $t\bar{t}$ pair have entered the reconstruction. The left plot in FIG. 6.67 shows the direct comparison of the predictions with the simulated data, in the right plot the pull between the data and the hypothesis (solid dots) and between the data and the antithesis (open dots) are shown to make the differences more visible. For these plots the prediction for the hypothesis has been calculated for an assumed Higgs mass of 500GeV, which is the mass of the simulated Higgs boson. A good description of the distribution by the antithesis can be seen, the pull values are generally smaller than one. However, a small oscillating structure is to be observed. The relatively smooth behaviour of the pull values is caused by a correlation between neighboring bins introduced by the applied matrix correction. The comparison with the hypothesis shows the expected pattern of a large overestimation of the spectrum left of the assumed Higgs mass and an underestimation of the spectrum right of the assumed Higgs mass which peaks directly above the assumed Higgs mass.

In FIG. 6.68 the same plots are shown for the simulated data sample containing a Higgs contribution. Here, the pull of the comparison with the antithesis shows a behaviour inverse to the behaviour of the pull for the hypothesis shown in FIG. 6.67: The antithesis underestimates the mass spectrum left of the simulated Higgs mass, while it overestimates the spectrum right of the Higgs mass, the overestimate peaks directly above the simulated Higgs mass. The description of the mass distribution by the hypothesis is much better, the pull values are mainly of an absolute value smaller than one. However, in the vicinity of the simulated Higgs mass a clear peak in the pull with values up to -7 can be seen. The reason for this can be understood with FIG. 6.69. Here, the mass distribution for the simulated Higgs bosons as it is obtained from the partonic decay products is compared to the part of the prediction which corresponds to the mass peak of degenerate H/A-bosons with a mass of 500GeV, without the terms for the QCD production of $t\bar{t}$-pairs and interference. The description of the simulated Higgs mass peak by the theory is not perfect, especially a larger asymmetry with more events left of the Higgs mass can be observed in the simulated Higgs peak. These differences are most likely caused by higher order corrections which are to some extent built into the simulation program but are not included in the theoretical prediction. However, the description of the mass spectrum in FIG. 6.68 by the hypothesis is overall still much better compared to the description by the antithesis. The difference between simulated and predicted mass peak is therefore only limiting to this analysis, but not prohibitive.

FIG. 6.70 shows the χ^2 values obtained when the hypothesis is compared to the simulated data sample without a Higgs contribution as a function of the Higgs mass assumed in the hypothesis. The χ^2-values correspond to 100 degrees of freedom. The χ^2 values are large and decrease fast with increasing Higgs masses. This behaviour can be easily understood by consulting FIG. 5.12: The size of the signature of a Higgs contribution becomes smaller for larger Higgs masses. Furthermore, a part of the Higgs signal migrates out of the mass-range which is considered in the sum of χ^2 when the Higgs mass is increased. This, together with the increasing statistical errors at high reconstructed $t\bar{t}$ masses in the data sample, leads to relatively small values of χ^2 when high Higgs masses are assumed. The corresponding χ^2-value for the antithesis and the data sample without a Higgs contribution is $\chi^2_{\text{antithesis}} = 7.8$ indicating an excellent agreement between the simulated data distribution and the prediction.

The χ^2-values obtained in this 'ideal world' analysis are lower than the expected values for 100 degrees of freedom. The reason for this is rooted in the applied correction procedure: The matrix correction, which represents the limited experimental mass resolution of around 50GeV, spreads out information of one bin over the approximately ten neighbouring bins. As a result of this, these bins become correlated and statistical fluctuations become equalised. This results in generally overestimated statistical errors and subsequent too low χ^2-values. However, as in the determination of exclusion limits only the differences of the χ^2-values are studied, this is not expected to affect the analysis result significantly.

FIG. 6.70 can be used to derive exclusion limits for the presence of a Higgs contribution. The presence of such a contribution can only be excluded with a sufficient probability (confidence), if the difference between the $\chi^2_{\text{hypothesis}}$ obtained under the assumption of a Higgs contribution with a given Higgs mass and the $\chi^2_{\text{antithesis}}$ value obtained under the assumption of the absence of any Higgs contribution is sufficiently large. To this end,

$$\Delta\chi^2(m_{H/A}) = \chi^2_{\text{hypothesis}}(m_{H/A}) - \chi^2_{\text{antithesis}} \tag{6.21}$$

is calculated. The interpretation of the $\Delta\chi^2$ value is connected to the treatment of $\Delta\chi^2$ when obtaining errors for fitted parameters. The predictions for hypothesis and antithesis can be written as

$$\sigma_{\text{tot}}(m_{t\bar{t}}) = x \cdot (\sigma_{\text{Higgs}}(m_{t\bar{t}}) - \sigma_{\text{interf}}(m_{t\bar{t}})) + \sigma_{\text{QCD}-t\bar{t}}(m_{t\bar{t}}) + \sigma_{\text{lj}-\text{bkg}}(m_{t\bar{t}}) \tag{6.22}$$

where the antithesis that the spectrum does not contain contributions due to Higgs decays, but only consists of the QCD produced $t\bar{t}$-pairs and the light jet background, is realised by $x = 0$, while the hypothesis that also a Higgs contribution is present corresponds to the case $x = 1$. With which confidence a Higgs

contribution to the mass spectrum can be excluded is therefore equivalent to the question which confidence interval around $x = 0$ excludes the value $x = 1$. For a confidence of 95%, the interval around $x = 0$ is determined by the condition $\Delta\chi^2 \leq 1.64$. Therefore, a contribution due to Higgs decays can be excluded as long as the difference between the χ^2-values obtained with the hypothesis and the antithesis remains larger than this value [56].

In FIG. 6.72 the $\Delta\chi^2$ values derived from the values in FIG. 6.70 are shown. A solid line indicates the value $\Delta\chi^2 = 1.64$. For all the studied mass range the difference between the χ^2-values for hypothesis and antithesis stays larger than 1.64 so that a Higgs contribution could be excluded over all this mass range.

In FIG. 6.71 the χ^2 values for the test of the hypothesis against the simulated data sample containing the contribution due to Higgs decays are shown. The χ^2 values fall steeply until a clear and narrow local minimum is reached at an assumed Higgs mass of around 500GeV after which the function rises steeply again and stays relatively flat at high values of χ^2. This corresponds to the behaviour expected, if a Higgs contribution is present. The minimum value of χ^2 is 128.7, while the χ^2 value for the antithesis is 1780, both for 100 degrees of freedom. This result would clearly indicate the presence of a Higgs contribution with a Higgs mass around 500GeV in a given data sample. However, although a clear minimum can be seen in the χ^2 values in FIG. 6.71 and the χ^2 value in the minimum is well below the χ^2 value for the antithesis, the minimum χ^2-value of 128.7 is surprisingly large, especially considering that the χ^2-values are expected to come out rather small in this analysis due to the correlation introduced by the matrix correction as discussed above. The reason for this is that the shape of the Higgs peak in the mass distribution of the Monte-Carlo is not described perfectly by the prediction, as can be seen in FIG. 6.69. Nevertheless, the clear minimum in the χ^2 curve can be interpreted as a signal for the presence of a resonance.

The optimistic assumptions made in the scenario above are unfortunately not realistic for an analysis of real data. The main setbacks are that the jets coming from the decay of the $t\bar{t}$ pair cannot be identified with certainty and that a large amount of background events due to QCD light jet events will be present in the data sample. In the following, the results of the analysis procedure will be studied taking these effects into account.

Even after the event selection including a cut in NN_{out}, the accepted simulated data sample contains a significant contribution due to QCD light jet events. In order to obtain meaningful χ^2 values, this contribution has to be taken into account in the functions used to represent the mass distribution of the hypothesis and the antithesis. Therefore, the fitted function EQ. 6.14, which has been used

to generate a randomly scattered mass distribution for accepted QCD light jet events, is added to both predictions. In a runnning experiment at LHC the shape of the QCD light jet background will be measured with high precision.

In FIG. 6.73 the $m_{t\bar{t}}$ distributions for the simulated data sample without a Higgs contribution is compared to the theoretical predictions, FIG. 6.74 shows the same comparison for the simulated data sample with a Higgs contribution. Again, the pulls of the data with respect to the predictions are shown on the right side of the figures, solid dots for the comparison with the hypothesis, open dots for the comparison with the antithesis. The jets entering the reconstruction of the $t\bar{t}$ mass are selected by b-tagging and p_T-ordering as described SECT. 6.2. Additionally, the cut $NN_{\text{out}} > 0.99$ has been applied to suppress events from the QCD light jet background. Both samples still contain residual contributions due to this background, which are included as described in SECT. 6.3.4. In both plots the differences indicated by the pulls are relatively small, the pulls for both predictions are scattered around mainly between -2 and 2. Both mass distributions in FIG. 6.73 and FIG. 6.74 are described well by the theoretical predictions with very little difference between the predictions for hypothesis and antithesis. This in comparison with FIG. 6.67 and FIG. 6.68 reduced difference between both predictions is in part due to the larger effect of the matrix correction for the limited reconstruction resolution, which here also corrects for experimental acceptance, in part due to the huge contribution of the QCD light jet background, which is added to both predictions and reduces the relative size of the differences due to the Higgs contribution.

In FIG. 6.75 the χ^2 values of the comparison of the hypothesis to the data sample without a Higgs contribution is shown. The χ^2 function starts at values around 200 and decreases fast for larger assumed Higgs masses. The χ^2 value for the antithesis is 71.1 for this data sample.

The corresponding $\Delta\chi^2$-values are shown in FIG. 6.77. For a large part of the studied mass range $\Delta\chi^2$ is larger than 1.64, indicating that a Higgs contribution to the mass spectrum could be excluded with a confidence of 95% up to a Higgs mass of $\sim$ 850GeV.

In FIG. 6.76, the χ^2 values of the comparison between the hypothesis and the data sample containing a Higgs contribution is shown. The χ^2 function start at a moderate χ^2 value of around 200 and drops sharply to a local minimum, which is still clearly pronounced at 500GeV, although it is less deep, but wider than the one in FIG. 6.71. The minimal χ^2 value for the hypothesis of 74.3 has to be compared to the χ^2 value of the antithesis, which is 108.3 for the simulated data sample containing a Higgs contribution.

The lower χ^2 values in FIG. 6.75 and FIG. 6.76 as compared to FIG. 6.70 and FIG. 6.71 are mainly caused by the large QCD light jet background contribution, due to which the statistical errors of the counting rates are increased, while the difference between the presence and the absence of a Higgs contribution stays constant.

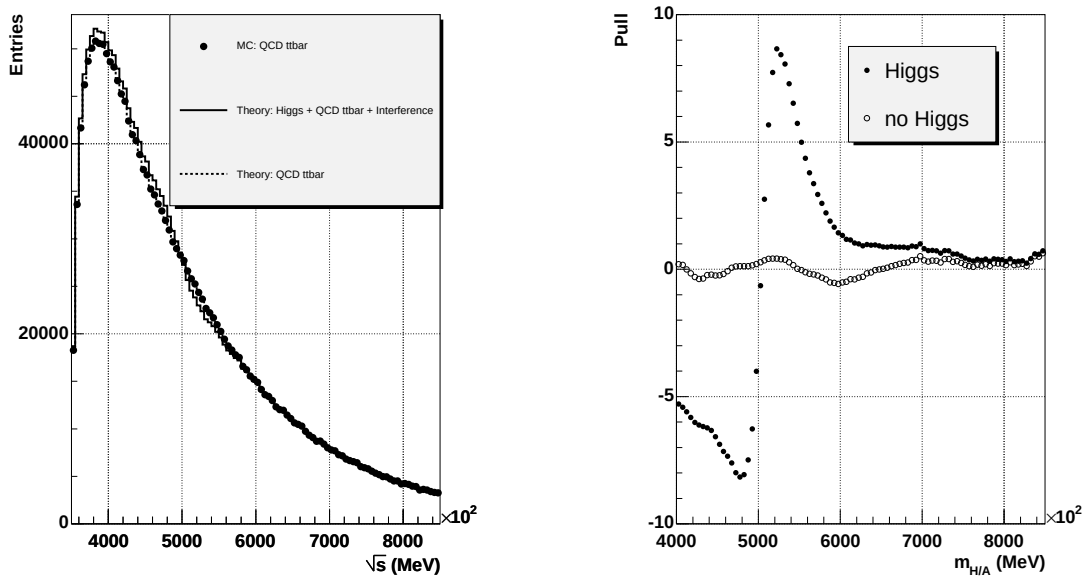

Figure 6.67: The mass distribution obtained from the data sample without a Higgs contribution in comparison with theoretical predictions with and without a Higgs contribution. The jets known to be decay products of the $t\bar{t}$ pair have been used for reconstruction. The left plot shows the mass distribution, the right plot the pull of the data with respect to the hypothesis (solid dots) and the antithesis (open dots).

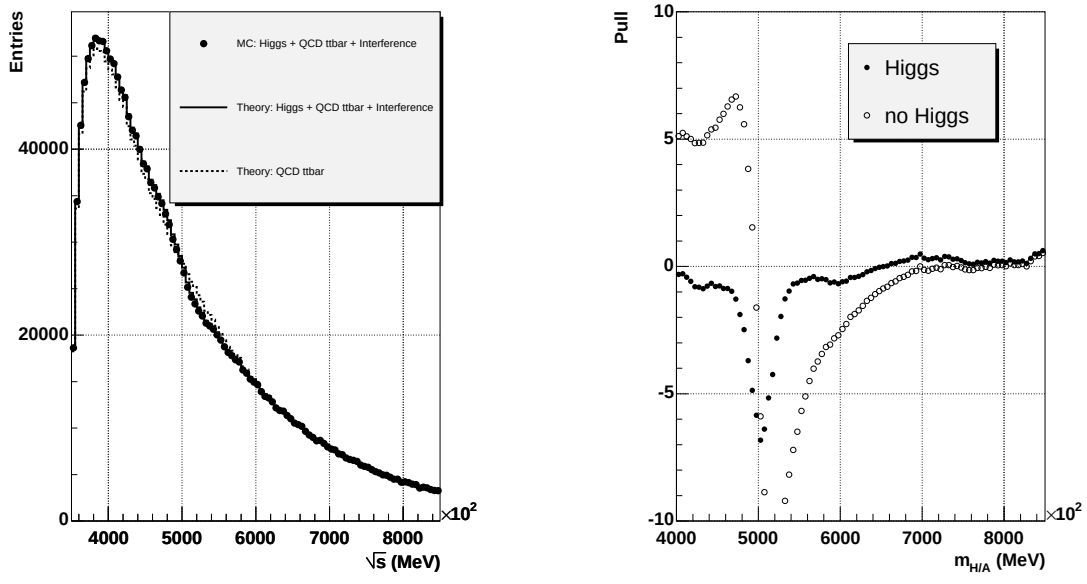

Figure 6.68: The mass distribution obtained from the data sample with a Higgs contribution in comparison with theoretical predictions with and without a Higgs contribution. The jets known to be decay products of the $t\bar{t}$ pair have been used for reconstruction. The left plot shows the mass distribution, the right plot the pull of the data with respect to the hypothesis (solid dots) and the antithesis (open dots).

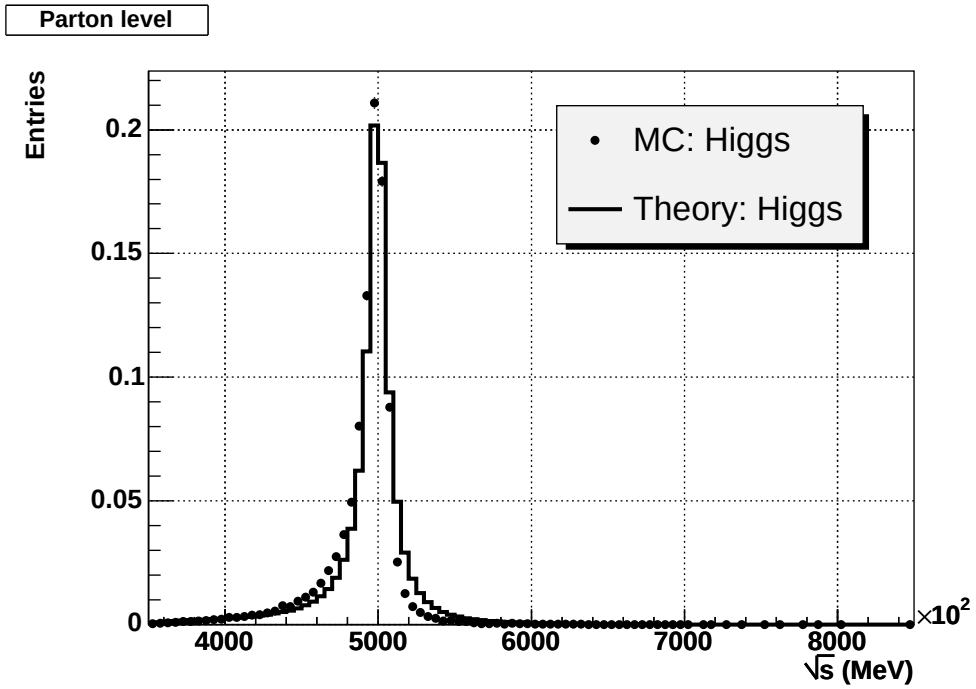

Figure 6.69: The distribution of the invariant $t\bar{t}$ mass in the simulated sample of Higgs decays in comparison with the prediction for the shape of the H/A peak

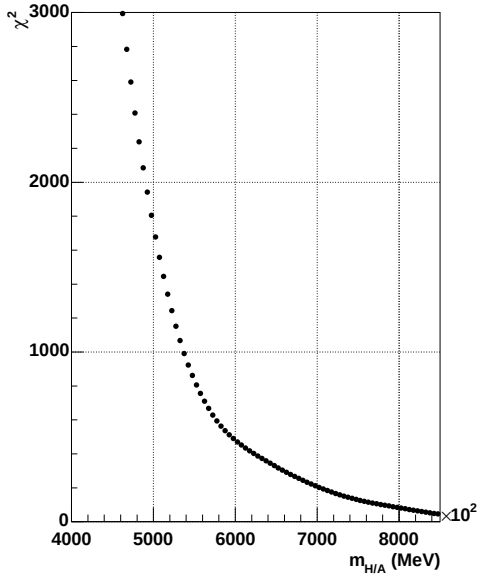

Figure 6.70: The χ^2 values obtained from the simulated data without a Higgs contribution as shown in FIG. 6.67

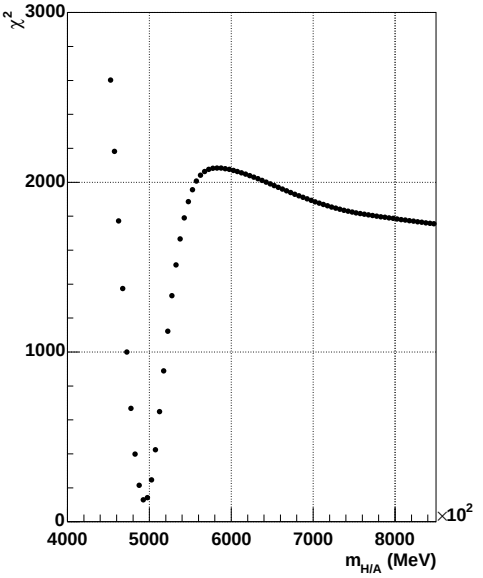

Figure 6.71: The χ^2 values obtained from the simulated data with a Higgs contribution as shown in FIG. 6.68

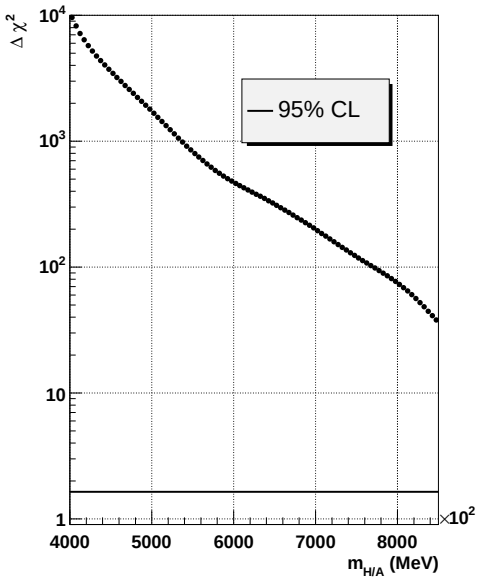

Figure 6.72: The $\Delta\chi^2$-values obtained using the jets known to be decay products of the $t\bar{t}$-pair. The solid horizontal line indicates $\Delta\chi^2 = 1.64$.

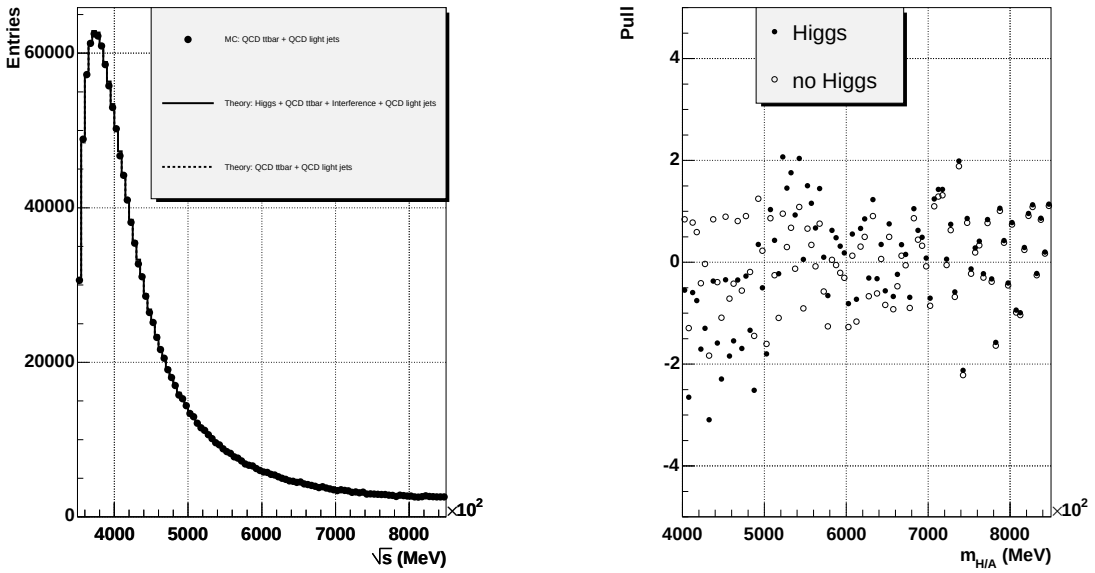

Figure 6.73: The mass distribution obtained from the data sample without a Higgs contribution in comparison with theoretical predictions with and without a Higgs contribution. The jets entering the reconstruction have been selected using b-tagging and ordering in p_T. The left plot shows the mass distribution, the right plot the pull of the data with respect to each of the two predictions

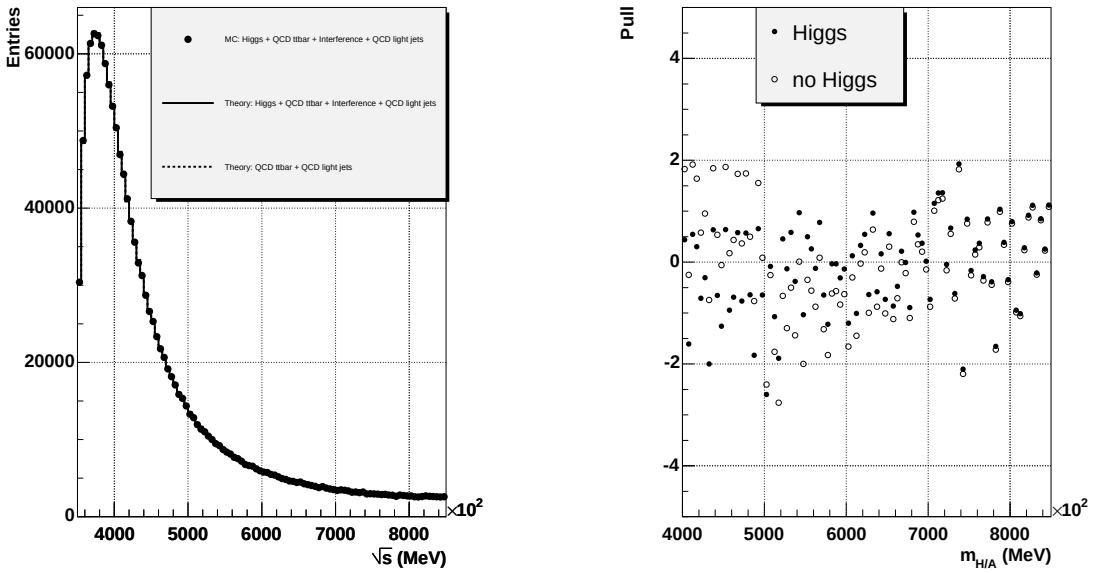

Figure 6.74: The mass distribution obtained from the data sample with a Higgs contribution in comparison with theoretical predictions with and without a Higgs contribution. The jets entering the reconstruction have been selected using b-tagging and ordering in p_T. The left plot shows the mass distribution, the right plot the pull of the data with respect to each of the two predictions

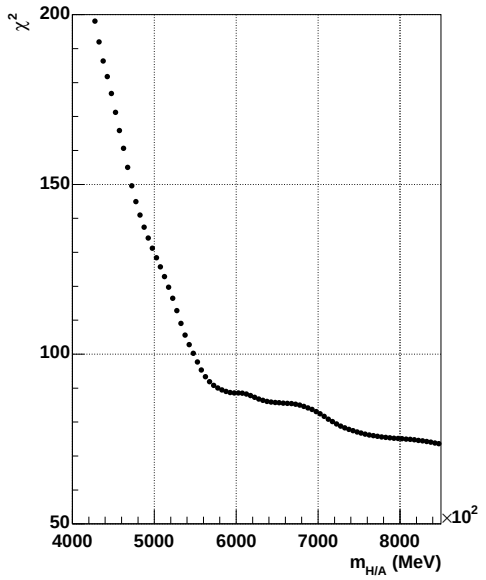

Figure 6.75: The χ^2 values obtained from the simulated data without a Higgs contribution as shown in FIG. 6.73

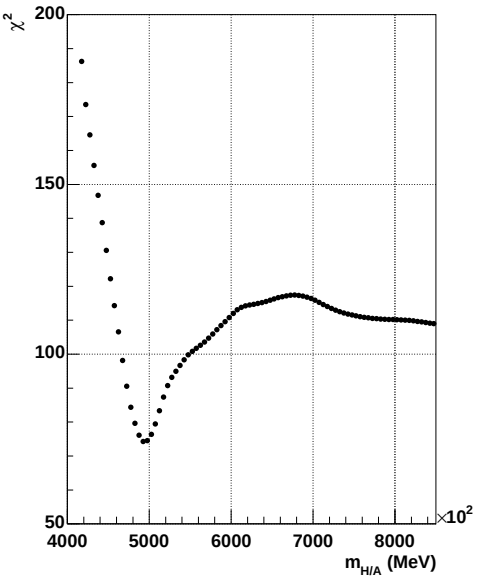

Figure 6.76: The χ^2 values obtained from the simulated data with a Higgs contribution as shown in FIG. 6.74

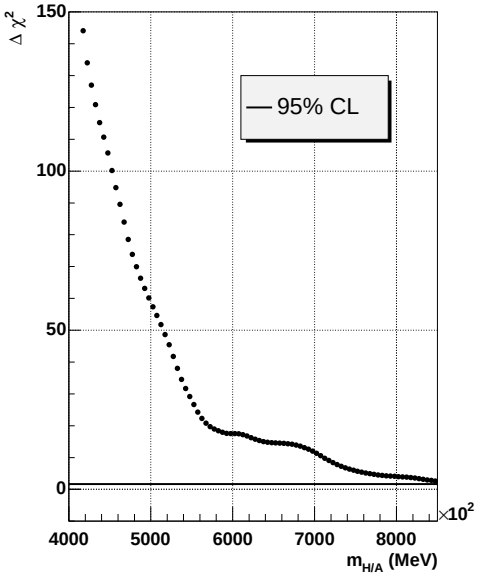

Figure 6.77: The $\Delta\chi^2$-values obtained using tagged jets as input to the analysis. The solid horizontal line indicates $\Delta\chi^2 = 1.64$.

Chapter 7

Trigger Studies

The analysis described in the previous chapter will now be used as an example physics analysis to investigate the influence of the trigger conditions on the prospects of physics searches. The trigger condition most important to the search of events with a $t\bar{t}$ final state is the four jet trigger which requires at least four jets with a transverse momentum higher than a given trigger threshold. However, many final states interesting to physics analyses have heavy quarks in the final state. Therefore, introducing a b-tagging criterium into the trigger requirements might significantly improve the composition of the triggered event sample.

In this chapter the prospects of introducing a b-tagging procedure into the level 2 four jet trigger for physics analyses will be discussed. For this purpose a b-tagging procedure with the same properties as the offline b-tagging discussed in Sect. 4.3 will be assumed [24].

In the first section general properties of the level 2 four jet trigger with a b-tagging procedure are discussed, especially with respect to the option to lower the trigger threshold when the b-tagging is included in the trigger. In Sect. 7.2 the analysis discussed in Chap. 6 will be shortly summarised before in Sect. 7.3 the impact of the trigger on the outcome of the analysis will be discussed.

7.1 Properties of the Trigger and the b-tagging

The main benefit of a trigger with b-tagging is that the additional constraint due to the b-tagging reduces the total number of triggered events at a given setting of trigger thresholds. This would allow for lowering the trigger thresholds

within the constraints given by the limited read-out bandwidth. As the b-tagging criterium is expected to suppress mainly QCD light jet events, which will be produced in abundance and are of only limited interest to many physics analyses, the combination of b-tagging and lower trigger thresholds is expected to increase the fraction of events interesting to physics analyses in the triggered event sample.

In order for the combination of b-tagging and lower trigger thresholds to improve the triggered data sample, two conditions have to be met:

1. The total number of triggered events must not be increased
2. The efficiency to trigger signal ($t\bar{t}$-) events should be increased

The first condition can be expressed as

$$\underbrace{\frac{N(x)}{N_0}}_{\equiv Y_{\text{limit}}} \cdot \underbrace{\frac{N_{\text{trig}}^{\text{tagged}}(x)}{N_{\text{trig}}(x)}}_{\equiv 1/Y_{\text{btag}}} \leq 1 \tag{7.1}$$

where $N(x)$ is the number of events triggered with a reduced threshold setting x, N_0 is the number of events triggered with the standard trigger, N_{trig} is the number of triggered events at a given threshold setting and $N_{\text{trig}}^{\text{tagged}}$ is the number of triggered and b-tagged events at the same threshold setting. Therefore, Y_{limit} represents the increase of the number of triggered events due to the lowered threshold, while $1/Y_{\text{btag}}$ represents the decrease of the number of triggered events due to the additional b-tagging constraint. With Eq. 7.1 the first condition can be expressed as

$$Y_{\text{btag}} \geq Y_{\text{limit}} \tag{7.2}$$

Similarly, the second condition can be expressed as

$$\underbrace{\frac{\epsilon(x)}{\epsilon_0}}_{\equiv 1/X_{\text{limit}}} \cdot \underbrace{\frac{\epsilon_{\text{trig}}^{\text{tagged}}(x)}{\epsilon_{\text{trig}}(x)}}_{\equiv X_{\text{btag}}} > 1 \tag{7.3}$$

where the ϵ represent the corresponding efficiencies to trigger $t\bar{t}$ signal events. Likewise, $1/X_{\text{limit}}$ represents the increase in efficiency due to lowering the trigger threshold, while X_{btag} represents the reduction of efficiency due to the additional b-tagging constraint. With this, the second condition can be written as

$$X_{\text{btag}} \geq X_{\text{limit}} \tag{7.4}$$

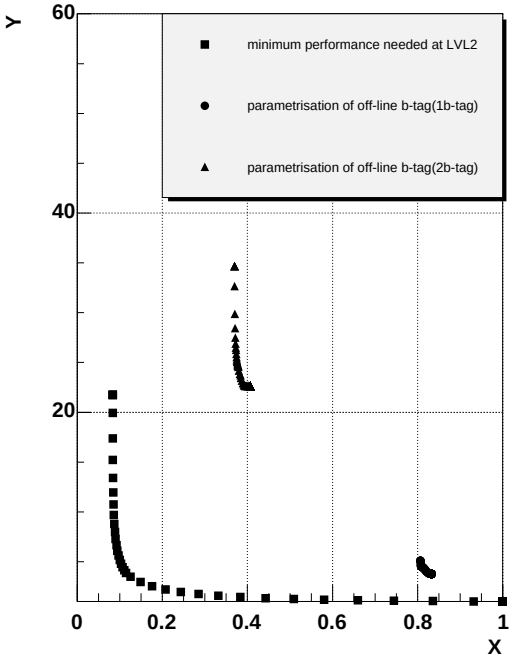

Figure 7.1: The minimal performance requirements for b-tagging in the level 2 trigger (squares) and the results for one (circles) and two (triangles) required b-tagged jets

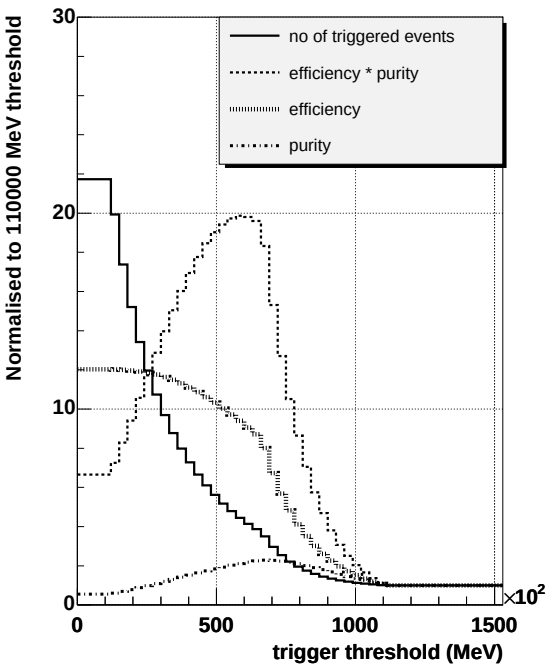

Figure 7.2: The effects of lowering the level 2 four jet trigger threshold on event rate, efficiency, purity and efficiency times purity. The shown values are normalised to the values obtained with the standard trigger conditions.

In FIG. 7.1 the pairs $(X_{\text{limit}}, Y_{\text{limit}})$ obtained for several threshold values of the four jet trigger are shown as squares. The curve built by these pairs gives the minimum requirement for the quality of the b-tagging. In order for the b-tagging procedure to meet the two conditions listed above, i. e. to fulfil EQ. 7.2 and EQ. 7.4, the pairs $(X_{\text{btag}}, Y_{\text{btag}})$ have to be above and right of the limiting curve.

The solid dots in FIG. 7.1 represent the $(X_{\text{btag}}, Y_{\text{btag}})$ pairs obtained by applying the offline b-tagging parametrisation described in SECT. 4.3 for different values of $|\eta|$ and p_T and demanding at least one positively tagged jet. They are grouped around a nearly constant efficiency reduction of $X_{\text{btag}} \simeq 0.8$. The Y_{btag} values vary stronger for different trigger thresholds. This can be understood as the lowering of the threshold alone increases the fraction of QCD light jet events in the triggered event sample. The lower the threshold is set, the higher the fraction

Event Sample	Generated Events	left after LVL1 Trigger		left after LVL2 Trigger		left after LVL2 + b-tag		left after lowered LVL2 + b-tag	
		Events	Eff.	Events	Eff.	Events	Eff.	Events	Eff.
H/A	40,000	12,957	32.4%	1,641	4.1%	662	1.7%	3,802	9.5%
$t\bar{t}$	1,000,000	163,821	16.4%	13,628	1.4%	5,125	0.51%	41,313	4.1%
QCD	1,000,000	56,277	5.6%	2,239	0.22%	72	0.0072%	242	0.024%

Table 7.1: The number of generated events in the three simulated data samples in comparison to the number of events passing the different four-jet-trigger conditions. The first two columns show the effects of the trigger conditions as they are now planned for ATLAS, the last two columns show how the introduction of a b-tagging criterium affects the outcome of the trigger.

of events with no b-tagged jet becomes, thus increasing the rejection rate.

The solid triangles in FIG. 7.1 represent the $(X_{\text{btag}}, Y_{\text{btag}})$ pairs obtained for several values for the trigger threshold when requiring at least two b-tagged jets. They cluster around an efficiency reduction of $X_{\text{btag}} \simeq 0.4$ with a stronger variation of Y_{btag} than in the case of one demanded b-tagged jet.

However, both groups of points are well right and above the limiting curve, indicating that the introduction of a b-tagging with a performance equivalent to the one discussed in SECT. 4.3 would improve the composition of the triggered event sample without compromising the rate of triggered events.

These findings indicate that the introduction of b-tagging into the trigger allows for the lowering of the trigger threshold. In FIG. 7.2 the effect of only lowering the threshold on the event rate, efficiency, purity and efficiency times purity is shown. The standard value for the four jet trigger condition at the moment is 110GeV. The quantities shown in FIG. 7.2 are expressed as multiples or fractions of their corresponding value at the standard threshold value. Therefore, above 110GeV all curves are flat lines at unity. For threshold values below 110GeV the event rate increases with lower threshold values. This is trivial as loosening an applied cut results in an larger or at least equal number of selected events. The behaviour of the event rate for very low threshold values is not to be considered realistic, as for low p_T jets the production of QCD light jets is dominating the event rate. QCD light jet events have been simulated for this analysis using a cut in the p_T of the initial hard interaction of 100GeV as discussed in SECT. 6.1. However, events with a softer initial hard interaction can only pass the four jet trigger with a threshold value of maximal 25GeV. As the level one trigger condition requires already four jets with at least 65GeV, this cut in the simulation is of no relevance

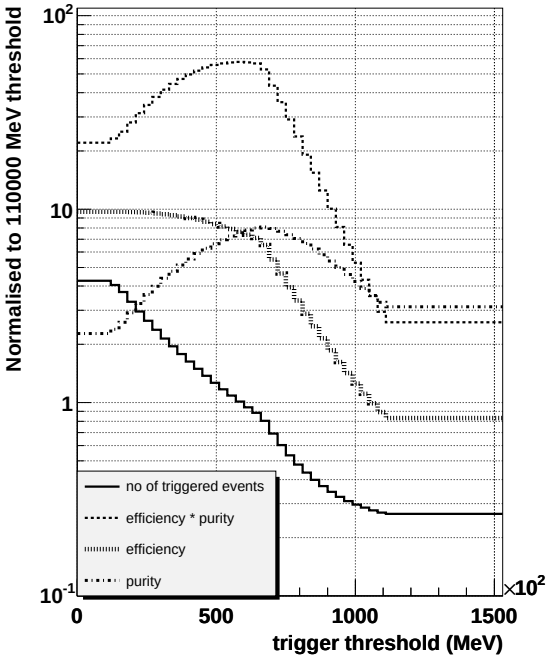

Figure 7.3: The effects of lowering the level 2 four jet trigger threshold and requiring at least one b-tagged jet on event rate, efficiency, purity and efficiency times purity. The shown values are normalised to the values obtained with the standard trigger conditions.

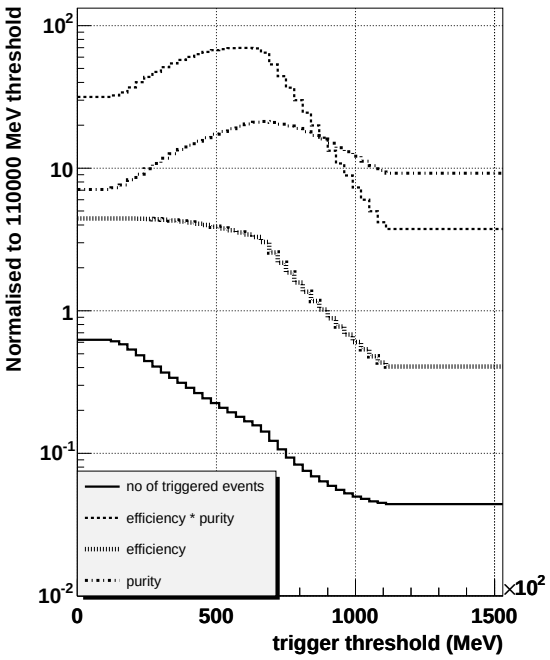

Figure 7.4: The effects of lowering the level 2 four jet trigger threshold and requiring at least two b-tagged jets on event rate, efficiency, purity and efficiency times purity. The shown values are normalised to the values obtained with the standard trigger conditions.

to this study.

For the same trivial reason as the event rate, the efficiency has to monotonously increase with decreasing threshold values. However, the efficiency increases first faster than the event rate and reaches a kind of saturation at low threshold values, where the event rate is still increasing. This behaviour is caused by the $t\bar{t}$ signal events being more likely to produce four jets with high tranverse momenta, while QCD light jet events are more likely to be produced with jets of lower transverse momenta. The saturation in the efficiency indicates that lowering the threshold below ~ 35GeV would not be meaningful.

Starting at high thresholds, the purity of the triggered event sample rises only

slowly with smaller threshold values due to the competing influences of rising efficiency and rising (especially background) event rate. Around 70GeV the purity shows a maximum of roughly two times the purity of the standard threshold setting and decreases again for lower threshold values.

While the introduction of an additional b-tagging criterium into the trigger condition is expected to reduce the efficiency, it is also expected to largely increase the purity of the triggered event sample. In FIG. 7.3 the event rate, efficiency, purity and the product of efficiency and purity is shown for the case that at least one positively b-tagged jet is required. Again, the values are normalised to the corresponding values obtained with the standard trigger condition. The effects of introducing b-tagging with an unchanged trigger threshold can therefore be observed in the flat lines above 110GeV. The b-tagging alone reduces the number of triggered events by a factor of four while the efficiency is reduced only by less than 20%. The purity of the triggered event sample is tripled due to the b-tagging.

All four quantities increase when the trigger threshold is lowered. The event rate reaches the same value as with the standard trigger threshold settings with a reduced threshold value of $\sim$ 60GeV. This implies that with the requirement of one b-tagged jet the threshold of the level 2 four jet trigger can be lowered down to the value of the level 1 four jet trigger threshold of 65GeV without compromising the event rate. The purity reaches a maximum of eight times the purity achieved with the standard trigger settings at a threshold value of $\sim$ 70GeV, the product of efficiency times purity is maximal around $\sim$ 65GeV with a value nearly sixty times the value of the standard settings. The efficiency itself is for the same threshold increased by a factor of $\sim$ 7.

In FIG. 7.4 the dependence of event rate, efficiency, purity and the product of efficiency and purity on the trigger threshold is shown for the case that at least two positively b-tagged jets are required. The general behaviour of the curves is similar to their behaviour in FIG. 7.3. However, the event rate is reduced much more by requiring two b-tagged jets than by requiring only one tagged jet and reaches for no lowered threshold the value of the standard trigger setting again. Of course, also here the cut on the initial hard interaction in the simulated QCD light jet event sample has to be taken into account, invalidating the results for trigger thresholds lower than 25 GeV. Purity reaches a maximal value roughly twenty times the value found with the standard trigger settings at a reduced threshold of $\sim$ 70GeV, efficiency times purity is maximal around a trigger threshold of $\sim$ 65GeV with a value $\sim$ 70 times the value found with the standard settings. The efficiency is for this setting of the trigger threshold increased by a factor of four, despite the additional b-tagging constraint.

The effects of all trigger conditions combined on the efficiency of the event selection is shown in TAB. 7.1. To estimate the efficiencies of the trigger conditions for the different event samples, 40,000 Higgs events with $m_H = 500\text{GeV}$ and 1,000,000 $t\bar{t}$- and light jet events have been used. Note, that TAB. 7.1 is only meant to show the effects of the trigger decisions on the different event types, the total numbers of triggered events do not reflect the proportions in which these event types will occur in the triggered event sample. In order to restore these proportions, the number of $t\bar{t}$ events would have to be multiplied by 8 and the number of QCD light jet events by 49,000.

The first two columns show the effect of all level 1 and the level 2 trigger conditions as they are at the moment planned for ATLAS. The next column displays the efficiencies which would be obtained when additionally to the level 2 trigger condition also a b-tagging for at least two jets would be required, while the last column shows the result of requiring the b-tagging and lowering the level 2 threshold value of the four jet trigger to its level 1 value. The number of H/A and $t\bar{t}$ events triggered with the level 2 trigger including the b-tag is only about a third of the number of such events triggered by the level 2 trigger only. However, the QCD light jet background is reduced substantially more. Using the reduced trigger rate for the light jet events to reduce the level 2 four jet trigger threshold to the value of the level 1 four jet trigger threshold, yields event rates for H/A and $t\bar{t}$ event about 2.5 times higher than with the standard level 2 trigger, while the number of triggered QCD light jet events is only a tenth of the number triggered with the standard level 2 trigger. Due to the large reduction of the light jet background, the total number of triggered events is still lower than the number of events triggered with the standard conditions, so the event rate constraint is not compromised by the lowered four jet trigger threshold.

All these findings support the implementation of a b-tagging criterium into the level 2 four jet trigger of ATLAS. Considering the huge background due to QCD light jet events and the large event rates at LHC, the purity of the triggered event sample surely appears to be the main concern of physics analyses. With this in mind the option to demand two positively b-tagged jets resulting in a twenty times increased purity of the event sample seems to be the requirement of choice.

7.2 Summary of the Example Analysis

In CHAP. 6 an analysis of simulated ATLAS data has been described. However, the simulation of the ATLAS detector used for this analysis did not contain any trigger mechanisms. Before discussing the impact of the trigger conditions on

this analysis in the next section, the most important points of this analysis are summarised here.

In the analysis presented in CHAP. 6 the sensitivity on the presence of a contribution due to the decay $H^0/A^0 \to t\bar{t} \to b\bar{b}qq\bar{q}\bar{q}$ to the spectrum of the invariant $t\bar{t}$ mass is studied. To this end pp collision events were simulated in which $t\bar{t}$ pairs were produced via gluon-gluon fusion. Additionally, an event sample in which $t\bar{t}$-pairs are produced via Higgs decays has been simulated. The first event sample alone represents the scenario of no Higgs contribution to the $t\bar{t}$-pair production, the combination of both samples represents the scenario of the presence of a Higgs contribution. However, an interference between both production processes occurs if a Higgs contribution is present. This interference is not taken into account in the Monte-Carlo simulation. Therefore, an event weighting procedure has been applied in order to introduce the interference into the combination of both event samples.

In these events jets were reconstructed using a cone algorithm. Only events with two positively b-tagged jets and at least four un-tagged jets were selected. The two b-tagged jets as well as the four un-tagged jets with the highest transverse momenta were assumed to be the decay products of the $t\bar{t}$ pair. For cross check reasons, the jets actually coming from the $t\bar{t}$ pair decay were identified using a parton-jet matching procedure. These jets were entered into a kinematic fit procedure which uses momentum and mass constraints in order to reconstruct the invariant mass of the assumed $t\bar{t}$ pair. For this, Gaussian errors of the jet parameters as well as corrections to systematic deviations of the jet parameters from the corresponding parameters of the quark which is assumed to have initiated the jet have been determined.

The main background to the fully hadronically decaying $t\bar{t}$ sample are QCD produced multi-jet events in which light jets are mis-tagged as b-jets. The reduction rate of this background due to the b-tagging is high. However, due to the large cross-section, a large amount of background events passes the b-tagging procedure. The amount of expected QCD light jet background events is too large to allow for the simulation of the full amount of events. Therefore, only a fraction of the expected events has been simulated with the intend to scale the results up with the necessary factor 1242.

In order to separate QCD light jet events from events which contain a $t\bar{t}$ pair, a Neural Network has been trained. Care has been taken, that the choice of input variables does not influence the spectrum of the reconstructed $t\bar{t}$ mass in the sample that is selected by a cut in the Neural Network output variable NN_{out}. Furthermore, the neural network input has been selected to ensure that

the neural network does not distinguish between QCD produced $t\bar{t}$ events and events in which the $t\bar{t}$-pair is produced in a Higgs decay. This is necessary in order to preserve the correct relative contributions of both $t\bar{t}$ production processes. A disturbed relation between QCD produced $t\bar{t}$-pairs and $t\bar{t}$-pairs from Higgs decays would later make the comparison of the mass spectrum with theoretical predictions of the combined spectrum of both production processes including their interference meaningless.

However, the cut in NN_{out} reduces the number of selected light jet events in a way that statistical errors become dominant in the mass distribution of these events. Therefore, the $t\bar{t}$ mass distribution of the selected light jet events has been fitted by a parametrisation to represent its shape. The parametrisation has been scaled up by the scaling factor and a random scatter representing statistical fluctuations of the counting rates has been superimposed on the parametrisation thus generating a pseudo data sample for the QCD light jet background.

The spectrum of the reconstructed $t\bar{t}$ masses has then been compared to theoretical predictions of this spectrum. A prediction for the spectrum without a contribution due to Higgs decays as well as a prediction including the contribution due to Higgs decays and the resulting interference are studied. The latter contains the mass of the Higgs boson as a free parameter. In order to apply the prediction of the process $gg \to t\bar{t}$ to the experimental case of $pp \to t\bar{t} + X$, a PDF-like correction has been multiplied to the prediction. Further, before comparing the prediction to the reconstructed simulation events, the prediction has been corrected for the effects of experimental mis-reconstruction of the $t\bar{t}$-mass using a matrix correction method.

Both, the full simulated data sample as well as the simulated data sample without $t\bar{t}$ production due to Higgs decays are then compared to both possible variations of the theoretical prediction. While the presence of a Higgs contribution could be clearly recognised with a χ^2-test and an estimate of the simulated Higgs mass could be derived from this, the tests on the data sample without a Higgs contribution allowed for the exclusion of this contribution up to masses of 850GeV.

7.3 Influence of the Trigger on the Sample Analysis

In this section the impact of the trigger conditions on the outcome of the sample analysis are discussed. As already discussed in Sect. 7.1, lowering the four jet trigger threshold of the level 2 trigger to its value of the level one trigger with

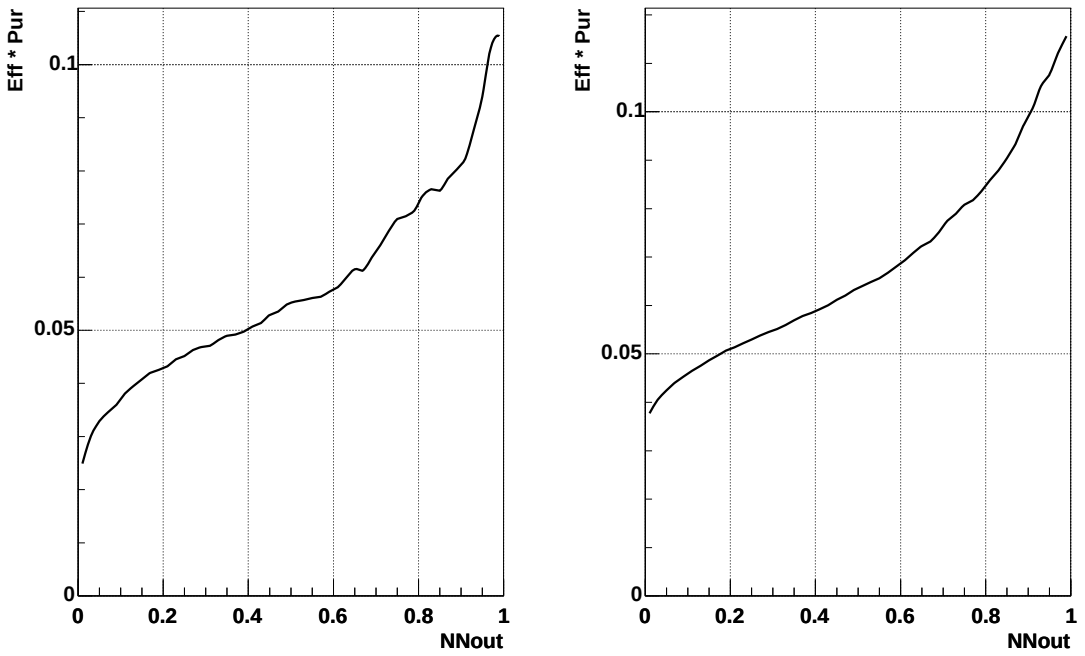

Figure 7.5: The product of efficiency and purity for the selection of $t\bar{t}$-events as a function of the cut in NN_{out} for events passing the standard level 2 trigger conditions (left) and events passing the level 2 trigger conditions with the reduced four jet trigger threshold (right)

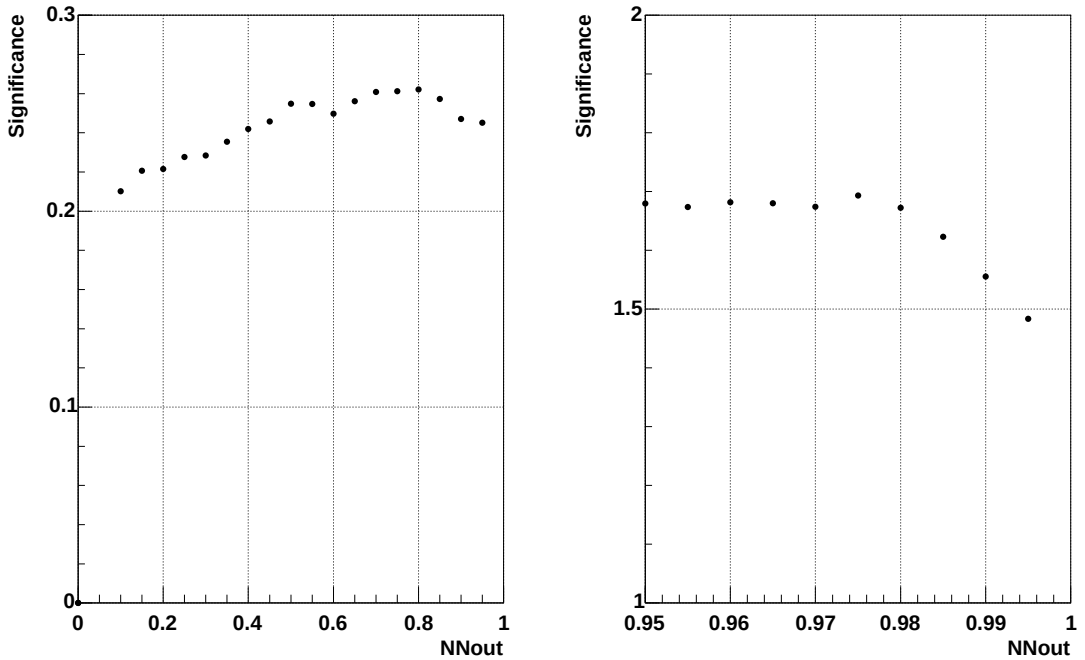

Figure 7.6: The significance of the number of of $H/A \to t\bar{t}$-events selected by a cut in NN_{out} as a function of the cut-variable for events passing the standard level 2 trigger conditions (left) and events passing the level 2 trigger conditions with the reduced four jet trigger threshold (right)

Evt. Sample	Events	LVL2 + KINFIT	after NN-cut	red. LVL2 + b-tag + KINFIT	after NN-cut
H/A	40,000	347	265	3143	1572
$t\bar{t}$	$7.928 \cdot 10^6$	29,375	24,289	295,264	146,519
QCD l. j.	$4.970 \cdot 10^{10}$	$1.113 \cdot 10^6$	233,571	$7.483 \cdot 10^6$	487,020
Sig/Bkg	$1.6 \cdot 10^{-4}$	$2.67 \cdot 10^{-2}$	$1.05 \cdot 10^{-1}$	$3.99 \cdot 10^{-2}$	$3.04 \cdot 10^{-1}$

Table 7.2: The number of events in the different event samples in comparison with the number of events that pass the level 2 trigger condition and the KINFIT procedure and those that also pass an cut in the neural network output for the present level two trigger menu as well as for the trigger menu with the reduced level 2 four jet threshold

the simultaneous implementation of a b-tagging procedure requiring at least two positively tagged jets into the level 2 trigger is expected to improve the data sample to be analysed. Therefore in this section the outcome of the analysis with the standard trigger conditions as they are at the moment forseen to be implemented into the ATLAS experiment will be compared to the outcome of the analysis of a data sample that has been triggered with the four jet trigger threshold of the level 2 trigger set to 65GeV and an additional b-tagging procedure with the properties described in Sect. 4.3. All other trigger conditions remain unchanged.

As the properties of the triggered event samples vary from the general event sample studied in Chap. 6, the most efficient cut value for the neural network output variable NN_{out} has to be determined anew for these samples. The training of neural networks dedicated to these event sample turned out not to be practical due to the insufficient number of events passing the trigger conditions. However, another neural network has been trained on the event sample which passed the level 1 trigger conditions as a cross-check. The properties of this newly trained network do not differ from those of the neural network trained on the general event sample as described in Sect. 6.3.2. It seems therefore save to assume that this neural network can also be applied on the event samples studied here.

Fig. 7.5 shows the product of efficiency and purity of the $t\bar{t}$-event selection as a function of the cut in NN_{out}. The left plot shows the curve for the data sample passing the standard level 2 trigger conditions, while the right plot shows the curve for the events passing the level two trigger with the reduced four jet trigger threshold. Both curves are monotonously rising with NN_{out} except for statistical fluctuations in the plot for the standard level 2 trigger. This again suggests to choose a cut value as high as reasonably possible. However, the actually used cut

value is again determined by maximising the expected significance of the Higgs contribution as defined in Eq. 6.15. In Fig. 7.6 the significance of the selected events with H/A decays is shown in dependence on the cut in NN_{out}. The left plot shows the significance for the event sample selected with the standard level 2 trigger conditions, the right plot the significance achieved using the reduced four jet trigger threshold. The significance has been calculated as described in Sect. 6.3.5, but the mass-range around the Higgs mass peak which is taken into consideration is adjusted to the shape of the peak obtained with the corresponding trigger condition. For the distributions obtained using the default level 2 trigger, all the histogramed mass range has been used to determine the significance, as no distinctive peak can be seen in the corresponding sample of triggered Higgs events, while for the distributions obtained using the lowered level two trigger threshold the mass range from 425GeV to 575GeV has been considered. The expected significance using the standard level 2 trigger conditions in only of the order of ~ 0.25, while the lowered four jet trigger threshold yields a significance around 1.7, nearly seven times larger. In order to maximise the significance of the expected Higgs contribution, a cut in NN_{out} at 0.8 is chosen for the event sample obtained with the standard level 2 trigger and a cut at 0.975 for the event sample obtained with the lowered four jet trigger threshold.

Tab. 7.2 shows the number of events for the different event types, that are left after passing the various level 2 trigger conditions and the KINFIT procedure in comparison with the number of events that are left after applying additionally a cut in NN_{out}. These numbers have to be compared to the numbers given in Tab. 6.2 for the analysis on the data sample not requiring the trigger. Applying the standard level 2 trigger the signal to background ratio is improved by a factor four in comparison with the results from Tab. 6.2 after the reconstruction procedure. However, the improvement in this ratio due to the cut in NN_{out} is only of a factor five, leading to a smaller signal to background ratio after the NN_{out}-cut here than in Tab. 6.2. The events rejected by the cut in NN_{out} in Tab. 6.2 overlap widely with the events here already rejected by the trigger conditions. However, the trigger condition rejects a larger amount of the signal events than the neural network cut would do, leading to this smaller signal to background ratio. The total number of selected signal events is reduced by more than a factor ten for Higgs events and by a factor twenty for QCD produced $t\bar{t}$-events when compared to the event numbers in Tab. 6.2.

Applying the level 2 trigger conditions with the reduced four jet threshold and the implemented b-tagging, the signal to background ratio is nearly restored to the value found in Tab. 6.2, while the total number of accepted signal events is only reduced by a factor two to three.

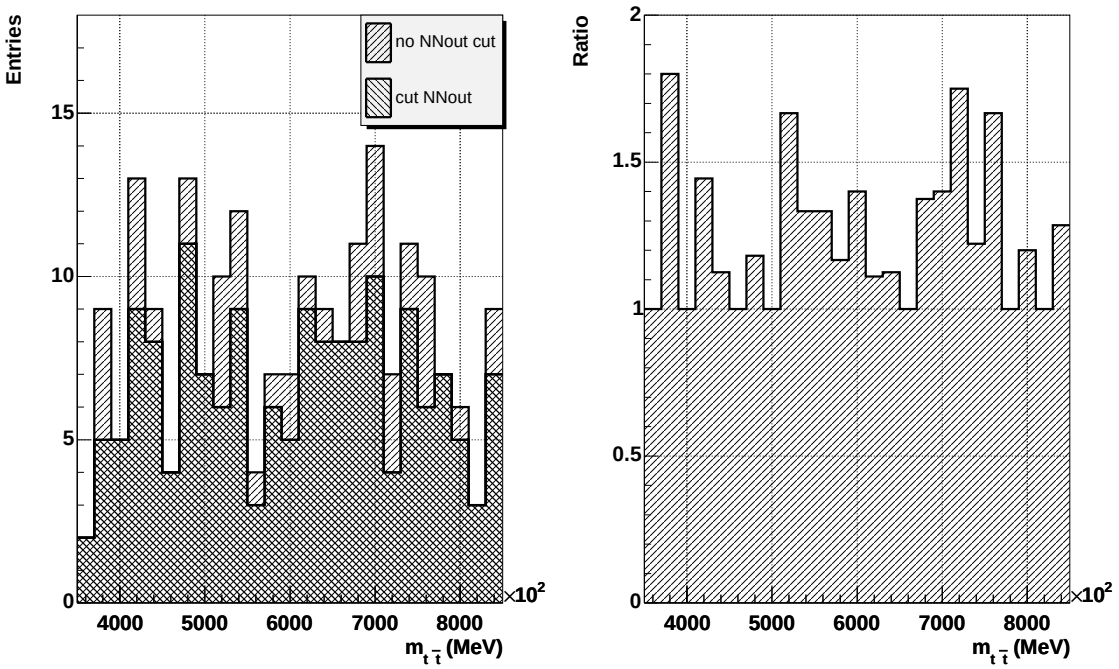

Figure 7.7: The $t\bar{t}$-mass distribution of the H/A sample after all default level 2 trigger conditions have been applied. The upper histogram shows the distribution before, the lower after applying a cut in the neural network output. The right plot shows the ratio of the two histograms.

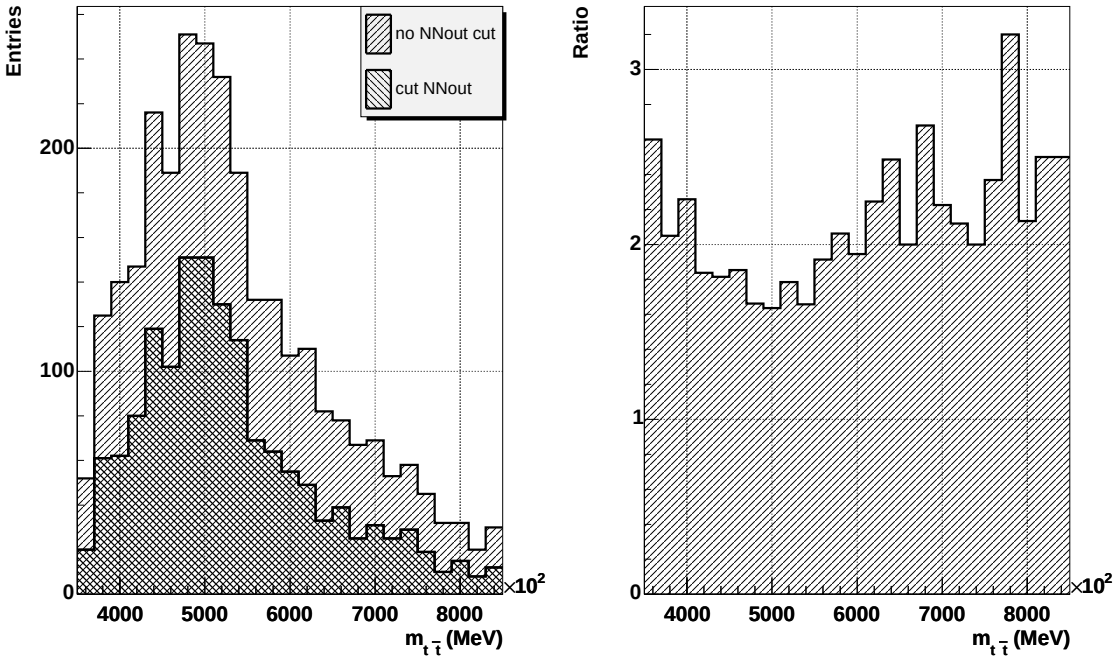

Figure 7.8: The $t\bar{t}$-mass distribution of the H/A sample after all level 2 trigger conditions with the reduced four jet trigger threshold have been applied. The upper histogram shows the distribution before, the lower after applying a cut in the neural network output. The right plot shows the ratio of the two histograms.

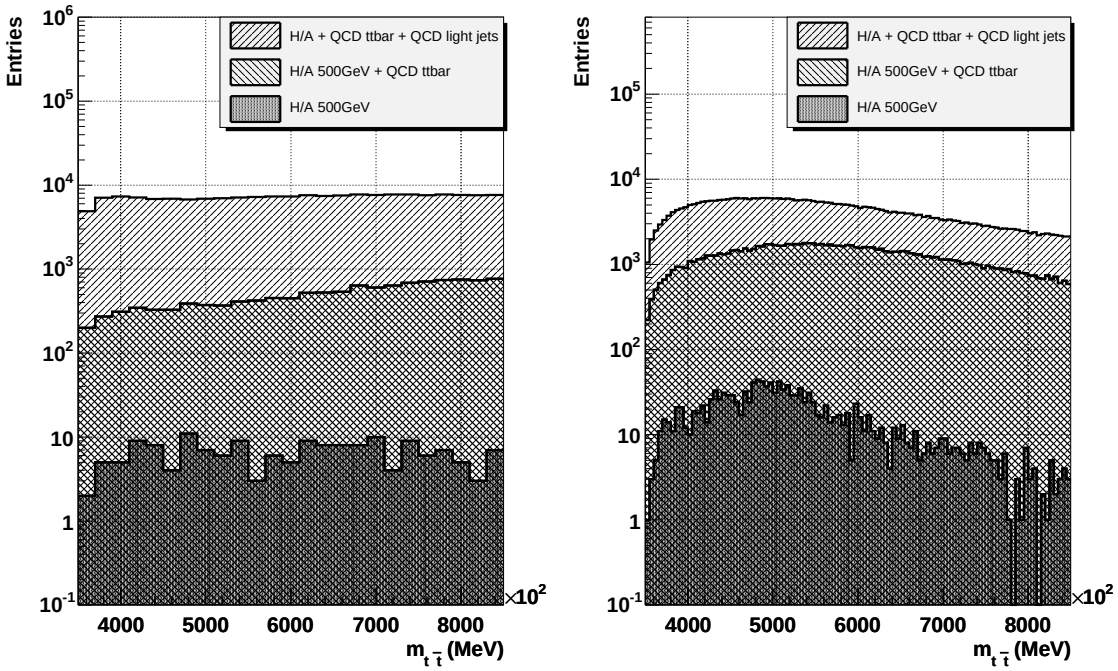

Figure 7.9: The $t\bar{t}$-mass spectrum of the events which meet the standard level 2 trigger conditions (left) and the level 2 trigger conditions with the reduced four jet trigger threshold (right). The events additionally passed a cut in NN_{out}. The contributions of the different event samples to the mass spectrum are indicated.

In FIG. 7.7 the impact of the standard trigger conditions and the cut in NN_{out} on the mass distribution of the H/A data sample is shown. In the left plot the mass distribution before and after the cut in NN_{out} is shown. Both mass distributions have only few entries and are nearly flat, a distinguished peak cannot be recognised. The difference between the two distributions is minimal, the cut in NN_{out} does not remove significantly more events after the standard level 2 trigger conditions are applied. The right plot shows the ratio between the two distributions in the left plot for clarity.

FIG. 7.8 shows the same plots for the event sample obtained with the reduced four-jet trigger threshold. Not only is the event sample entering the distribution in the left plot much larger than the one in FIG. 7.7, also the distinctive shape of the mass peak is preserved here. The cut in NN_{out} removes a larger fraction of the events than in FIG. 7.7, but even in the distribution of the events passing this cut the mass peak is still clearly visible. The right plot in FIG. 7.8 shows again the ratio of the two distributions in the left plot for clarity.

In FIG. 7.9 the composition of the $t\bar{t}$-mass spectrum is shown for the events accepted by the cut in NN_{out}. The left plot shows the spectrum for the events triggered by the standard level 2 conditions, the right plot shows the result obtained with the reduced four jet trigger threshold. The shape of the overall spectrum in the left plot is changed due to the influence of the trigger conditions. Instead of slowly declining after a maximum around 400GeV as in FIG. 6.52, the spectrum first rises, but then stays high and even increases. Using the reduced four jet trigger threshold, the shape of the spectrum is closer to the one shown in FIG. 6.52. The improved signal to background ratio can be recognised in the right plot of FIG. 7.9.

Now the analysis steps described in SECT. 6.4 are applied to the data samples obtained with the two variations of the level 2 trigger conditions. FIG. 7.10 shows the data sample triggered with the standard level 2 trigger conditions without a Higgs contribution in comparison with both theoretical predictions. The pulls of the simulated data with respect to the predictions are again shown in the right plot of FIG. 7.10. In FIG. 7.11 the same plots for the data sample with a Higgs contribution are shown. The distorted, bent upwards shape of the mass spectrum can be clearly recognised in the linear plots. The general description of the data by both predictions is good, the pull values generally vary between -2 and 2. No clear difference between the pulls of the two hypothesis can be seen.

Applying the χ^2-test to these data samples leads to the values shown in FIG. 7.14 for the hypothesis. The left plot shows the results obtained from the data sample without a Higgs contribution, the right plot the results for the sample with the Higgs contribution. Both χ^2-functions are nearly constant around 84 without any distinctive feature. The corresponding χ^2-values for the antithesis are 82.8 for the data sample without a Higgs contribution and 83.5 for the data sample with a Higgs contribution. Again, all χ^2-values refer to 100 degrees of freedom. These values indicate no distinction between the different data sets and the different hypotheses. Therefore, neither an indication of the presence of a Higgs contribution nor exclusion limits for such a contribution could be derived from this data.

In FIG. 7.12 and FIG. 7.13 the comparison of the data sample triggered with the lowered level 2 four jet trigger threshold with the two theoretical predictions is shown, in FIG. 7.12 for the data sample without, in FIG. 7.13 for the data sample with a Higgs contribution. The mass distribution is more similar to the distributions shown in FIG. 6.73 and FIG. 6.74 for the data samples without trigger conditions, showing a clear maximum. However, the maximum is wider than in FIG. 6.73 and FIG. 6.74 and shifted to higher masses. The right plots in FIG. 7.12 and FIG. 7.13 again show the pull values of the data with respect to the different predictions. Again, the pull values vary only between -2 and 2 indicating

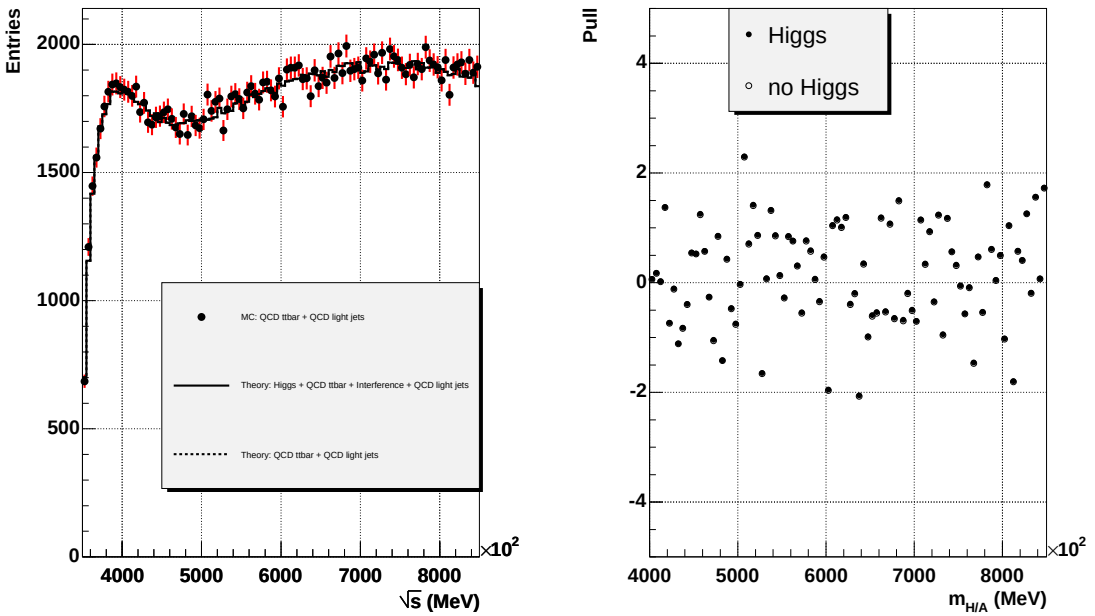

Figure 7.10: The $t\bar{t}$-mass distribution of the data sample without a Higgs contribution in comparison with the theoretical predictions for this distribution with and without a Higgs contribution. The events passed the standard level 2 trigger conditions and a cut in NN_{out}. The right plot shows the pull of the simulated data with respect to the theoretical predictions with solid dots for the hypothesis and with open dots for the antithesis.

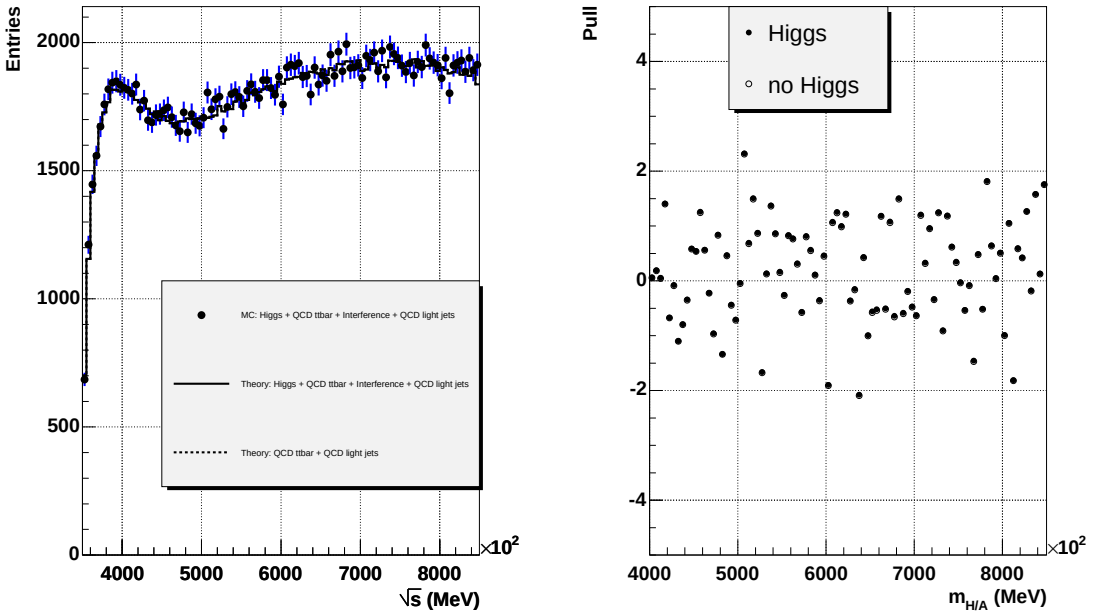

Figure 7.11: The $t\bar{t}$-mass distribution of the data sample with a Higgs contribution in comparison with the theoretical predictions for this distribution with and without a Higgs contribution. The events passed the standard level 2 trigger conditions and a cut in NN_{out}. The right plot shows the pull of the simulated data with respect to the theoretical predictions with solid dots for the hypothesis and with open dots for the antithesis.

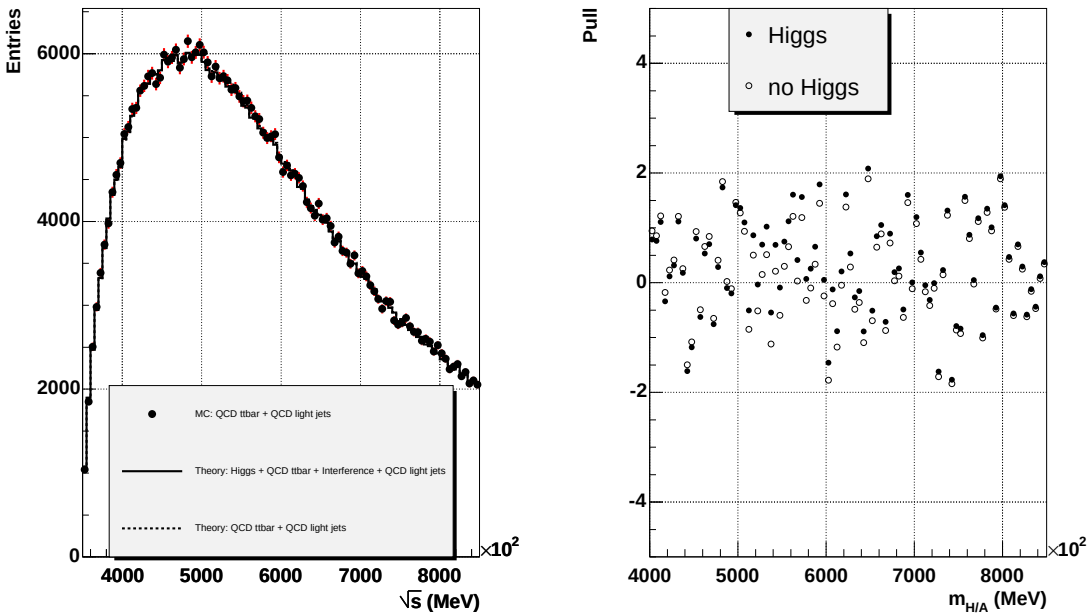

Figure 7.12: The $t\bar{t}$-mass distribution of the data sample without a Higgs contribution in comparison with the theoretical predictions for this distribution with and without a Higgs contribution. The events passed the level 2 trigger conditions with a lowered four jet trigger threshold and a cut in NN_{out}. The right plot shows the pull of the simulated data with respect to the theoretical predictions with solid dots for the hypothesis and with open dots for the antithesis.

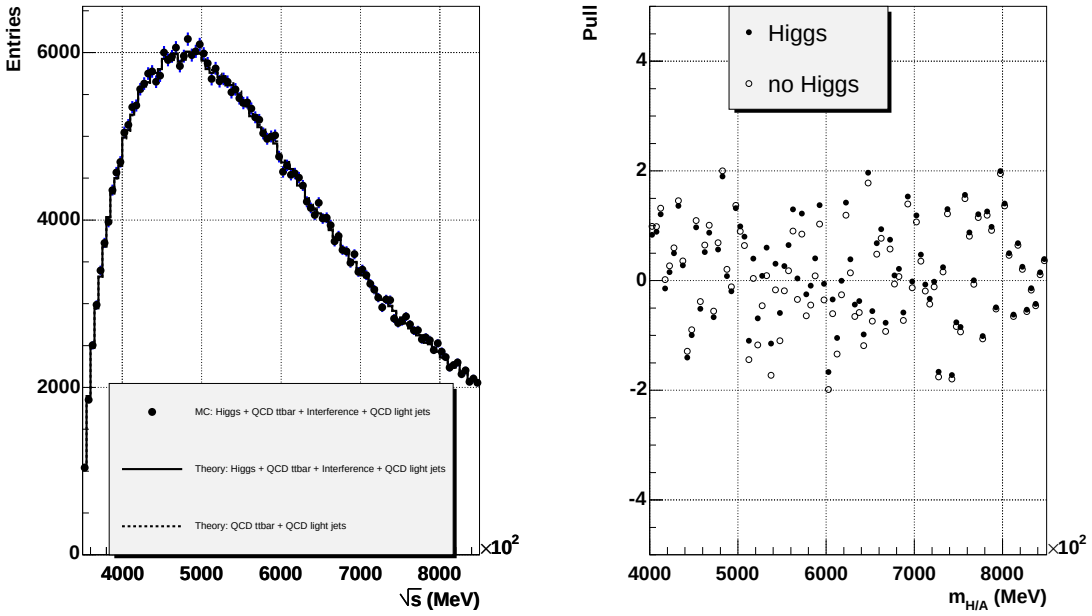

Figure 7.13: The $t\bar{t}$-mass distribution of the data sample with a Higgs contribution in comparison with the theoretical predictions for this distribution with and without a Higgs contribution. The events passed the level 2 trigger conditions with a lowered four jet trigger threshold and a cut in NN_{out}. The right plot shows the pull of the simulated data with respect to the theoretical predictions with solid dots for the hypothesis and with open dots for the antithesis.

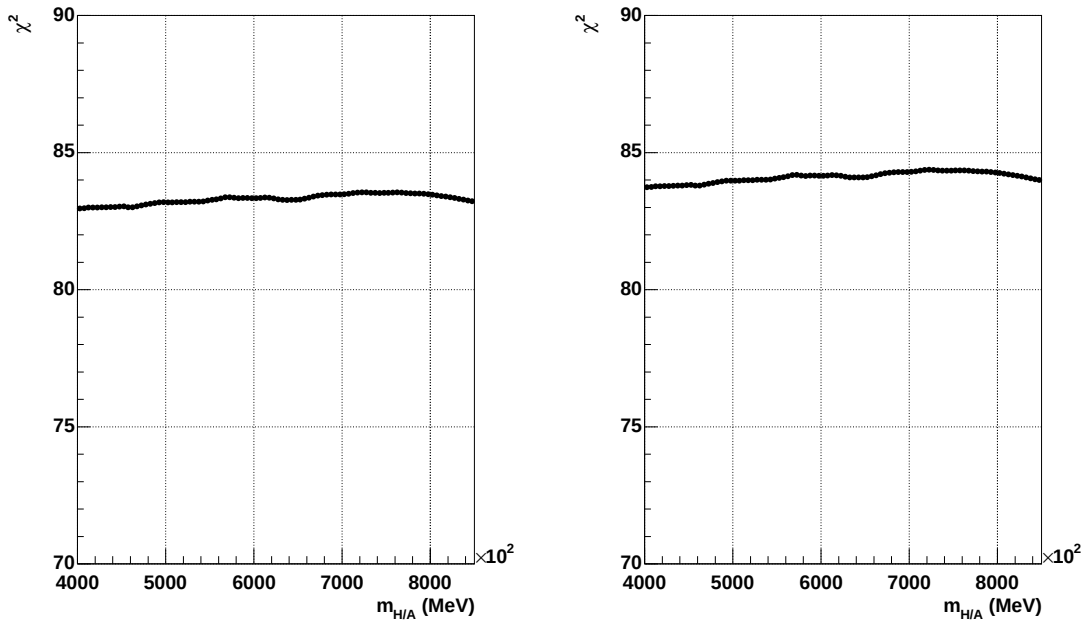

Figure 7.14: The χ^2-values obtained from the comparison of the hypothesis to the data sample without a Higgs contribution (left) and with a Higgs contribution (right). The events passed the standard level 2 trigger conditions and a cut in NN_{out}.

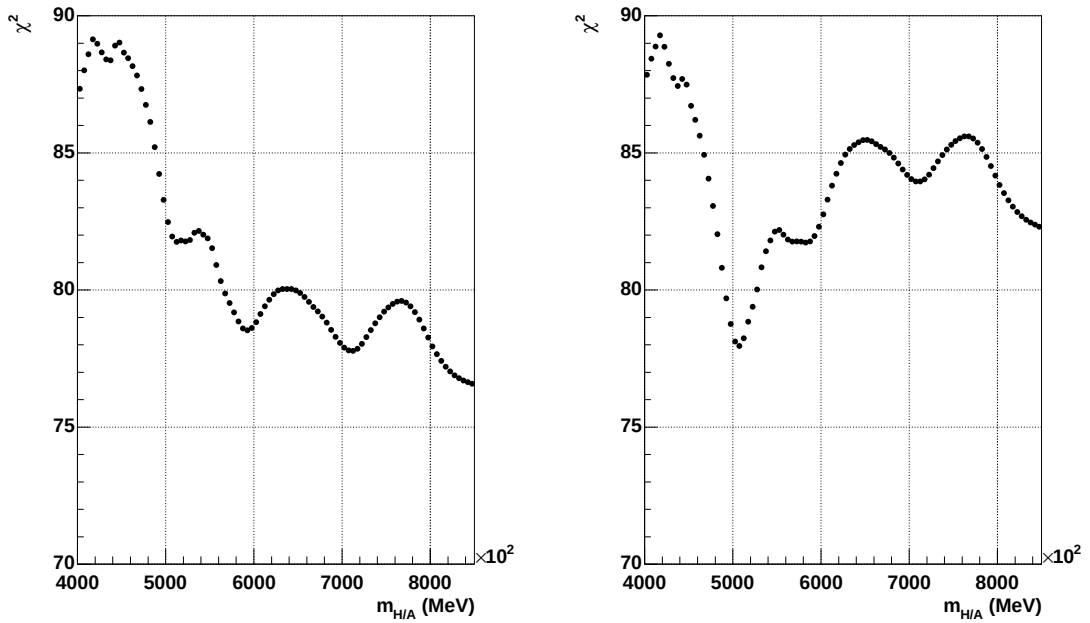

Figure 7.15: The χ^2-values obtained from the comparison of the hypothesis to the data sample without a Higgs contribution (left) and with a Higgs contribution (right). The events passed the level 2 trigger conditions with the lowered four jet trigger threshold and a cut in NN_{out}.

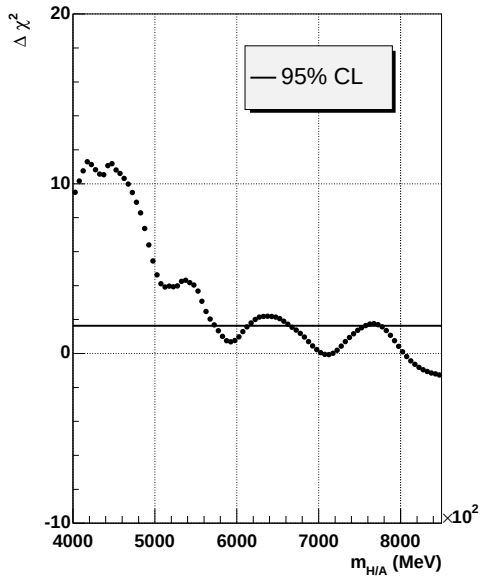

Figure 7.16: The $\Delta\chi^2$-values obtained using tagged jets as input to the analysis. The solid horizontal line indicates $\Delta\chi^2 = 1.64$.

a good agreement between the data sets and both predictions. However, unlike for the samples triggered with the standard level 2 trigger conditions, the pull values for the different predictions are distinguishable.

In FIG. 7.15 the corresponding χ^2-values with respect to the hypothesis that a Higgs contribution is present are shown. The left plot shows the values obtained with the data sample without a Higgs contribution, the χ^2-values are around 85 to 90 for small invariant masses and drop rapidly for larger masses. The corresponding χ^2-value with respect to the antithesis is 77.8.

The right plot of FIG. 7.15 shows the χ^2 values obtained when comparing the data sample with a Higgs contribution to the hypothesis that this contribution is present. Here, a small dip around $m_H = 500$ GeV can be seen. It becomes more pronounced by the χ^2-curve rising right of the dip to higher values than the corresponding values in the left plot. This is caused by the depletion of events at masses larger than the Higgs mass due to the interference. This depletion increases the difference between the mass peak of the hypothesis and the data, leading to the increase in χ^2. The χ^2 value in the minimum is 78.0, while the χ^2 value with respect to the antithesis is 82.2.

In FIG. 7.16 the $\Delta\chi^2$ values obtained from the χ^2-values shown in the left plot of FIG. 7.15 are shown. Over a large part of the studied mass range they stay above 1.64. A contribution to the $t\bar{t}$-mass spectrum due to Higgs decay could therefore be excluded up to a Higgs mass of $\sim$ 560GeV.

The exclusion limit for a Higgs contribution to the mass spectrum depends to some extent on the statistical fluctuations within the dominant background distribution of QCD light jet events. In order to estimate the influence of these fluctuations on the achievable mass limit, ten different randomly scattered mass distributions have been generated with the method described in SECT. 6.3.4. The top left plot of FIG. 7.17 shows the χ^2-values obtained when the full data sample including QCD light jet background, QCD produced $t\bar{t}$-events and Higgs decaying into $t\bar{t}$ is compared to the theoretical prediction of the hypothesis (that a Higgs contribution to the spectrum is present) for each of the ten produced QCD light jet backgrounds. The absolute values of the χ^2-values vary between $\sim$ 65 and $\sim$ 105. This variation is in good agreement with the expected standard deviation for χ^2, which is $\sqrt{2N_{dof}} \simeq 14.1$. However, at least eight of the ten χ^2-curves in this plot show the characteristic dip at 500GeV indicating the presence of the contribution due to a Higgs boson with a mass of 500GeV.

The top right plot of FIG. 7.17 shows the χ^2 values obtained when the hypothesis is compared to a data sample which includes no Higgs contribution, but consists only of QCD light jet events and QCD produced $t\bar{t}$-events for each of the ten generated light jet distributions. The scatter of the absolute χ^2-values is similar to the scatter observed in the top left plot of FIG. 7.17. All curves show some general declining tendency with increasing masses with some fluctuations, but no distinctive features that would suggest the presence of a Higgs contribution. From these χ^2-curves and the corresponding χ^2-values obtained when comparing the mass distributions of these data samples to the antithesis (that no Higgs contribution is present), the $\Delta\chi^2$ values as defined in EQ. 6.21 can be calculated. The average of these $\Delta\chi^2$-values obtained with the ten different light jet backgrounds is shown as a function of the Higgs mass assumed in the hypothesis in the lower left plot of FIG. 7.17. The curve falls steeply with increasing Higgs mass and crosses the critical value of 1.64 at roughly 800GeV. However, the last increase and drop of before this is rather a statistical fluctuation. Extrapolating the descent of the curve a crossing of 1.64 is expected around 720GeV. This limit, based on a larger sample of generated background represents a more reliable estimate of the exclusion limit to be expected.

A significant improvement of the data sample has been reached by lowering the four jet trigger threshold and requiring b-tagging in the trigger condition of the level 2 trigger. If, an experimental confirmation or exclusion of a Higgs contri-

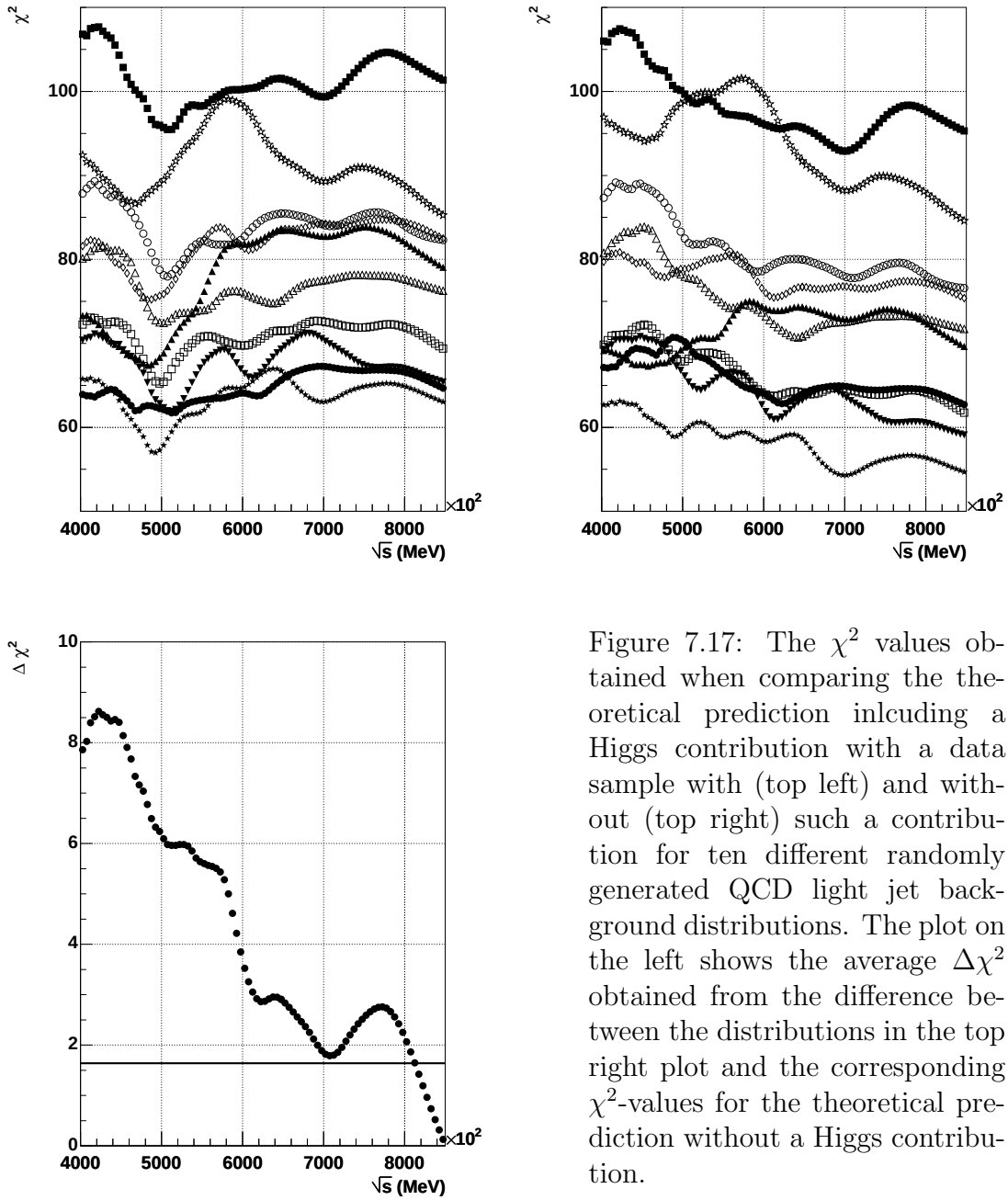

Figure 7.17: The χ^2 values obtained when comparing the theoretical prediction inlcuding a Higgs contribution with a data sample with (top left) and without (top right) such a contribution for ten different randomly generated QCD light jet background distributions. The plot on the left shows the average $\Delta\chi^2$ obtained from the difference between the distributions in the top right plot and the corresponding χ^2-values for the theoretical prediction without a Higgs contribution.

bution to the mass spectrum of fully hadronically decaying $t\bar{t}$-pairs is tried to be achieved with the ATLAS data, the modification of the level 2 trigger condition is highly recommended.

Chapter 8

Summary

In this thesis a pre-study to an analysis of data recorded by the ATLAS event has been presented. The scope of this analysis is the search for heavy super-symmetric Higgs bosons H/A in the decay channel $H/A \to t\bar{t} \to qq\bar{q}\bar{q}b\bar{b}$. Special consideration has been paid to the prospects of improving the analysis by introducing a b-tagging criterium to the level 2 trigger system of ATLAS.

Three event samples have been simulated and processed with the fast detector simulation ATLFAST. The event samples for QCD produced $t\bar{t}$-events and for $t\bar{t}$-pair production via H/A-decays have been simulated corresponding to an integrated luminosity of $\mathcal{L} = 35.8\text{fb}^{-1}$, which is the luminosity expected after one year of data taking at medium luminosity.

In order to reconstruct the invariant mass of the $t\bar{t}$-pairs, a kinematic fit procedure has been set up and a neural network has been trained to separate the QCD light jet events from the events that contain $t\bar{t}$-decays. The obtained mass-spectra have then been compared to theoretical predictions of these distributions. In order to adjust the predictions, which are calculated for the process $gg \to t\bar{t}$, to the $t\bar{t}$-production in proton-proton collisions, effective PDFs have been devised. Inefficiencies of the reconstruction procedure have been added to the predictions using a matrix correction technique.

The comparison of these predictions with the simulated data sample which did not undergo the triggering process allowed for the postulation of exclusion limits for the presence of a Higgs contribution to the mass spectrum. For an ideal jet identification, the absence of a Higgs contribution could be discovered over the whole studied mass range with an 95% confidence limit. The exclusion limit drops to 850 GeV using a realistic jet identification.

The presence of a Higgs contribution to the mass spectrum was found to produce a distinctive pattern in the χ^2 values as a function of the Higgs mass assumed in the theoretical prediction. A clear dip in the χ^2-values at the mass of the simulated Higgs boson could be observed for the case of an ideal jet identification. The pattern eroded to some degree when a realistic jet identification is used, but generally persisted.

Studies of the impact of the introduction of a b-tagging criterium into the ATLAS level 2 trigger menu on the triggered data sample showed that a b-tagging criterium with properties as they are at the moment assumed for the offline b-tagging would allow to lower the level 2 four jet trigger threshold to its level 1 value without compromising the event rate. This would significantly improve the triggered event sample, increasing the reduction rate of QCD light jet events by a factor ten and the efficiency to trigger $t\bar{t}$-events by a factor two to four.

The analysis has been applied to the data samples triggered with the standard level 2 trigger conditions and the trigger conditions improved by b-tagging and a lower threshold. In case of the standard level 2 four jets trigger, an exclusion limit for the presence of a Higgs contribution to the $t\bar{t}$-mass spectrum could not be given. Furthermore, no distinctive local minimum in the χ^2-values as function of the assumed Higgs mass could be found when analysing a data sample with such a contribution. In contrast, the sample selected with the improved level 2 trigger criteria allowed for an exclusion of a Higgs contribution to the measured mass spectrum up to 720 GeV. Moreover, a clear local minimum at the correct mass could be restored in the $\chi^2(m_{\text{Higgs}})$ curve for simulated H/A bosons of 500 GeV mass. The modification of the trigger condition by reducing the four-jet trigger threshold from 110 GeV to 65 GeV with the simultaneous introduction of a b-tagging procedure into the level two trigger seems therefore to be strongly recommended.

The findings of this analysis indicate that fully hadronic $t\bar{t}$ events can be used in the search for MSSM Higgs bosons and that a resonance signal can be identified in this channel, if it is complemented by an interference pattern.

Acknowledgements

I would like to take this opportunity to express my utmost gratitude to at least some of the many people who lent me their support in completing this thesis, in the hope not to forget too many of them.

First and foremost, I would like to thank my supervisor Prof. Dr. Peter Mättig. His support guided me throughout the whole process, providing valuable input and constant motivation.

In the same way I want to thank Dr. Klaus Hamacher. His inimitable humour, frankness and personal warmth as well as his amazing physical intuition and experience guided me past so many obstacles in the time I worked on this thesis.

Also, I am deeply indebted to many of my colleagues of the Wuppertal ATLAS team. Especially Dr. Grant Gorfine and Dr. Andreas Kootz, who helped me with unparalled patience when I stumbled over the rocks in the field of programming and provided invaluable additional physical insights. Dr. Yvonne Peters did not only cope with my moods, but created also a wonderful working atmosphere with her inexhaustible cheerfulness spiced with only minute traces of sarcasm in the office I shared with her.

Of all the helpful and unbelievably friendly colleagues in our research group I would like to say special thanks to Dr. Daniel Wicke, Dr. Jenny Böhme, Dr. Christian Schmidt and Dr. Torsten Harenberg, to name only a few of all the colleagues who together formed a team with a uniquely pleasant atmosphere.

My very special thanks I would like to give to my parents for their constant love, support, understanding and dedication which made it possible for me to follow the path I chose and to achieve the things I aimed for. Without them, none of this would ever have been possible. I also would like to thank my mother-in-law who was a great friend and mother while staying in a foreign country.

Last but not the least I want to thank my husband Martin who, with his great patience, support and great knowledge of physics helped, guided and kicked me when no light in the tunnel was seen and stood up to my very many moods during the pregnancies with our two wonderful sons. He spent so many hours in helping to find answers to the questions I had during my work and kept my head up

whenever necessary.

Bibliography

[1] Super-Kamiokande Kollaboration: Y. Fukuda u. a.,
Evidence for oscillation of atmospheric neutrinos,
Phys. Rev. Lett. **81** (1998) 1562;

[2] *A Combination of Preliminary LEP Electroweak Measurements and Constraints of the Standard Model*
ALEPH, DELPHI, L3 and OPAL Collaborations,
CERN-PPE-95-172, Nov 1995,
Contributed to the 1995 Europhysics Conference on High Energy Physics EPS-HEP, Brussels, Belgium, 27 Jul-2 Aug 1995 and to the 17th International Symposium on Lepton-Photon Interactions, Beijing, China, 10-15 Aug 1995;

[3] D.Griffiths,
Introduction to Elementary Particles,
Jonh Wiley & Sons, New York 1987;

F. Halzen and A. D. Martin,
Quarks & Leptons,
John Wiley & Sons, New York 1984;

M. E. Peskin und D. V. Schroeder,
An introduction to quantum field theory,
Addison-Wesley Publishing Company, New York 1995;

M. Kaku,
Quantum field theory,
Oxford University Press, Oxford 1993;

[4] Shi-Lin Zhu, Departament of Physics, Peking University,
BEIJING 100871, CHINA (Dated: August 22, 2006),

arXiv:hep-ph/0406204 v1 18 Jun 2004;

[5] R. K. Ellis, W. J. Stirling und B. R. Webber,
QCD and Collider Physics,
Cambridge University Press, Cambridge 1996;

[6] Yu.L.Dokshitzer, V.A.Khoze, A.H.M"uller & S.I.Troyan,
Basics of perturbative QCD,
Editions Frontiéres, Gif-sur-Yvette Cedex 1991;

[7] P. W. Higgs,
Broken symmetries, massless particles and gauge fields,
Phys. Lett. **12** (1964);
Broken symmetries and the masses of gauge bosons,
Phys. Rev. Lett. **13** (1964);

[8] S. L. Glashow, J. Illipoulos und L. Maiani,
Weak interactions with Lepton-Hadron symmetry,
Phys. Rev. **D2** (1970) 1285;

[9] N. Cabibbo, Phys. Rev. Lett. **10** (1963) 531;
M. Kobayashi and K. Maskava, Prog. Theor. Phys. **49** (1973) 652;

[10] S. L. Glashow,
Partial symmetries of weak interactions,
Nucl. Phys. **22** (1961) 579;
S. Weinberg,
A model of leptons,
Phys. Rev. Lett. **19** (1967) 1264,
Effects of a neutral intermediate boson in semileptonic processes,
Phys. Rev. **D5** (1972) 1412;

[11] The LEP Working Group for Higgs Boson Searches,
Search for the Standard Model Higgs Boson at LEP, ALEPH, DELPHI, L3 and OPAL Collaborations,
CERN-EP/2003-011, April 25, 2003;

[12] N. Ellis,
Supersymmetry for Alp Hikers
in Proceedings of the 2001 European School of High-Energy Physics, Beatenberg, Switzerland;
CERN Yellow Book 2002-002;

[13] J. Ellis,
Beyond the Standard Model for Hillwalkers
in Proceedings of the 1998 European School of High-Energy Physics, St. Andrews, Scotland, UK,
CERN Yellow Book 99-04;

[14] Particle Data Group
Review of particle physics
Phys.Rev. **D66** (2002) 010001

[15] The Atlas Collaboration,
Atlas Detector and Physics Performance
Technical Design Report, Vol1
CERN-LHCC-99-14 (1999);

[16] The Atlas Collaboration,
Atlas Detector and Physics Performance
Technical Design Report, Vol2
CERN-LHCC-99-15 (1999);

[17] M. Elsing et al. on the behalf of the Atlas High Level Trigger Group,
Configuration of the Atlas Trigger System,
ATL-DAQ-2003-038, arXiv:hep-ph/0306046 v1 5 Jun 2003;

[18] The Atlas Collaboration
Atlas High Level Trigger Data Acquisition and Controls
CERN/LHCC/2003-022 Atlas TDR 016, 30 June 2003;

[19] T. Schoerner-Sadenius, S. Tapprogge,
Atlas Trigger Menus for the LHC Start-up Phase,

ATL-DAQ-2003-004, 11 Jul 2003;

[20] T. Sjostrand et al.,
Pythia 6.221 LU TP 01-21, hep-ph/0108264
Pythia 6.221 Physics and Manual;

[21] Used by courtesy of Yvonne Peters

[22] E. Richter-Was et al.,
ATLFAST 2.0 a fast simulation package for ATLAS,
ATL-PHYS-98-131, 13 Nov 1998;

[23] J. E. Garcia-Navarro et al.,
The b-tagging performance of the complete ATLAS DC1 layout using WH events,
ATL-com-indet-2003-017, 29 Jul 2003;

[24] A. Kootz,
B-Identifikation in Level 2 Trigger des ATLAS Experiments
Doctoral Thesis
WUB-DIS 2005-08;

[25] G. Borisov,
Combined b-tagging,
DELPHI 97-94 PHYS 716, 23 Jul 1997;

[26] J. Hertz, A. Krogh and R. G. Palmer
Introduction to the Theory of Neural Computation, Addison Wesley,
Redword City, CA, 1991;

[27] C. Peterson and T. Rognvaldsson,
An introduction to Artificial Neural Networks,
1991 CERN school of computing;

[28] `http://www-cdf.fnal.gov/physics/statistics/recommendations/selection.html`
`http://www.doc.ic.ac.uk/~nd/surprise_96/journal/vol4/cs11/report.html`

[29] CDF Collab., F. Abe et al.,
Phys. Rev. Lett. **73** (1994) 225, hep-ex/9405005,
Phys.Rev. **D50** (1994) 2966;

[30] CDF Collab., F. Abe et al.,
Phys. Rev. Lett. **74** (1995) 2626, hep-ex/9503002;

[31] D0 Collab., S. Abachi et al.,
Phys. Rev. Lett. **74** (1995) 2632, hep-ex/9503003;

[32] CDF Collab., F. Abe et al.,
Phys. Rev. **D51** (1995) 4623, hep-ex/9412009;
Phys. Rev. Lett. **75** (1995) 3997, hep-ex/9506006,
Phys. Rev. **D52** (1995) 2605;

[33] B. Resende, *Top Properties within the SM*,
ATL-COM-PHYS-2006-020,CERN, 27 Feb 2006;

[34] A. Lucotte,
Top physics prospects in Atlas, ATL-PHYS-CONF-2006-002;

[35] N. Kidonakis and R. Vogt, Phys. Rev. **D68** (2003) 114014,
Eur. Phys. J. **C33** (2004) 446;

[36] R. K. Ellis, W. J. Stirling und B. R. Webber,
QCD and Collider Physics,
Cambridge University Press, Cambridge 1996;

[37] M. Beneke et al.,
Top Quark Physics
CERN-2000-004 Yellow Report, hep-ph/0003033 419-529;

[38] Frank Fiedler
Top quark production and properties at the Tevatron,
arXiv:hep-ex/0506005 v12Jun2005;

[39] I. Borjanovic et al.
Investigation of top mass measurements with the Atlas detector at LHC
hep-ex/0403021;

[40] The LEP Collaborations and the LEP Electroweak Working group
hep-ex/0511027 (2005);

[41] *Combination of CDF and D0 Results on the Mass of the Top Quark*,
The Tevatron Electroweak Working Group for the CDF and D0 Collaborations,
hep-ex/0603039, 20 March 2006;

[42] T. Stelzer and S. Willenbrock
Phys. Lett. **B374** (1995) 169-172;

[43] F. Kalen Martens on the behalf of the Atlas Collaboration
Top Physics Capabilities at the LHC,
ATL-PHYS-2004-024;

[44] E. Richter-Was et al.,
Minimal Supersymmetric Standard Model Higgs rates and backgrounds in ATLAS,
CERN-TH/96-111, 22.4.1996;

[45] H. Georgi, S. Glashow, M. Machacek and N. Nanopoulus,
Phys. Rev. Lett. 40 (1978) 692;

[46] K. Gaemers and F. Hoogeveen,
Phys. Rev. Lett. **B 146** (1984) 347;

[47] D. Dicus, A. Stange, S. Willenbrock,
Higgs decays to top quarks at hadron colliders,
Phys. Rev. Lett. B333 (1994) 126-131;

[48] L. Resnick, Phys. Rev. **D2**, 1975 (1970);
J.Pumplin, Phys. Rev. **D2**, 1859 (1970);
T. Bauer, Phys. Rev. Lett. **25**, 485 (1970);
J.-L. Basdevant and E. Berger, Phys. Rev **D16**,
657 (1977); **D19**, 239 (1979); **D19**, 246 (1979);
D. Morgan and M. Pennington, Z. Phys C37, 431 (1988);

[49] J.Gunion, H.Haber, S.Dawson, *The Higgs hunters guide*,
Addison-Wesley, New York, 1990;

[50] F.Berends, J.Tausk and W.Giele,
Phys. Rev. **D47**, 2746 (1993);

[51] B. List and J. List,
MarlinKinfit: An Object-Oriented Kinematic Fitting Package,
LC-TOOL-2009-001;

[52] T. Sjöstrand et al.,
High Energy Physics Event Generation with Pythia 6.1,
Comput. Phys. Comm. **153** (2001) 238,
hep-ph/0010017

[53] J. D. Bjorken and S .J. Brodsky, Phys.Rev. **D1** (1970) 1416;

[54] R. J. Barlow, *Statistics, A Guide to the Use of Statistical Methods in the Physical Sciences*,
John Wiley and Sons, Baffins Lane, Chichester,
West Sussex PO19, 1UD, England 1989;

[55] Peter Mättig, Private conversation;

[56] L. Lyons, Private communications;

List of Figures

List of Tables